Multiscale characterization of cardiac remodeling induced by intrauterine growth restriction, at organ, cellular and subcellular level

Anna González Tendero

PhD THESIS

Programa Doctorat Biomedicina

Metabolisme, senyalització metabòlica i patologies associades

Facultat de Medicina - Universitat de Barcelona

Multiscale characterization of cardiac remodeling induced by intrauterine growth restriction, at organ, cellular and subcellular level

Submitted by

Anna González Tendero

To obtain the degree of “Doctor in Biomedicine”

and the International Doctor Mention

Director:
Professor Fátima Crispi Brillas

Director:
Professor Bart Bijnens

Tutor:
Professor Eduard Gratacós Solsona

Universitat de Barcelona
Facultat de Medicina
Programa de Doctorat de Biomedicina
Metabolisme, senyalització metabòlica i patologies associades

A Thesis submitted by Anna González Tendero for the PhD degree (Doctor in Biomedicine, University of Barcelona) including the mention of “International Doctor” under the direction of Fatima Crispi Brillas; Consultant and Senior Researcher; Bart Bijnens, ICREA Research Professor and Eduard Gratacós Solsona; Professor of Obstetrics and Gynecology at Universitat de Barcelona.

Anna González Tendero

Barcelona, May 2014.

Fátima Crispi Brillas, PhD
Consultant and Senior Researcher
Fetal i+D Fetal Medicine Research Center, IDIBAPS
BCNatal | Barcelona Center for Maternal Fetal and Neonatal Medicine
Hospital Clínic and Hospital Sant Joan de Déu, Universitat de Barcelona

Professor Bart Bijnens
ICREA Research Professor in the Department of Information and Communication Technologies
University Pompeu Fabra, Barcelona, Spain

Professor Eduard Gratacós Solsona
Professor in Obstetrics and Gynecology
Head of the Fetal i+D Fetal Medicine Research Center, IDIBAPS
BCNatal | Barcelona Center for Maternal Fetal and Neonatal Medicine
Hospital Clínic and Hospital Sant Joan de Déu, Universitat de Barcelona

We declare that **Anna González Tendero** has performed under our supervision the studies presented in the Thesis **"Multiscale characterization of cardiac remodeling induced by intrauterine growth restriction, at organ, cellular and subcellular level"**. This Thesis has been structured following the normative for PhD Thesis as a compendium of publications, to obtain the degree of **International Doctor in Biomedicine** and the mentioned studies are ready to be presented to a Tribunal.

Codirector	Codirector	Tutor
Fàtima Crispi Brillas	**Bart Bijnens**	**Eduard Gratacós Solsona**

Barcelona, May 2014.

PRESENTATION

The present Thesis has been structured following the normative for PhD Thesis, as a compendium of publications, to obtain the degree of International Doctor in Biomedicine. It was approved by the "*Comissió del programa de Doctorat en Biomedicina"* on the 20th June 2011. Projects included in this Thesis belong to the same research line, leading to four articles published or submitted for publication in international journals:

Study 1. Gonzalez-Tendero A, Zhang C, Cárdenes R, Balicevic V, Loncaric S, Butakoff C, Paun B, Bonnin A, Gratacós E, Crispi F, Bijnens B. Whole heart detailed and quantitative anatomy, myofiber structure and vasculature from X-ray phase-contrast synchrotron radiation-based micro-CT.
Status: In preparation

Study 2. Gonzalez-Tendero A, Torre I, Garcia-Canadilla P, Crispi F, García-García F, Dopazo J, Bijnens B, Gratacós E. Intrauterine growth restriction is associated with cardiac ultrastructural and gene expression changes related to the energetic metabolism in a rabbit model. Am J Physiol Heart Circ Physiol. 2013; 305: H1752–H1760.
Status: published
Journal Impact Factor: 3.629
Quartile: 1st , area Physiology.

Study 3. Iruretagoyena JI, Gonzalez-Tendero A, Garcia-Canadilla P, Amat-Roldan I, Torre I, Nadal A, Crispi F, Gratacos E. Cardiac dysfunction is associated with altered sarcomere ultrastructure in intrauterine growth restriction. Am J Obstet Gynecol. 2014. doi: 10.1016/j.ajog.2014.01.023.
Status: published
Journal Impact Factor: 3.877
Quartile: 1st , area Obstetrics and Gynecology.

Study 4. Torre I, González-Tendero A, García-Cañadilla P, Crispi F, García-García F, Bijnens B, Iruretagoyena I, Dopazo J, Amat-Roldán I, Gratacós E. Permanent cardiac sarcomere changes in a rabbit model of intrauterine growth restriction.

Status: submitted to PlosOne

Journal Impact Factor: 3.73

Quartile: 1st *,* area Multidisciplinary Sciences.

TABLE OF CONTENTS

1. INTRODUCTION

1. INTRODUCTION

1.1. Developmental origins of cardiovascular disease

Cardiovascular diseases are the leading cause of mortality in developed countries, with an estimated 23% of all disease burdens and over 4 million deaths each year in Europe (European Heart Network). It has been historically thought that cardiovascular diseases are determined by genetic factors and lifestyle, amount of physical activity and quality of nutrition in early adulthood. In most cases, cardiovascular diseases undergo a long subclinical phase that can last decades before the first clinical symptoms appear. Barker's studies were the first to show a direct correlation between low birth weight and cardiovascular diseases in adulthood, including hypertension, stroke, myocardial infarction or cardiovascular dysfunction [1]. They proposed the hypothesis of "developmental origins of disease", which stipulated that low birth weight was associated with the presence of cardiovascular disease in the adult [1], and suggested the idea that *in utero* programming of disease could occur. This concept is now known as "fetal programming" and is defined when an insult *in utero* leads to functional changes in key organs that remain in postnatal life and lead to a greater risk of disease in adulthood [2,3,4,5].

1.2. Intrauterine Growth Restriction

Intrauterine growth restriction (IUGR) affects 7-10% of all pregnancies and is a major cause of perinatal mortality and long-term morbidity [6]. Low birth weight, most likely due to IUGR is strongly associated with increased risk of cardiovascular mortality in adulthood [7]. This association is thought to be mediated through fetal cardiovascular programming. IUGR is diagnosed when a fetus does not reach its growth potential. The concept of "normal" birth weight or "adequate" fetal growth has changed throughout the years [8,9]. IUGR is characterized by the birth weight and body mass lower than normal with respect to the number of gestational weeks [10]. It is generally accepted that IUGR fetuses are those that have an estimated fetal weight below the 3rd centile [9], or below the 5th centile of abdominal circumference, who have no other abnormalities (chromosomal, structural, infectious or other diseases) [11,12,13].

Placental insufficiency is the main cause of IUGR, and it also constitutes the major cause of perinatal mortality and severe morbidity [6]. IUGR can be classified into early- and late-onset IUGR based on gestational age at diagnosis and umblical artery Doppler patterns [14,15]. Early-onset IUGR results from severe placental insufficiency before 34 weeks of gestation, affects less than 1% of deliveries and constitutes a main cause of perinatal mortality and morbidity [6]. It is characterized by an increase in impedance to blood flow at the umbilical artery and subsequent fetal vasodilatation mechanism to maintain cerebral oxygen supply [16]. The severity of placental dysfunction is determined by the grade and the progression rate of Doppler abnormalities [17]. Late-onset IUGR occurs after 34 weeks of gestation and differs by clinical manifestations, patterns of deterioration and severity of placental dysfunction which is normally milder and with normal umbilical artery blood flow [18,19].

1.3. Fetal cardiac function and remodeling

The heart achieves its function by contracting its muscular walls around a closed chamber to generate sufficient pressure to eject blood. Its main purpose is to generate the required cardiac output to assure adequate perfusion to organs and to be able to adapt to changing demands, like exercise, and changing working conditions, like cardiovascular diseases [20,21,22]. Systolic and diastolic processes must occur in a specific time course and synchronized manner to maintain cardiac function. Cardiac cycle is integrated by five phases, which define main features of cardiac blood flow movement and myocardial motion: isovolumetric relaxation phase, early diastole, atrial contraction period, isovolumetric contraction phase and ejection period [21].

Cardiac function and shape are mainly determined by myocardial contractility, fiber orientation, tissue elasticity, heart geometry, loading conditions, electrical activation and myocardial perfusion. In the fetal heart, however, other factors play a relevant role: myocardial maturation and fetal blood circulation [23]. During *in utero* development myocardial maturational changes lead to changes in elasticity and contractility throughout the pregnancy [24]. While structural arrangements are established during the embryonic period, the fetal heart continues to grow by cell division and cell enlargement. The fetal circulation has some specific properties compared to postnatal life. A small proportion of the right output is directed to the lungs, while the systemic circulation is fed from the left and

right ventricles in parallel [23]. There are three shunts - ductus venosus, ductus arteriosus and foramen ovale - whose hemodynamic properties are key determinants for the development of the fetal heart and circulation during the second and third trimester of pregnancy [23]. Therefore, in the fetal heart, changes in ventricular loading are important factors for cardiac maturation and cardiac function. Preload refers to the (volume) load prior to contraction and is mainly determined by venous return. In fetal heart, for instance, an increase in pulsatility of the ductus venosus will increase the venous return, causing a volume overload. It will lead to heart dilatation to make the heart able to cope with the increased blood volume while increasing its efficiency [25]. Afterload is defined as the tension against which the ventricle must contract, and is detemined by pressures at the aorta (left ventricle) and pulmonary artery (right ventricle). An increase in this tension, for instance due to abnormally higher vascular or placental resistance, will lead to a pressure overload condition, which will cause myocardial hypertrophy in order to increase contractile mass to overcome the higher afterload [25].

Fetal cardiac function is usually assessed by measuring blood flow through conventional Doppler, cardiac morphometry in 2D or M-mode, tissue Doppler and 2D speckle tracking imaging [21]. Table 1 shows the most common parameters used to evaluate fetal cardiac function as well as their definition.

Hence, fetal cardiac structure and function can be affected by a variety of abnormal fetal conditions like pressure or volume overload, hypoxia, hyperglicemia, heart compression or direct myocardial damage. When the heart receives an insult, during its initial stages, the heart usually manages to adapt and there is a long subclinical phase that can last decades before the first clinical symptoms appear. During this period of cardiac adaptation, changes in cardiac function and in the heart's shape and size can be measured. These changes are the heart's attempt to adapt to the insult; this process is known as cardiac remodelling [21].

Table 1. Common parameters used to evaluate fetal cardiac function

Parameter	Definition
SYSTOLIC FUNCTION	
Ejection fraction	Fraction of blood ejected from the ventricle with each heart beat
Cardiac output	Volume of blood pumped from the ventricle per minute
Annular displacement	Distance of the movement of the atrioventricular valve annulus
Systolic annular peak velocity	Speed of movement of the atrioventricular valve annulus in systole (S')
DIASTOLIC FUNCTION	
Precordial vein blood flow patterns (DV and others)	Pattern o blood in precordial veins during atrial contraction that indirectly reflects cardiac compliance
E/A ratio	Ratio between early (E) and late (A) ventricular filling velocity
Diastolic annular peak velocities	Speed of movement of the atrioventricular valve annulus in early and late diastole
Isovolumetric relaxation time (IRT)	Time between closure of the aortic valve and opening of the mitral valve

Modified from [21].

1.4. Cardiac dysfunction and remodeling associated to IUGR

The heart is a central organ in the fetal adaptive mechanism to placental insufficiency and cardiac dysfunction is recognized as being among the central pathophysiologic feature of both early- and late-onset IUGR [26]. The prediction of mortality, morbidity and the subclinical cardiac dysfunction associated with IUGR is critical for the management of these fetuses [27]. Cardiac dysfunction in early-onset IUGR fetuses is mainly characterized by signs of decreased longitudinal motion and impaired relaxation (diastolic dysfunction) from the early stages of deterioration, showing increased ductus venosus pulsatility index, higher E/A ratio, increased isovolumic relaxation time, reduced annular peak velocities, and increased levels of atrial natriuretic peptide and B-type natriuretic peptide on cord blood [27]. Late-onset IUGR fetuses might also show features of cardiac dysfunction [28,29] with increased values of myocardial performance index, decreased annular peak velocities and increased cord blood levels of troponins.

Fetal abnormal conditions in placental insufficiency that are believed to lead to cardiac dysfunction in IUGR are: hypoxia, volume and pressure overload [21,30]. All of them are considered insults for the heart. A chronic restriction of oxygen and nutrients [31] triggers the initiation of a variety of adaptive structural [26,27,32,33] and metabolic responses [34]. Under the state of chronic hypoxia and undernutrition, the objective of the IUGR fetus is to preferentially divert its cardiac output to its vital organs (brain, heart, adrenal glands and liver). This effect is known as “brain sparing effect” and mainly causes an increase in the

pulsatility of precordial veins (ductus venosus), which increases preload [35]. This redistribution together with an increased placental resistance, results in a combined volume and pressure overload condition of the fetal heart [30]. As a consequence, IUGR fetuses and newborns show signs of cardiac remodeling and altered function [27,36,37].

The effect of hypoxia and nutrient restriction in cardiac development and function has been previously studied, demonstrating the actual association of IUGR to a cardiac remodeling. Maternal hypoxia has been related to changes in cardiac structure and function [38,39,5], increased cardiac collagen content [40], changes in cardiomyocyte proliferation and apoptosis [41,42] and to long-term effects increasing cardiac susceptibility to ischemia-reperfusion injury by causing changes on myocardial energetic metabolism [43,44].

The cardiac hemodynamic changes due to IUGR also induce adaptive changes to the coronary circulation. The coronary vascular tree in the immature heart is very plastic and has the ability to remodel to meet the oxygen demands of the myocardium, however, this remodeling may predispose for adult coronary disease [45]. Doppler evaluation of human fetuses has shown changes in coronary flow that seem to be one of the last stages of cardiac decompensation and dysfunction before death [35,46]. However, the remodeling of the coronary vascular tree may occur before its visualization is possible on colour Doppler evaluation [35]. It has been observed that coronary vascular tree responds to conditions of chronic hypoxemia by a substantial increase in the cross-sectional area of the vessels [45] or by increasing coronary vessel growth and myocardial vascularization [47].

Although effects of hypoxia on fetal heart adaptation have been characterized, it is not clear how the fetal heart manages to adapt to the *in utero* pressure/volume overload condition. It is believed that cardiac remodeling in IUGR may result from a combination of strategies to adapt to the three different insults, but the underlying events of this remodeling in IUGR at the organ, cellular and subcellular scale still remain poorly understood.

The postnatal persistence of cardiac remodeling has been demonstrated in a cohort of 5-year old children that suffered from IUGR. IUGR children show a more globular cardiac morphology, subclinical cardiac dysfunction and vascular remodeling [36]. Additionally, several studies using animal models give support to the postnatal persistence of changes induced by prenatal hypoxia [5,38]. This notion is extremely relevant to reinforce the association of IUGR with increased risk of cardiovascular disease in adulthood. Overall, these studies suggest that IUGR induces primary cardiac changes.

Consequently, the early identification of signs of cardiac remodeling due to IUGR as well as an intensive cardiac function assessment could help to identify IUGR cases at higher cardiovascular risk later in life and therefore could allow the implementation of timely preventive interventions [17].

1.5. Detailed cardiac anatomy

The myocardium is made of millions of cardiomyocytes that are aggregated together as a three-dimensional mesh within a supporting matrix of fibrous tissue [48,49]. Cardiomyocytes are arranged in a very specific way within ventricular walls, forming the fibers. The organization of the fibers within the walls forms the cardiac geometry with a specific curvature and thickness. This complex cell organisation is what allows the heart to efficiently pump a large volume-fraction, because cardiomyocytes can only maximally shorten by 10-15%, so their ability to shorten is limited [50].

Myocytes are aggregated and aligned in a predominant direction, depending on their position with the myocardial wall [49]. At the epicardium as well as the endocardium, they are aligned tangential with a predominant longitudinal (base-apex) direction, while in the mid-myocardium they are predominantly circumferential [49] The change in angulation relative to the ventricular equator (helical angle) is gradual and the helical angle in the epicardial layers is opposite to the helical angle in the subendocardial layers [49,51], and tends to approach 90° at the endocardium and -90° at the epicardium [52].

The cardiac contraction, in terms of motion, results from a complex three-directional movement that involves longitudinal and circumferential contraction, radial thickening and rotation of the basal versus the apical planes. These cardiac movements are determined by the complex three-dimensional organization of the fibers within the cardiac walls. Longitudinal contraction is determined by predominantly longitudinally oriented fibers in the endo- and epi-cardium, of which the endocardial ones are the most sensitive to hypoxia because of being localized most distal in the coronary tree originating from the epicardium. Circumferential contraction is predominantly determined by fibers located in the mid myocardium. The rotation and twisting depends on the obliqueness of the fibers in the myocardial wall [20].

Several studies provide evidence of the strong relationship between regional cardiac architecture, myofiber alignment and cardiac function. The three dimensional cardiac and cardiomyocyte architecture and organization are established early in prenatal life, but exhibit high plasticity afterwards [53]. However little is known about the changes of cardiac architecture over cardiac development. The normal 3D fiber architecture in embryonic and fetal myocardium has been studied using polarized light microscopy and laser scanning confocal microscopy [54,55,56]. Tobita et al. showed that during normal development, in the left ventricle myocardium, fiber angle distribution changed from a uniform transmural circumferential orientation to a gradual transmural shift in orientation from circumferential (endocardium) to longitudinal (epicardium) [56]. Fiber orientation is sensitive to changes in mechanical load. When there is a reduction in the mechanical load, the left ventricle undergoes a hypoplasic adaptation and transmural variation of fiber angle results to be immature. On the contrary, an increased mechanical load induces ventricular hyperplasia and an acceleration of fiber maturation [56].

Linking information on individual cells to their spatial organization and functioning of the whole organ is essential for understanding diseases and remodeling. Several techniques have been used to study fiber organization, such as diffusion tensor MRI or echocardiography, but without enough resolution to detect the orientation of individual cardiomyocytes [57,58]. Histology and optical microscopy provide sufficient detail, but do not allow to image whole hearts, and slicing/processing is required, which could be a source of artefacts on the actual cardiac structure [54,55].

In this Thesis we used an integrated, high resolution, image acquisition and quantification approach to study a whole heart at myofiber resolution, providing structural information at microscopic level without need of slice processing (Fig 1). The imaging is based on X-ray phase-contrast synchrotron radiation-based micro-CT [59]. Phase-contrast imaging with synchrotron radiation has emerged as a novel X-ray-based imaging approach providing enhanced image contrast in some biological tissues and additionally suggesting the potential to improve the diagnostic work-up [60].

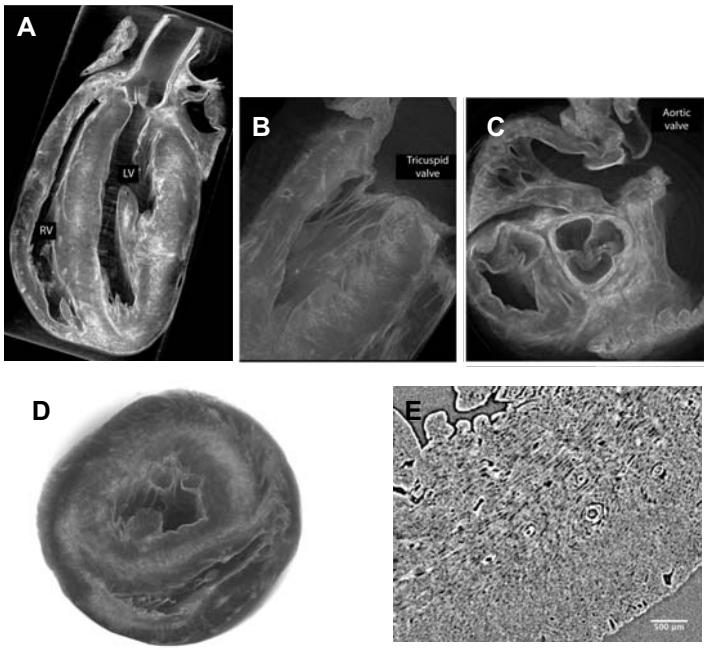

Figure 1. X-ray phase-contrast synchrotron radiation-based micro-CT imaging of a rat heart. A, When performing volume rendering of the raw images, cardiac architecture can be observed in great detail. **B**, the architecture of the tricuspid valve as well as **C,** the aortic valve are clearly visualised. **D**, volume rendering of a transverse section where ventricular walls architecture as well as fiber orientation can be recognized. **E**, shows a detailed view of part of the heart tissue, where fiber orientation can be recognised in the ventricular walls.

1.6. Cardiomyocyte intracellular organization

Differentiation and maturation of cardiomyocytes lead to a complex specialization and a high degree of intracellular structural organization. This allows a high degree of organization of specialized cellular functions within structural and functional compartment [61]. Perinatal development of cardiomyocytes is associated with a profound reorganization of the cell architecture whose main changes are an increase of the mitochondrial and myofibrillar mass, sarcoplasmic reticulum (SR) maturation, compaction of the cellular components and as a consequence there is a decrease of the amount of cytoplasm [62,63]. It is during this period that a complex compartmentation of the structures involved in calcium handling system and energy transference starts [64,65]. SR and T-tubules organization is built up for a maximum excitation-contraction coupling efficiency and energetic compartmentation is as well established for an optimal energy production and transference [64,65,66]. Therefore mitochondria, myofibrils and SR acquire their fixed position during cardiomyocyte maturation. It is well studied that in cardiomyocytes there is a complex relationship between cellular architecture and cell function, and there is a need for

a very early optimization of the cardiomyocyte cytoarchitecture for a proper optimization of cardiac function [65]. Cytoarchitectural disarrangements such as misalignment of mitochondria and myofibrils, heterogeneity of mitochondrial shape and size and mitochondrial degradation, have been observed in several models of heart failure [67,68].

The heart has high-energy requirements in the form of ATP, and it has to permanently adjust energy production to energy consumption [69,70]. For this, the heart mainly depends on oxidative metabolism for adequate energy production and on efficient energy transfer systems. More than 90% of heart's muscle energy is produced from mitochondrial respiration. Mitochondria occupy more than 30% of the cardiomyocyte volume and are densely packed, organized under the sarcolemma and in rows between myofilaments in the adult cardiomyocyte [69]. The main cardiac energy consumers are SERCA (sarcoendoplasmic reticulum calcium-ATPase) located in the sarcoplasmic reticulum and the MHC-ATPase (myosin heavy chain ATPase) located in the sarcomere thick filaments. The highly ordered mitochondrial spatial distribution constitutes an optimal organization for energy transference between mitochondria and the main energy consumers and provides a constant diffusion distance between mitochondria and the core of myofilaments [69]. The intracellular energetic units (ICEUs), are structural and functional units, consisting of mitochondria located at the level of the sarcomeres between Z-lines interacting with surrounding myofilaments, sarcoplasmic reticulum, cytoskeleton and cytoplasmic enzymes, that promote an endogenous cycling of adenine nucleotides between mitochondria and ATPases [71,72,73]. Alterations in ICEUs arrangement together with an impaired local energetic regulation of the main cardiac ATPases have been described in cardiac pathophysiological processes [67]. In addition to the highly specialized intracellular organization, cardiomyocyte energetic homeostasis is regulated by a complex interaction of molecular pathways, mainly involving energy production through oxidative phosphorylation in the mitochondria [74]. It has been widely described that disruption of mitochondrial oxidative phosphorylation plays a critical role in the development of heart failure [75,76,69]. The oxidative phosphorylation takes place in the mitochondrial electron transport chain. It is composed of five complexes; in the complex I the enzyme NADH dehydrogenase catalyzes the reaction [77]. Deficiencies in complex I function have been observed in dilated cardiomyopathy and in failing myocardium [78].

1.7. Ultrastructure of the sarcomere

The sarcomere is the elementary contractile unit in cardiac muscle. It is mainly composed of myosin (thick) filaments and actin (thin) filaments. Contraction is produced thanks to myosin sliding over actin filaments, while other proteins form a scaffold that ensures the efficiency of their interaction and optimal transmission of the generated force [79]. The arrangement of the filaments into parallel bundles gives a characteristic striated pattern to sarcomeres under electron microscope, in which different transverse structures can be identified: the Z-discs that define sarcomere borders and anchor the antiparallel thin filaments of adjacent sarcomeres; the I-band, which is occupied only by thin filaments; the A-band, which contains thick filament bundles; the M-band, which is the lighter zone in the center of the A-band and corresponds to the crossbridge-free portion of the thick filament. The giant protein titin spans from Z-disc to M-band, it acts as a scaffold protein by integrating thick and thin filaments into the sarcomeric unit and it is believed to define the resting sarcomere length in addition to be the main stress sensor [79].
The expression of sarcomeric proteins is well documented to respond to physiological activity or disease, making the sarcomere a prime candidate for a visible indicator of myofiber integrity [80,81,82]. The study of sarcomere morphometry provides information about the sarcomere's structure and function and thus about cardiac contractility [83]. For this, end-diastolic sarcomere length has been widely used as a feature of sarcomere morphometry [84,85]. Sarcomere length is strongly related to sarcomere function and contraction force, and has been described to be consistently altered in a substantial number of conditions associated with cardiac failure [86,87,88]. Changes in sarcomere structure and its key proteins have been observed in models of cardiac dysfunction and failure [89,90,91]. In a previous experimental study, it was demonstrated that chronic pre-natal hypoxia induced permanent post-natal changes in the isoforms and content of sarcomeric proteins, including titin and myosin [5].

In this Thesis sarcomere was studied by using multiphoton and second harmonic generation (SHG) microscopy, which is a technique based in a nonlinear optical effect known as second harmonic generation. It is widely used in biomedical research as an imaging technique allowing measurement of morphological features at subcellular level, including sarcomere length and pattern [92,93] by identifying the myosin from the sarcomere [94,95] without the need of staining, and thus eliminating artefacts associated to staining processes. The SHG signal along a muscle fiber shows a biperiodical pattern as

shown in Figure 5 (methods). The two periods are associated with characteristic sarcomeric lengths that provide information of the ultrastructure of the cardiac tissue [84,96,97]. Particularly, the shortest period corresponds to the A-band distance and the longest period to sarcomere length (distance between Z discs). Our group recently developed an automated and accurate methodology, based on the autocorrelation quantification, which allows to sistematically measure sarcomere morphology from SHG images of unstained cardiac tissue. With this method several parameters can be quantified: sarcomere length (SL), A-band length (ABL) and thick-thin filament interaction length (TTIL) [98].

1.8. Relevance and justification of the research study

Most factors leading to cardiovascular disease are already present in childhood and the importance of early identification of cardiovascular risk factors is now well recognized. Primary cardiac remodeling and programming might be one of the causes of increased cardiovascular disease and mortality in adults born with IUGR. Although clinical features of fetal IUGR and cardiac dysfunction have been studied [27,26], the underlying pathophysiological mechanisms leading to this dysfunction, at cellular and subcellular level are still not well understood. Gaining understanding on the responsible mechanisms for cardiac remodeling and programming in IUGR might help to open new opportunities for monitoring, identifying therapeutic targets or designing new interventional strategies in newborns and children affected by this condition. Since IUGR affects 7-10% of all newborns, designing new strategies to detect and assess the risk of cardiovascular programming might benefit thousands of children yearly.

This thesis consists on a comprenhensive study to evaluate cardiac remodeling due to IUGR at all levels, from the whole cardiac architecture, through cardiomyocyte architecture, to the ultrastructure of the sarcomere. The characterization of this remodeling might help to better understand the pathophysiological mechanisms underlying cardiac dysfunction in IUGR. To achieve our objectives, novel imaging techniques have been used. The novel implemented imaging techniques could also have a potential application in understanding other cardiac diseases and open up new possibilities for a systems approach towards cardiac function. In the **study 1**, the detailed anatomy of the whole heart has been studied using X-ray phase-contrast synchrotron radiation-based micro-CT. The **study 2** focuses on the study of the cardiomyocyte intracellular organization using transmission electron

microscopy. Finally, in **studies 3** and **4**, the ultrastructure of the sarcomere, the basic contractile unit, was evaluated using multiphoton microscopy and second harmonic generation imaging.

The main goal of this Thesis is to provide a comprehensive understanding of the cardiac structural changes induced by IUGR. In order to achieve this objective, four specific projects with specific hypothesis and objectives were designed. This introduction aimed to globally explain and justify each specific project.

2. HYPOTHESIS

2. HYPOTHESIS

2.1. Main hypothesis

Intrauterine growth restriction induces cardiac remodeling and dysfunction at organ, cellular and organelle level.

2.2. Specific hypothesis

- Cardiac anatomy and fiber orientation change as an adaptation to IUGR.
- IUGR cardiomyocytes present abnormal intracellular arrangement of the organelles.
- The contractile machinery presents structural alterations in IUGR hearts.
- The structural alterations in IUGR hearts are present *in utero* and persist postnatally.
- Cardiac remodelling in IUGR is associated with cardiovascular dysfunction.

3. OBJECTIVES

3. OBJECTIVES

3.1 Main objective

To characterize cardiac remodeling and function in IUGR, at organ, cellular and cell-organelle level.

3.2 Specific objectives

- To analyze detailed cardiac anatomy, fiber orientation and coronary vasculature in IUGR fetal hearts using X-ray synchrotron radiation.

- To evaluate the intracellular organization of the cardiomyocytes' organelles using transmission electron microscopy in IUGR fetuses.

- To evaluate the morphometry and ultrastructure of the contractile machinery, the sarcomere, of IUGR fetal hearts using second harmonic generation microscopy.

- To determine the postnatal persistence of the fetal morphometric changes of the sarcomere in IUGR.

- To assess the association of cardiac remodelling with functional parameters in IUGR.

4. METHODS

4. METHODS

4.1. Study populations

4.1.1. Human IUGR population (study 3)

The human study population included 9 severe early-onset IUGR and 9 control fetuses from 19 to 33 weeks of gestational age, who died in the perinatal period due to perinatal complications or medical termination of pregnancy. Cases were singleton pregnancies with IUGR that had been included in a large prospective cohort evaluating cardiac dysfunction in IUGR [36]. IUGR was defined as an estimated fetal weight below the 10th centile according to local reference curves [99] together with umbilical artery (UA) pulsatility index (PI) above 2 standard deviations [100]. Controls were selected among women undergoing termination of pregnancy due to severe maternal disease or non-cardiac malformations. Intracardiac injection of potassium chloride was electively performed to induce cardiac arrest before induction of labor according to local standard protocols in those cases undergoing termination of pregnancy after 22 weeks of pregnancy.

The study protocol was approved by the Ethics Committee at the participating institution, and all patients provided written informed consent. Exclusion criteria were chromosomal anomalies or evidence of fetal infection. In all pregnancies, gestational age was calculated based on the crown-rump length at first trimester ultrasound.

All cases underwent ultrasonographic examination of fetal wellbeing and hemodynamics within 48 hours of delivery or fetal death, including complete morphological examination, fetal weight, UA, middle cerebral artery (MCA) and cerebro-placental ratio (CPR). All Doppler estimations were done in the absence of fetal body movements and, if required, with maternal voluntary suspended respiration. The mechanical and thermal indices were maintained below 1. UA pulsatility index was obtained from a free loop of the umbilical cord. MCA PI was measured in a transverse view of the fetal skull at the level of its origin from the circle of Willis. Cerebro-placental ratio was calculated as MCA PI / UA PI [99]. All individual Doppler data were normalized by converting the measurements into z-scores (standard deviation from the gestational age mean) [100].

4.1.2. Experimental model of IUGR (studies 1, 2 and 4)

In order to reproduce the IUGR condition, an experimental model previously validated was reproduced [101,102]. New Zealand white rabbits were provided by a certified breeder. Dams were housed for 1 week before surgery in separate cages on a reversed 12/12 h light cycle. Animals were fed a diet of standard rabbit chow and water ad libitum. Animal handling and all procedures were performed in accordance to applicable regulations and guidelines and with the approval of the Animal Experimental Ethics Committee of the University of Barcelona.

A selective ligature of uteroplacental vessels was performed in pregnant rabbits at 25 days of gestation [101] (Fig 2). Briefly, tocolysis (progesterone 0.9 mg/kg intramuscularly) and antibiotic prophylaxis (Penicillin G 300.000 UI intravenous) were administered prior surgery. Ketamine 35 mg/kg and xylazine 5 mg/kg were given intramuscularly for anesthesia induction. Inhaled anesthesia was maintained with a mixture of 1-5% isoflurane and 1-1.5 L/min oxygen. After a midline laparatomy, both uterine horns were exteriorized. The number of gestational sacs from each horn were counted and numbered. Pregnant rabbits have between 4 and 7 gestational sacs per horn. At random, one horn was assigned as the IUGR horn and the other horn was considered as the normal control growth. In all gestational sacs from the horn assigned as IUGR, a selective ligature of the 40-50% of the uteroplacental vessels was performed. No additional procedure was performed in the horn assigned as control. After the procedure, the abdomen was closed and animals received intramuscular meloxicam 0.4 mg/kg/24 h for 48 h, as postoperative analgesia. Five days after surgery, at 30 days of gestation, a caesarean section was performed under the same anesthetic procedure. Before extracting the fetuses, an echocardiographic evaluation was performed as described below (section 4.5.1.). Thereafter all living rabbit fetuses and their placentas were obtained, identified and weighted. Kits were randomly assigned to two age study groups: i) fetal (30 days of gestation) and ii) young adult (70 postnatal days) group. Kits assigned to the young adult group were breast-fed by a wet nurse rabbit until 25 postnatal days. They were then placed on separate cages and were fed a diet of standard rabbit chow and water *ad libitum* until 70 postnatal days.

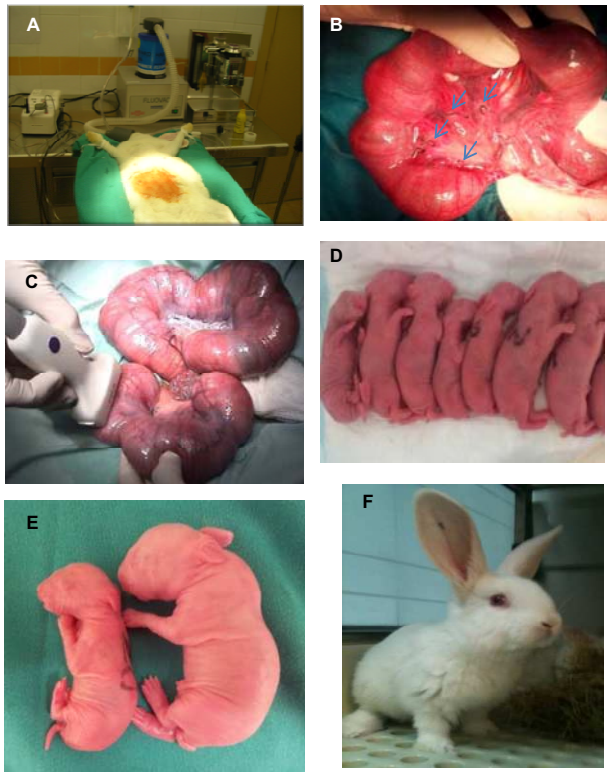

Figure 2. Experimental model of IUGR. A, preparation of the pregnant rabbit, at 25 days of gestation, for the surgery. **B**, ligature of the 40-50% of the uteroplacental vessels of each gestational sac from one uterine horn (blue arrows). **C**, echocardiographic evaluation of the two uterine horns before the cesarean section at 30 days of gestation (picture from [102]). **D**, offspring clearly showing different sizes of the kits, smaller are IUGR while bigger are controls. **E**, detail of a IUGR kit (left) and a control kit (right) at 30 days of gestation. **F**, adult young rabbit at 70 postnatal days.

4.2. Detailed cardiac anatomy of IUGR hearts (study 1)

4.2.1. Sample preparation

In order to evaluate detailed cardiac anatomy, fiber orientation and coronary vasculature, three control and three IUGR fetal rabbit hearts were analyzed. They were obtained after the caesarean section at 30 days of gestation, and were subsequently administered intramuscular ketamine and xylazine for anaesthesia induction. The kits' chest was opened to expose the heart and abdominal aorta. Heparin 500 U was administered through the aorta as well as saturated KCl to arrest hearts in diastole. The abdominal aorta was cannulated and connected to a perfusion pump. A phosphate buffer saline solution was passed through the circulation to rinse blood and subsequently a 10% neutral buffered formalin solution to fix the heart. Hearts were then excised from the animal, immersed in 10 % formalin solution and stored at 4ºC until processing. Before imaging hearts were dehydrated in increasing ethanol concentrations from 10% to 80% in 10% steps. In order to

avoid movement artefacts, hearts were immobilized in 1% agarose solution into a tube that fitted the size of the heart and the size of the sample holder, as shown in Figure 3.

4.2.2. Image acquisition

X-ray phase-contrast synchrotron radiation-based micro-CT was performed at the European Synchrotron Radiation Facility (ESRF, Grenoble), beamline ID19. The X-ray beam energy range was 19Kev and propagation distance between the object and the camera was 1100 mm, obtaining a field of view of 5,68x15,96 mm, and a pixel size of 7.43µm. The heart was maintained inside a tube at room temperature, was placed on top of a holder, and was positioned remotely at the center of the beamline (Fig 3B). The sample was rotated 360 degrees acquiring a total of 2499 projections during the whole rotation (Fig 3C, D). The exposure time for each projection was 0.3 seconds and the total time of each rotational acquisition was 14 minutes. Four to five rotational acquisitions were necessary to fully cover the whole heart along its long axis. These acquisitions were taken sequentially with an overlap of 363 slices (2,697mm) always from base to apex. After each acquisition, a set of 41 reference flat field images (with the sample removed), and 21 dark images (with sample removed and shutter closed) were taken for background removal. Therefore, total acquisition time was approximately 1h or 1,25h/sample in case of 4 or 5 different chunks were necessary respectively.

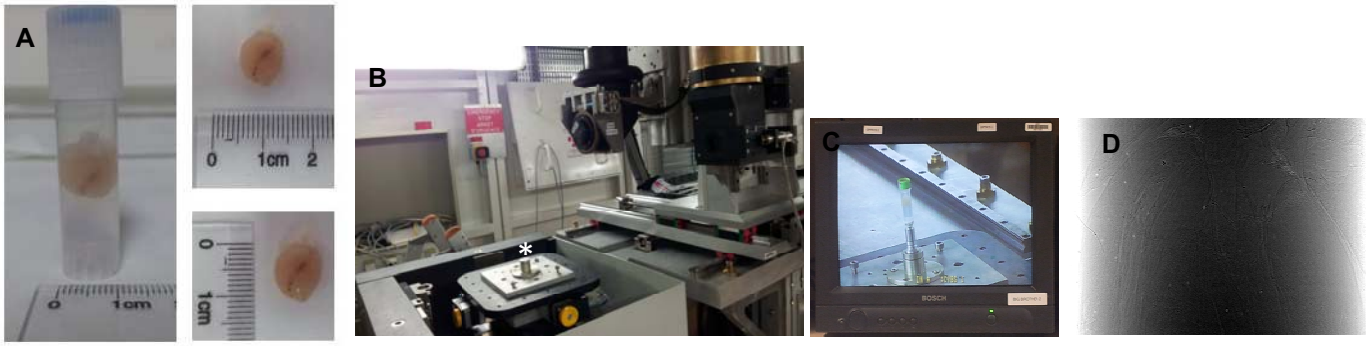

Figure 3. X-ray phase-contrast synchrotron radiation-based micro-CT image acquisition at the ESRF. A, a fixed rabbit fetal heart, dehydrated in ethanol and embedded in agarose; the size of the tube is optimal for the sample holder at the beamline. **B,** sample holder (*) and X-ray beam at the ID19 beamline, ESRF. **C,** detail of the sample placed on the holder, where it rotates over 360º during the imaging. **D**, projection image obtained from a heart, before the 3D reconstruction

4.2.3. Image post-processing and quantification

Each projection series was reconstructed at the ESRF computing facilities using a state of the art filtered backprojection approach as well as the method described in Paganin *et al*. [103]. The reconstructed volumes were then converted to 16 bits tiff image series, merged into a single dataset, and cropped to the desired region of interest. In all cases the whole heart was kept in the resulting 3D dataset. Images were analysed with Fiji (reslicing/rendering) [104], ICY (rendering) [105], Ilastik (vessel segmentation) [106] and in-house developed software for fibre analysis based on Matlab (Mathworks 2007b, version 7.5.0.342; MATLAB, The MathWorks Inc., Natick, Massachusetts, USA).

4.3. *Cardiomyocyte intracellular organization in IUGR hearts (study 2)*

4.3.1. Sample preparation

A transmission electron microscopy study was designed aiming to analyze the intracellular cardiomyoycte organization of control and IUGR fetal rabbit hearts. For this, 3 control and 3 IUGR rabbit fetuses, were obtained at the caesarean section and anesthetized with intramuscular ketamine and xylazine. Hearts were then harvested and immediately arrested in an ice-cold Ca^{2+}-free solution. Random areas of left ventricle were dissected and cut into small pieces. Approximately 10 pieces from each left ventricle were incubated with 2% parafomaldehyde and 2.5% glutaraldehyde in phosphate buffer (PB) during 24 hours at 4ºC. Then, tissue pieces were washed in PB and post-fixed with 1% osmium tetroxide in PB containing 0.8% potassium ferricyanide at 4ºC for 2 hours. Samples were then dehydrated in acetone, infiltrated with Epon resin during 2 days, embedded in the same resin and polymerized at 60ºC during 48 hours.

4.3.2. Image acquisition and quantification

Morphological analysis of intracellular cardiomyocyte organization was performed in 2 randomly selected left ventricle epon resin blocks, from each subject. Semi-thin 500 nm sections were made from the epon resin blocks in order to confirm the longitudinal orientation of cardiac sarcomeres under light microscope. If confirmed, 50 nm ultra-thin sections were obtained from each block from two tissue areas separated 1 μm of distance

(Fig 4A). Ultra-thin sections were cut using a Leica UC6 ultramicrotome (Leica Microsystems, Vienna, Austria) and mounted on Formvar-coated copper grids, stained with 2% uranyl acetate in water and lead citrate. Tissue sections were imaged using a JEM-1010 electron microscope (Jeol, Japan) equipped with a CCD camera Megaview III and the AnalySIS software (Soft Imaging System GmbH, 1998). Images were taken at 20000x magnification when an area containing longitudinal myofilaments surrounded by a mitochondrial network was observed. Micrographs with disrupted mitochondria, disrupted sarcomeres or transversal or oblique orientation of sarcomeres were excluded from the quantification. Electron micrographs were taken and quantified in a blinded fashion. Images were analyzed from three viewpoints:

General cardiomyocyte cyotarchitecture: The volume densities of myofilaments, mitochondria and cytoplasm were estimated in 10 electron micrographs acquired from each heart. For this purpose, a grid in which each line intersection served as a sample point was generated on each image using Image J [107], according to standard stereological methods [108] (Fig 4B). Volume densities of the different structures were calculated by counting the number of points hitting the studied structures divided by the total number of points hitting the section, using a grid size of 0,02 a.u.

Mitochondrial area and number: The area of individual mitochondria was determined from 193 mitochondria in each study group. Individual mitochondria were delineated and their area was measured using the AnalySIS software. The number of mitochondria was counted by using 10 randomly chosen images from each heart as previously described [109].

ICEUs arrangement: The cytoplasmic area and the mean distance between mitochondria and myofilaments within ICEUs were measured by delineating the area of cytoplasm existing between two consecutive z-disks and the immediately adjacent mitochondria using a custom-made GUI (Graphical User Interface) designed in MatLab. The area was automatically calculated and the mean distance between mitochondria and myofilaments within ICEUs was obtained by evaluating the Euclidean distance of the delineated region [110]. A total of 169 ICEUs were analyzed in the control group, whereas 154 ICEUs were analyzed in the IUGR group, obtained from 10 to 15 electron micrographs from each heart. We analyzed all the ICEUs found in the transmission electron microscopy images. However, ICEUs were discarded from the quantification when they were not clear, blurred or if the limits to mitochondria were not sharp enough

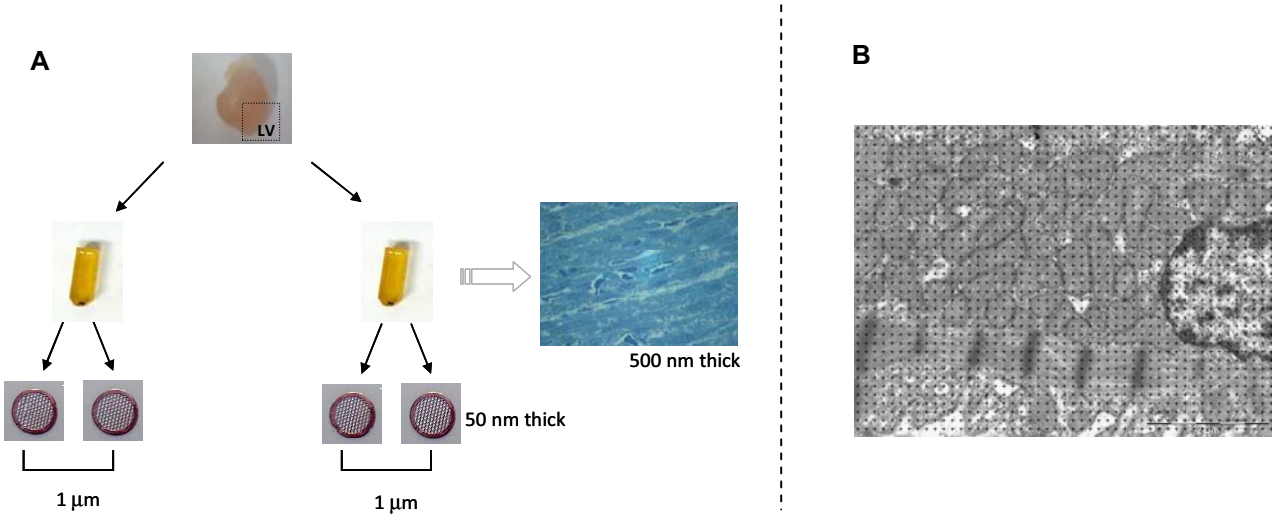

Figure 4. **Sampling procedure for transmission electron microscopy imaging. A**, sampling procedure of fetal rabbit hearts: two different tissue pieces from left ventricle were embedded in epon resin. From each epon resin block, 500 nm thick semithin sections were obtained in order to confirm longitudinal orientation of myofibers. Then two grids containing several 50 nm thick slices were obtained from each block; slices from each grid were separated 1 µm of distance to assure different tissue areas were analyzed. **B**, example of an electron micrograph and the grid generated over it for the stereological quantification (magnification 20000x, scale bar = 2 µm).

4.4. *Morphometry of the sarcomere in IUGR hearts (studies 3 and 4)*

4.4.1. Sample preparation

We aimed to study the ultrastructure of the basic contractile unit (sarcomere) by means of second harmonic generation microscopy, in human post-mortem fetal cardiac samples and in hearts from the experimental model of IUGR. For this characterization, on one hand, 9 controls and 9 IUGR post-mortem human fetal cardiac samples were collected at autopsy (refer to section 4.1.1. for details regarding human population). A transverse section of the upper third of posterior left ventricular wall was obtained and then fixed in 3.7% paraformaldehyde, dehydrated and embedded in paraffin. On the other hand, regarding samples from the experimental model of IUGR, at 30 days of gestation rabbit fetuses were obtained after the caesarean section and randomly assigned to two age study groups: i) fetal (30 days of gestation) and ii) young adult (70 postnatal days) group. Hearts from rabbits were obtained through a thoracotomy after anaesthesia (7 Controls and 7 IUGR for both age groups), arrested in Ca^{2+}-free buffer and fixed in 4% paraformaldehyde in PB for

24 hours at 4ºC. Fixed fetal and young adult hearts were dehydrated and embedded in paraffin. The subsequent procedures were the same for both human and animal samples. Transversal heart 30 µm thick sections were cut in a microtome (Leica RM 2135) and mounted onto silane (Sigma-Aldrich) coated thin slides. Tissue sections were deparaffined with xylene and hydrated with decreasing ethanol concentrations (100º / 96º / 70º), and finally covered with Mowiol 4-88 mounting medium (Sigma-Aldrich).

4.4.2. Image acquisition

Unlabelled cardiac tissue samples were identified to contain mostly cardiomyocytes and no collagen. Detection of SHG signal was performed with a Leica TCS-SP5 laser scanning spectral confocal multiphoton microscope (Leica Microsystems Heidelberg GmbH, Manheim, Germany) equipped with a Near Infrared laser (Mai Tai Broad Band 710-990 nm, 120 fempto second pulse) and a DMI6000 inverted microscope, from the Advanced Optical Microscopy Unit from Scientific and Technological Centres from University of Barcelona. A 25x water immersion objective (numerical aperture 0.95) and an oil immersion condenser (NA 1.40 OilS1) were used. Acquisition features were 400 Hz of scan speed, 810 nm excitation light of a two-photon laser and emission collected through a 405 nm filter with transmitted light photomultiplier tube, 16 bit depth and a resolution of 40 nm/pixel. For each heart section, between 8 and 10 SHG images, randomly chosen from the left ventricular mid-wall of the same individual, were acquired. Each image included an average of 15 cardiac muscle fibers containing 200 sarcomeres approximately. Left ventricular cardiac fibers, which are mostly oriented in a single axis in optical sections of approximately 1.5 microns, were aligned at 45 degrees to maximize signal to noise ratio of SHG. All tissue sections contained mainly parallel fibres and were contained in a single plane by the sample preparation to avoid any bias in measurements. This certifies that statistical differences are due to differences within groups and contributions from any source of experimental error are marginal.

4.4.3. Image post-processing and quantification

Figure 5 shows the distinctive biperiodic pattern of sarcomeres, imaged by means of SHG, and their characterization by three distances in unstained intact sarcomeres: resting

sarcomere length (SL), measured as the distance between the two Z-discs delimiting each sarcomere, and intra-sarcomeric A-band length (ABL), defined as the distance between the two intra-sarcomeric segments of the A-band, divided by the M-band. Additionally, since SHG arises from the thick-thin filament overlap in mature and developing sarcomeres [95], its length was calculated as the mean width of the A-band-related peak (namely in our study as thick-thin filament interaction length; TTIL). Additionally, a ratio between SL and ABL was calculated to further assess the quality of the acquired images and comparable physiological conditions between study groups. When the ratio ZZ/AA was above 2.25, the sample was excluded from the analysis since the typical SHG pattern of cardiac sarcomeres was lost. Measurements were retrieved after optimal fitting of a parametric model of the autocorrelation function for sarcomere fibers [84] and a custom made iterative fitting algorithm, that was developed by our research group [111], based in the curve fitting toolbox of Matlab to extract the average characteristic morphometric features of the sarcomere within a tissue section and from images acquired by standard SHG.

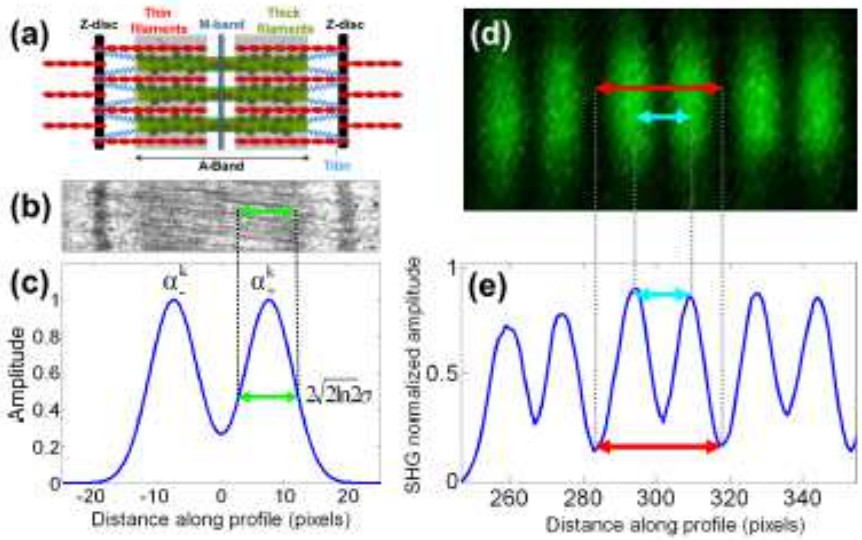

Figure 5. **SHG signal of sarcomere.** (a) Schematic representation of the elementary parts of a sarcomere, (b) an electron microscopy image of a sarcomere, (c) ideal SHG signal intensity profile along a sarcomere, (d) SHG image of a muscle fiber and (e) SHG intensity profile along the muscle fiber. Sarcomere Length (SL) is indicated by a red arrow, intrasarcomeric A-band length (ABL) by a blue arrow and thick-thin interaction length (TTIL) by a green arrow. [98]

Cardiac fibre tracking and single sarcomere detection and segmentation: Cardiac fiber tracking was achieved by computing local anisotropy of SHG images and standard streamline processing [112]. Subsequent sarcomere detection and segmentation was

achieved by combining the parametric sarcomere model and estimated cardiac fiber tracks. Visual inspection of images was enough to validate the accuracy of the method [111].

Other considerations: Sarcomere length in end-stage heart failure remains contentious [113] and some differences in the literature related to sarcomere morphometry might exist, due to (a) sample preparation which may reduce cell size up to 30% between alive and fixed status [85,114]; and (b) automated image quantification requires sufficient Signal to Noise Ratio (SNR), above 17dB for our methodology, to compute unbiased and unscaled measurements as noise, inhomogeneous illumination and fibre waving can produce errors. In any case, constant preparation and imaging conditions at specific SNR guarantee that statistical differences are real, although absolute values might not be fully correct.

4.5. Assessment of cardiac function (studies 2, 3 and 4)

4.5.1. Fetal echocardiography

Echocardiograhic measurements were performed in the experimental model of IUGR at the time of the cesarean section and in humans at diagnosis. A Vivid q (General Electric Healthcare, Horten, Norway) 1.4-2.5 MHz phased array probe was used for the animals and a Siemens Sonoline Antares (Siemens Medical Systems, Erlangen, Germany) or a Voluson 730 Expert (GE Medical Systems, Milwaukee, WI, USA) with 6-4 or 6-2 MHz curved array probes for humans. The angle of insonation was kept <30º in all measurements and a 70 Hz high pass filter was used to avoid slow flow noise. Echocardiographic evaluation included: (1) Ductus venosus pulsatility index (DVPI) obtained in a midsagittal section or transverse section of the fetal abdomen positioning the Doppler gate at its isthmic portion [115]; (2) Aortic isthmus pulsatility index (AoIPI) obtained in a sagittal view of the fetal thorax with a clear view of the aortic arch placing the sample volume between the origin of the last vessel of aortic arch and the aortic joint of the ductus arteriosus; (3) Left and right sphericity indeces calculated as base-to-apex length / basal ventricular diameter measured from 2-dimensional images in an apical 4-chamber view at end-diastole; (4) Left ventricular free wall thickness measured by M-mode in a transverse 4-chamber view; (5) Left ejection fraction estimated by M-mode from a transverse 4-chamber view according to Teicholz formula; (6) Longitudinal systolic (S') peak velocities at the mitral annulus measured by spectral tissue Doppler from an apical 4-chamber view; (7) left

myocardial performance index (MPI) obtained in a cross sectional image of the fetal thorax and an apical 4-chamber view, placing the Doppler sample volume on the medial wall of the ascending aorta including the aortic and mitral valve. The movements (clicks) of the valves in the Doppler trim were used as landmarks to calculate the isovolumetric contraction (ICT) and relaxation times (IRT), and the ejection time (ET). MPI was calculated as (ICT+IRT)/ET [116,117,118,119]; (8) diastolic ventricular filling (E/A) ratios: mitral and tricuspid E/A ratios were obtained in an apical 4-chamber view, with the Doppler sample volume just below the atrioventricular valves and calculated by dividing early diastolic (E) by atrial (A) peak inflow velocities [117]. Echocardiographic parameters were normalized into z-scores for gestational age [115,116,117].

4.5.2. Cardiovascular biomarkers in human fetal blood

Evaluation of the presence of cardiovascular biomarkers in humans was performed in fetal umbilical EDTA-treated blood, which was obtained from the umbilical vein after cord clamp at delivery in cases or at cardiocentesis in fetuses undergoing termination of pregnancy. All samples were processed within 1 hour. Plasma was separated by centrifugation at 1400g for 10 minutes at 4°C; samples were stored immediately at –80°C until assay. Cord blood levels of B-type natriuretic peptide (BNP) were measured with an immunoassay system (ADVIA Centaur BNP; Siemens Healthcare Diagnostics, Deerfield, IL), as previously described [120]. Troponin I levels were measured with commercially available assays from Centaur CP-troponin I assay (Siemens Healthcare Diagnostics).

4.5.3. Gene expression microarrays in rabbit hearts

In order to evaluate the cardiac gene expression profile of fetal IUGR and control rabbits, hearts were obtained through thoracotomy after anesthesia and immediately snap frozen and stored at -80ºC until use. The IUGR-gene expression profile was analyzed in 6 control and 6 IUGR rabbit fetuses. Total RNA was isolated from 40 mg of each left ventricle. The extraction protocol was a combination of TRIzol as reagent and the RNeasy Mini kit (Qiagen). RNA concentration and quality was determined in a Nanodrop spectrophotometer at 260/280 and 260/230 ratios**.** For each sample included in the study, the total amount of RNA was always above 25 μg with homogenous profile, showing a RNA integrity number

between 9.3 to 9.9 (analyzed with RNA 6000 Nano and Bioanalyzer 2100; Agilent). Next, 500 ng of total RNA from each sample were labeled with the Quick Amp One-color Labelling kit (Agilent) and fluorochrome Cy3. Efficiency of labeling (Cy3pmol/μg) was analyzed using a Nanodrop spectrophotometer to check that values were above the minimum requirements (>1.65 μg and > 9.0 pmols Cy3/ μg). Additionally, a RNA 6000 Nano mRNA assay in the Bioanalyzer 2100 was done in order to assess that all the samples show a comparable profile and fragments size was as expected (200-2000 bp). Then, 1650 μg of RNA obtained from each labeled sample were hybridized during 17 hours at 65ºC with an Agilent's Rabbit Microarray Kit 4x44k, P/N G2519F (Agilent Microarray Design ID 020908) containing 43,803 probe sequences obtained from the rabbit genome. All probe sequences included in the microarray were based on rabbit (*Oryctolagus cuniculus*) public transcript data. Finally, hybridization was quantified at 5 μm resolution (Axon 4000B scanner). Data extraction was done using Genepix Pro 6.0 software and results were subjected to bioinformatics analysis.

Data obtained from the microarray were subjected to two kinds of bioinformatics analysis. Firstly, a *differential expression analysis* in order to identify up- or down-regulated individual genes due to IUGR, and secondly, a functional interpretation of data using FatiScan for *gene set analysis* in order to identify gene modules or pathways with a coordinated over- or under-representation in IUGR.

Differential gene expression of the samples in each group was assessed with the adjusted P value for every gene included in the microarray and with the fold change. The analysis was carried out using the *limma* [121] package from Bioconductor (http://www.bioconductor.org/). Multiple testing adjustments of p-values were done according to Benjamini and Hochberg [122] methodology. All the pre-processing steps described can be carried out with the Babelomics software [123].

Gene set analysis was carried out for the Gene Ontology (GO) terms using the FatiScan (3) algorithm, implemented in the Babelomics suite (4). This method detects significantly up- or down-regulated blocks of functionally related genes in lists of genes ordered by differential expression. FatiScan can search for modules of genes that are functionally related by different criteria such as common annotations like GO terms. The FatiScan algorithm studies the distribution of functional terms across the list of genes coming from the microarray experiment, extracting significantly under- and over-represented GO terms in a

set of genes. GO terms were grouped in three categories: 1) cellular components, that refer to the place in the cell where a gene product is active; 2) biological processes, which refer to a biological objective to which a gene or gene product contributes and 3) molecular functions; that represent all the biochemical activities of a gene product. The core of the method proposed is based on an algorithm to test whether a set of genes, labeled with terms (biological information), contain significant enrichments on one or several of these terms with respect to another set of genes of reference. FatiScan uses a Fisher's exact test for 2×2 contingency tables for comparing two groups of genes and extracting a list of GO terms whose distribution among the groups is significantly different. Given that many GO terms are simultaneously tested, the results of the test are corrected for multiple testing to obtain an adjusted p-value. FatiScan returns adjusted p-values based the False Discovery Rate (FDR) method [122]. GO annotation for the genes in the microarray where taken from the Blast2GO Functional Annotation Repository web page (http://bioinfo.cipf.es/b2gfar/). The raw microarray data have been deposited in the Gene Expression Omnibus database under accession number GSE37860.

4.6. Statistical analysis

Data was analyzed using the statistical package SPSS 18.0 (SPSS, Chicago). P values below 0.05 were considered statistically significant. Data are expressed as mean ± SD or median (interquartile range, IQR) as appropriate. Statistical significance of differences between groups was compared with unpaired two-tailed t-test or Mann-Whitney test, depending whether variables followed or not a normal distribution.

5. STUDIES

5.1. STUDY 1

Whole heart detailed and quantitative anatomy, myofiber structure and vasculature from X-ray phase-contrast synchrotron radiation-based micro-CT.

Gonzalez-Tendero A, Zhang C, Cárdenes R, Balicevic V, Loncaric S, Butakoff C, Paun B, Bonnin A, Gratacós E, Crispi F, Bijnens B.

Status: In preparation

Results from this study have been presented or accepted for presentation in:

1. Gonzalez-Tendero A, Cárdenes R, Zhang C, Bonnin A, Demicheva E, Gratacós E, Crispi F, Bijnens B. X-ray phase-contrast synchrotron radiation-based micro-CT to study detailed cardiac anatomy, myofiber structure and vasculature of a rodent heart. European Society of Cardiology Congress, Barcelona, Spain. August 2014. Poster.

2. Gonzalez-Tendero A, Zhang C, Balicevic V, Cárdenes R, Loncaric S, Bonnin A, Gratacós E, Crispi F, Bijnens B. X-ray phase-contrast synchrotron radiation-based micro-CT enables assessment of fetal cardiac anatomy, fiber orientation and vasculature in a rabbit model of intrauterine growth restriction. Frontiers in Cardiovascular Biology, European Society of Cardiology. Barcelona, Spain. July 2014. Poster.

3. Gonzalez-Tendero A, Cárdenes R, Butakoff C, Paun B, Zhang C, Bonnin A, Crispi F, Gratacós E, Bijnens B. X-ray phase-contrast synchrotron radiation-based micro-CT of a whole rodent heart for the assessment of detailed anatomy, myofiber structure and vasculature. 3rd European Conference on Whole Slide Imaging and Analysis, Heidelberg. November 2013. Poster.

Whole heart detailed and quantitative anatomy, myofiber structure and vasculature from X-ray phase-contrast synchrotron radiation-based micro-CT

Anna Gonzalez-Tendero[1], Chong Zhang[2,3], Rubén Cárdenes[1,2], Vedrana Balicevic[4], Sven Loncaric[4], Constantine Butakoff[2], Bruno Paun[2], Anne Bonnin[5], Eduard Gratacós [1], Fatima Crispi[1], Bart Bijnens[2,6]

[1]BCNatal - Barcelona Center for Maternal-Fetal and Neonatal Medicine (Hospital Clínic and Hospital Sant Joan de Deu), IDIBAPS, University of Barcelona, and Centre for Biomedical Research on Rare Diseases (CIBER-ER), Barcelona, Spain; [2]PhySense, DTIC, Universitat Pompeu Fabra, Barcelona, Spain; [3]CellNetworks, Heidelberg, Germany [4]Faculty of Electrical Engineering and Computing, University of Zagreb, Zagreb, Croatia; [5]European Synchrotron Radiation Facility, Grenoble, France; [6]ICREA, Barcelona, Spain

Address for correspondence:

Prof. Bart Bijnens
Institució Catalana de Recerca i Estudis Avançats (ICREA)
Carrer de Tànger, 122-140
ES–08018 Barcelona (Spain)
Tel. +34 61 501 6853
e-mail: bart@bijnens.com

Wordcount: 3243 words

ABSTRACT

Background: Cardiovascular diseases often become symptomatic only after a long process of subclinical remodelling. Early detection of these subtle changes is crucial for diagnosis and prevention. Including computational modelling, requires knowledge on the multi-scale structure of the whole heart and major vessels. While individual cardiomyocytes only have a limited ability to shorten, the heart efficiently pumps a large volume-fraction thanks to a complex cell organisation in a complex 3D fibre structure.

Methods: we developed a fast acquisition together with visualisation and quantification methods of the integrated microstructure of whole hearts using synchrotron based X-ray (phase-contrast) tomography. We have been able to extend the information to include not only X-ray absorption by the tissue, but also wave propagation phenomena when propagating trough structures We used normal rat hearts to validate the technique and fetal rabbit hearts suffering intrauterine growth restriction as a model of subclinical cardiac remodelling

Results and conclusions: we have developed a novel, high resolution, image acquisition and quantification approach to study a whole heart at myofibre resolution, providing integrated 3D structural information at microscopic level without need of slide processing. This opens up new possibilities for a systems approach towards cardiac function, providing fast acquisition of quantitative microstructure the heart in a near native state.

INTRODUCTION

Cardiovascular diseases often become symptomatic only after a long process of sub-clinical remodelling where structural or functional changes are occurring in the complex substructures of the heart.

While for clinical and research purposes, the heart chambers are often simplified to ellipsoid-like volumes, in reality, the shape is variable and the endocardial wall shows complex trabeculations, contributing to volume ejection and guiding Purkinje fibres. Additionally, intracavitary structures, such as the valve apparatuses, with papillary muscles and tendinous chordea as well as false tendons, guiding Purkinje cells, are present. And while individual cardiomyocytes only have a limited ability to shorten, the heart efficiently pumps a large volume-fraction thanks to a complex cell organisation in a complex 3D fibre structure. This structure is additionally interlinked with a coronary tree starting from a few epicardial arteries, which branch into a complex vascular network while penetrating the myocardial wall.

While several genetic cardiomyopathies, such as Hypertrophic Cardiomyopathy, or fibrosis, will majorly change local microstructure, more subclinical conditions only show subtle changes. An example of this is intrauterine growth restriction (IUGR) due to placental insufficiency, affecting 7-10% of all pregnancies and a major cause of perinatal mortality and long-term morbidity[1,2]. Low birth weight, most likely due to IUGR is strongly associated with increased risk of cardiovascular mortality in adulthood[3]. Fetal hypoxia and volume/pressure overload induces cardiac remodelling which is mainly characterized by signs of decreased longitudinal motion and impaired relaxation (diastolic dysfunction) from the early stages of deterioration[4,5,6]. The fetal immature heart is very plastic and remodelling of the microstructure might be expected. The three dimensional cardiac and cardiomyocyte architecture and organization are established early in prenatal life[7]. However, given the high plasticity, little is known about the changes of cardiac architecture during cardiac development and under altered haemodynamic conditions.

IUGR also induces adaptive changes to the coronary vascular tree, which which even may predispose for adult coronary disease[8,9,10]. Doppler evaluation of severe IUGR human fetuses has shown changes in coronary flow[10]. It has been observed that the coronary tree responds to conditions of chronic hypoxemia by a substantial increase in the cross-sectional area of the coronary tree[8] or by increasing coronary vessel growth and myocardial vascularization[11].

Therefore, for understanding disease progression and gradual remodelling, integrating information on individual cells to their spatial organisation in fibres and the myocardium, together with the supporting structure is essential

While a lot is known about cardiac (cellular) physiology and regional microstructure, translating this towards clinical medicine, based on imaging, is still a challenge. For this, a translational approach based on systems medicine, integrating multiple scales, has been proposed. Additionally, many efforts towards computational modelling of the cardiovascular system are actively developed. For these initiatives, detailed knowledge on the whole heart 3D morphology, integrating all the substructures present at a resolution that includes all relevant details, is essential.

The myocardium is made of millions of cardiomyocytes that are aggregated together as a three-dimensional mesh within a supporting matrix of fibrous tissue [12,13]. Cardiomyocytes are arranged in a very specific way within ventricular walls, forming the fibers. The organization of the fibers within the walls creates the cardiac geometry with a specific curvature and thickness. This complex cell organisation is what allows the heart to efficiently pump a large volume-fraction, since cardiomyocytes can only maximally shorten by 10-15% [14].

Myocytes are aggregated and aligned in a predominant direction, depending on their position with the myocardial wall[13]. At the epicardium as well as the endocardium, they are aligned tangential with a predominant longitudinal (base-apex) direction, while in the mid-myocardium they are predominantly circumferential. The change in angulation relative to the ventricular equator (helical angle) is gradual and the helical angle in the epicardial layers is opposite to the helical angle in the subendocardial layers[15,13], and tends to approach 90° at the endocardium and -90° at the epicardium[16].

The cardiac contraction, in terms of motion, results from a complex three-directional movement that involves longitudinal contraction, circumferential contraction as well as rotation/twisting[17]. The regional deformation is determined by the complex three-dimensional organization of the fibers within the cardiac walls.

Several studies provide evidence of the strong relationship between regional cardiac architecture, myofiber alignment and cardiac function.

The normal 3D fiber architecture in embryonic and fetal myocardium has been studied using polarized light microscopy and laser scanning confocal microscopy[18,19,20]. Tobita et al. showed that during normal development, in the left ventricle myocardium, fiber angle distribution changed from a uniform transmural circumferential orientation to a gradual transmural shift in orientation from circumferential (endocardium) to longitudinal (epicardium)[20]. Fiber orientation is sensitive to

changes in mechanical load[21]. When there is a reduction in the mechanical load, the left ventricle undergoes a hypoplasic adaptation and transmural variation of fiber angle results to be immature. On the contrary, an increased mechanical load induces ventricular hyperplasia and an acceleration of fiber maturation[20].

Thus, linking information on the microstructure of the myocardium and its spatial organization is essential for understanding the functioning of the whole organ and remodelling induced by disease. Several techniques have been used to study e.g. the fiber organization, both trough direct visualisation (microscopy or high resolution micro-MRI/CT) or trough inference by assessing local tissue properties (e.g. diffusion tensor MRI or echocardiography). However, detecting the orientation of individual cardiomyocytes, especially in larger tissue volumes or the whole heart, is still a major challenge[22,23]. Histology and optical microscopy provide sufficient detail, but hardly allow to image whole hearts, and slicing/processing is required, which is a source of artefacts on the actual cardiac micro-structure[18,19]. High resolution/field strength MRI (including DTI)[24,25,26] has been attempted, but special resolution is still suboptimal (~50 micron) and scan times are extremely long. Micro CT, after iodine staining, shows some promise[27,28], but organ preparation is very challenging and extracting the integrated microstructure, including myofibres and vessels is hardly feasible.

In this study we propose an integrated, high resolution, image acquisition and quantification approach to study whole hearts at myofiber resolution, providing structural information at microscopic level without need of slice processing. The imaging is based on X-ray phase-contrast synchrotron radiation-based micro-CT[29]. Phase-contrast imaging with synchrotron radiation has emerged as a novel X-ray-based imaging approach providing enhanced image contrast in some biological tissues and additionally suggesting the potential to improve the diagnostic work-up[30]. Varray et al. studied small samples of human myocardium acquired at 3.5 microns resolution, showing the ability to resolve fibre structures.

MATERIAL AND METHODS

Organ preparation

New Zealand white rabbits and Wistar rats were provided by a certified breeder. Animal handling and all procedures were performed in accordance to applicable regulations and guidelines and with the approval of the Animal Experimental Ethics Committee of the University of Barcelona. A validated experimental model of IUGR in New Zealand White pregnant rabbit was reproduced[31]. Briefly, at 25 days of gestation a midline laparatomy was performed, both uterine horns were exteriorized and one horn was randomly considered as IUGR while the other was considered as the normal control growth horn, in which no procedure was performed. In all gestational sacs from the IUGR horn, a selective ligature of the 40-50% of the uteroplacental vessels of each gestational sac was performed. After the procedure, the abdomen was closed and animals were kept in regular conditions and fed a diet of standard rabbit chow and water *ad libitum.* At 30 days of gestation, a caesarean section was performed and all living rabbit kits were obtained. After anaesthesia induction with an intramuscular injection of ketamine and xylazine, the kits' chest was opened to expose the heart and abdominal aorta. Heparin 500 U was administered through the aorta as well as saturated KCl to arrest hearts in diastole. The abdominal aorta was cannulated and connected to a perfusion pump. A phosphate buffer saline solution was passed through the circulation to rinse blood and subsequently a 10% neutral buffered formalin solution to fix the heart. The same procedure was followed for heart fixation of young Wistar rats (25 days old), after anaesthesia induction with inhaled isofluorane. Hearts were then excised from the animal, immersed in 10 % formalin solution and stored at 4ºC until processing.

Before imaging, hearts were dehydrated with increasing ethanol concentrations from 10% to 80% in 10% steps. In order to avoid movement artifacts, hearts were immobilized in a 1% agarose solution into a tube that fitted the size of the heart and the size of the sample holder.

Image acquisition

Phase contrast projection images were acquired at the ESRF beamline ID19, using a X-ray energy of 19Kev, and a propagation distance between the object and the camera of 1100mm, obtaining a field of view of 5,68x15,96 mm, and an isotropic pixel size of 7.43µm. The sample, maintained inside a tube at room temperature, was placed on top of a holder, and was positioned remotely at the center of the beamline. Then, the sample was rotated 360 degrees acquiring a total of 2499 projections during the whole rotation. The exposure time for each projection was 0.3 seconds and the total time of each rotational acquisition was 14 minutes. Four to five rotational acquisitions were necessary to fully cover the whole heart along its long axis. These acquisitions were taken sequentially with an overlap of 363 slices (2,697mm) always from base to apex. After each

acquisition, a set of 41 reference flat field images (with the sample removed), and 21 dark images (with sample removed and shutter closed) were taken for background removal. Therefore, total acquisition time was approximately 1h or 1,25h/sample in case of 4 or 5 different chunks were necessary respectively.

Each projection series was reconstructed at the ESRF computing facilities using a state of the art filtered backprojection approach as well as the method described in Paganin et al[32]. The reconstructed volumes were then converted to 16 bits tiff image series, merged into a single dataset, and cropped to the desired region of interest. In all cases the whole heart was kept in the resulting 3D dataset. Images were analysed with Fiji (reslicing/rendering) [33], ICY (rendering)[34] and Ilastik (vessel segmentation)[35] and in-house developed software for fibre analysis based on Matlab[36].

RESULTS

All reconstructed 3D datasets covered the whole heart and provided 3D details not available up to now. One young rat heart, one normal rabbit fetal heart and 1 IUGR fetal heart was processed.

Figure 1a shows the images obtained from the rat heart. The left part of the figure shows some originally reconstructed short axis slices at aortic valve and mid ventricular level, as well as a longitudinal reslice trough the aortic valve and apex. The cardiac substructure can be clearly differentiated (atria, ventricles, great vessels and valves). Intramural vessels as well as local fibre directions can be recognised. When visualising data using volume rendering (right part of the figure), the detailed architecture of the tricuspid valve apparatus and aortic valve can be clearly visualized. Additionally, details of local complexity of the walls (such as pectinate muscles in the atria) and part of the vasculature, is visible.

Figure 2 shows a detailed view of part of the aortic wall (top) as well as from the RV and LV wall (bottom). In the aortic wall, spiral like structures can be seen, corresponding to the elastine providing its support and elasticity. In the muscle walls, besides clearly visible vessels, predominant directions in the muscle can be observed. Longitudinally oriented cell aggregates show as dot-like structures in the short-axis cut, while circumferential fibres are line-like. From this, it can be clearly seen that in the LV, in the epicardial as well as in the endocardial side, fibres are predominantly longitudinal while in the mid-wall, they are more circumferential. However, in the RV, 2 rather than 3 directions can be seen, with the longitudinal fibres mainly at the endocardial side.

Video 1 provides a visualisation of the (edge-enhanced) whole heart dataset of the rat from the short-axis slices. The intramural course of the coronary vessels is easily traceable and the oblique course of the fibres gives the impression of flow within the myocardium with different direction at both edges of the walls. The spiral like arrangement towards the apex is clearly shown.

Figure 3 shows surface rendered images of cutes trough the two fetal hearts. The IUGR heart (right) is clearly smaller than the normal one (left). Additionally, the coronaries are clearly dilated and much more prominent in the IUGR heart. In the RV cut (bottom), both the chordal as well as the false tendons can be easily depicted.

Figure 4 (and video 2) shows the segmented arterial trees for both rabbit hearts (top) as well as a visualisation of the local radius of the vessels (bottom) where the dilatation of the coronary arteries in IUGR can be clearly observed and quantified.

Figure 5 (left) shows the local helix angle of the fibres within a slice of the rabbit myocardial wall with a visualisation of the resulting 3D fibre structure at the right. The gradual change from predominantly longitudinal at the epicardial side, towards more circumferential in the mid-

myocardium and again longitudinal at the epicardial side of the left ventricle can be observed. A rather abrupt change in the mid of the interventricular septum is present. In IUGR, predominantly in the RV wall, there seems a reduction in the longitudinally oriented fibres with more predominance of the circumferential ones.

DISCUSSION

In this paper we described a comprehensive, integrated approach for the non-destructive acquisition, visualisation and quantification of the structure of a whole heart at almost cell-like resolution.

This approach allows fast imaging of whole hearts to quantitatively describe and compare morphological remodelling of all substructures within the different components of the heart. Both myocardial tissue and vessels can be extracted and interrelated from the same dataset, with the ability to extract the local orientation of myocytes (=myofibres) and relate it to location within the wall and the surrounding vasculature. Additionally, global chamber geometry, including detailed visualisation of trabeculations and (false) tendons is provided.

These datasets provide a unique source of information where tissue properties can be quantified and compared within the 3D structure for purposes of describing changes induced by genetic or acquired disease, even if the remodelling present is subtle and not detectible by current imaging modalities. Additionally, the data is of sufficient detail to serve as input for computational modelling studies of whole hearts without the need for adding additional virtual substructures.

To illustrate the potential of the novel approach, besides a normal heart, we also scanned a control and an IUGR fetal rabbit heart. Firstly, the resolution and lack of complicated processing, enables to study the micro-architecture of the fetal heart, which is challenging otherwise. Additionally, we have shown that the integrated assessment of organ morphology, vasculature and fibre structure provides a way to quantify subtle (sub-clinical) remodelling induced in-utero, beyond gross changes induced by genetic alteration. We have observed that, while the whole heart is smaller, the coronary arteries are clearly dilated due to the haemodynamic challenge induced by hypoxia and hyponutricia in IUGR. Additionally, the gradual change of fibre direction can be quantified and preliminary data points towards an alteration of its transmural course.

The richness of the data, together with the resolution and the image contrast, allows the use of state-of-the-art medical image analysis tools to quantify and visualise the different substructure of the whole 3D dataset of the heart. To extract the coronary tree, we proposed a machine learning based approach where the image appearance is learned from a couple of slices and the algorithm (implemented in Ilastik, an open-source project providing a user-friendly tool for image classification and segmentation) is able to extract the vessel structure. The ability to discriminate the local predominant direction of the myocyte aggregates in the images allows for a quantification of the transmural fibre direction by extracting the 3D components of the local structural tensor using traditional gradient calculations together with fibre tracking approaches as have been developed for applications based on DT MRI. This allows the optimal re-use of the vast spectrum of image

analysis tools, while offering the possibility to combine approaches from high-resolution data with techniques developed for lower resolution (clinical) imaging modalities.

Additionally, both the superior resolution as well as the fact that all substructures can be recognised and segmented while originating from single 3D dataset, enables to obtain the structural data that is required for performing computational modelling of the whole heart as a functional organ. Current approaches often get overall geometry from imaging, but have to incorporate e.g. the fibre structure from statistical models that were developed from microscopy data since high-resolution non-destructive fibre visualisation was not possible up to now. This offers a wealth of new possibilities to improve the computational models, especially towards more individual simulations and comparing control and pathological specimens.

The imaging is based on phase-contrast CT, as provided by some beamlines present in contemporary synchrotron radiation facilities. X-ray based imaging is currently the only non-destructive approach that provides the resolution needed to resolve details that approach the size of individual myocytes (<10 micron). While some microCTs can provide this resolution required, X-ray absorption imaging does not provide the contrast needed to discriminate the microstructural details within cardiac tissue. Vessels and fibres can only be detected when a contrast agent is perfused throughout the tissue. However, this is a highly artefact prone procedure since a homogeneous distribution of contrast along myofibres and within the vasculature is very challenging. However, phase-contrast X-ray imaging provides a way to not only quantify the local X-ray absorption, but additionally capture wave propagation phenomena that enhance subtle differences in tissue properties and enable to provide contrast between tissue and vessels as well as to capture details on the local predominant direction of the myfibres. Therefore, phase-contrast imaging is far superior to (contrast-enhance) X-ray absorption imaging when studying the microstructure of the heart. While a lot of research is going on to enable phase contrast imaging based on more traditional CT systems[37,38], currently, high resolution phase contrast X-ray imaging is only available in synchrotron based light sources. Phase contrast imaging is an expanding field within several synchrotron facilities and has shown great promise for non-destructive visualisation and quantification of samples from different origins and application fields (paleontology[39], biological samples[40], materials[41],…). Extending the use of these large-infrastructure research facilities, funded by national and international research organisation, towards cardiac applications opens up new possibilities for studying cardiovascular development, pathophysiological remodelling and therapeutic targets.

In conclusion, we have developed a novel, high resolution, non-destructive approach towards visualising and quantifying the microstructure of whole hearts at myofiber resolution, providing structural information at microscopic level without need of slice processing. This opens up new

possibilities for a systems medicine approach towards cardiac remodelling, providing fast acquisition of the heart in a near native state without processing artefacts.

In this report, we describe some preliminary results, mainly focussing on the direct visualisation of datasets and quantification of remodelling induced by intra-uterine growth restriction.

ACKNOWLEDGMENTS

We acknowledge the European Synchrotron Radiation Facility for provision of synchrotron facilities.

REFERENCES

1. Alberry M, Soothill P. Management of fetal growth restriction. *Arch Dis Child Fetal Neonatal Ed*. 2007;**92**:F62-7.
2. Figueras F, Gratacós E. Update on the Diagnosis and Classification of Fetal Growth Restriction and Proposal of a Stage-Based Management Protocol. *Fetal Diagn Ther*. 2014. *In press.*
3. Barker DJ, Osmond C, Golding J, Kuh D, Wadsworth ME. Growth in utero, blood pressure in childhood and adult life, and mortality from cardiovascular disease. *BMJ*. 1989;**298**:564-7.
4. Crispi F, *et al*. Cardiac dysfunction and cell damage across clinical stages of severity in growth-restricted fetuses. *Am J Obstet Gynecol*. 2008;**199**:254.e1-8.
5. Crispi F, Gratacós E. Fetal cardiac function: technical considerations and potential research and clinical applications. *Fetal Diagn Ther*. 2012;**32**:47-64.
6. Verburg BO, *et al*. Fetal hemodynamic adaptive changes related to intrauterine growth: the Generation R Study. *Circulation*. 2008;**117**:649-59.
7. Zhang L, *et al*. Cardiomyocyte architectural plasticity in fetal, neonatal, and adult pig hearts delineated with diffusion tensor MRI. *Am J Physiol Heart Circ Physiol*. 2013;**304**:H246-52.
8. Thornburg KL, Reller MD. Coronary flow regulation in the fetal sheep. *Am J Physiol.* 1999;**277**:R1249-60.
9. Chaoui R. Coronary arteries in fetal life: physiology, malformations and the "heart-sparing effect". *Acta Paediatr Suppl*. 2004;**93**:6-12.
10. Baschat A, Gembruch U. Evaluation of the fetal coronary circulation. *Ultrasound Obstet Gynecol*. 2002;**20**:405-12.
11. Thompson LP. Effects of chronic hypoxia on fetal coronary responses. *High Alt Med Biol*. 2003;**4**:215-24.
12. Anderson RH, Ho SY, Redmann K, Sanchez-Quintana D, Lunkenheimer PP. The anatomical arrangement of the myocardial cells making up the ventricular mass. *Eur J Cardiothorac Surg*. 2005;**28**:517-25.
13. Anderson RH, Smerup M, Sanchez-Quintana D, Loukas M, Lunkenheimer PP. The three-dimensional arrangement of the myocytes in the ventricular walls. *Clin Anat.* 2009;**22**:64-76.
14. Sonnenblick EH, Ross J Jr, Covell JW, Spotnitz HM, Spiro D. The ultrastructure of the heart in systole and diastole. Changes in sarcomere length. *Circ Res.* 1967;**21**:423-31.
15. Henderson DJ, Anderson RH. The development and structure of the ventricles in the human heart. *Pediatr Cardiol*. 2009;**30**:588-96.
16. Streeter DD Jr, Spotnitz HM, Patel DP, Ross J Jr, Sonnenblick EH. Fiber orientation in the canine left ventricle during diastole and systole. *Circ Res*. 1969;**24**:339-47.
17. Bijnens B, Cikes M, Butakoff C, Sitges M, Crispi F. Myocardial motion and deformation: What does it tell us and how does it relate to function? *Fetal Diagn Ther*. 2012;**32**:5-16.
18. Jouk PS, Usson Y, Michalowicz G, Grossi L. Three-dimensional cartography of the pattern of the myofibres in the second trimester fetal human heart. *Anat Embryol (Berl).* 2000;**202**:103-18.

19. Jouk PS, *et al*. Analysis of the fiber architecture of the heart by quantitative polarized light microscopy. Accuracy, limitations and contribution to the study of the fiber architecture of the ventricles during fetal and neonatal life. *Eur J Cardiothorac Surg*. 2007;**31**:915-21.
20. Tobita K, Garrison JB, Liu LJ, Tinney JP, Keller BB. Three-dimensional myofiber architecture of the embryonic left ventricle during normal development and altered mechanical loads. *Anat Rec A Discov Mol Cell Evol Biol*. 2005;**283**:193-201.
21. Arts T, Delhaas T, Bovendeerd P, Verbeek X, Prinzen FW. Adaptation to mechanical load determines shape and properties of heart and circulation: the CircAdapt model. *Am J Physiol Heart Circ Physiol*. 2005;**288**:H1943-54.
22. Mekkaoui C, *et al*. Fiber architecture in remodeled myocardium revealed with a quantitative diffusion CMR tractography framework and histological validation. *J Cardiovasc Magn Reson.* 2012;**14**:70.
23. Mekkaoui C, *et al*. Diffusion MRI tractography of the developing human fetal heart. *PLoS One.* 2013; **8**:e72795.
24. Gilbert SH, *et al*.. A framework for myoarchitecture analysis of high resolution cardiac MRI and comparison with diffusion tensor MRI. *Conf Proc IEEE Eng Med Biol Soc*. 2012; **2012**:4063-6.
25. Healy LJ, Jiang Y, Hsu EW. Quantitative comparison of myocardial fiber structure between mice, rabbit, and sheep using diffusion tensor cardiovascular magnetic resonance. *J Cardiovasc Magn Reson.* 2011;**13**:74.
26. Scollan DF, Holmes A, Zhang J, Winslow RL. Reconstruction of cardiac ventricular geometry and fiber orientation using magnetic resonance imaging. *Ann Biomed Eng*. 2000;**28**:934-44.
27. Aslanidi OV, *et al*. Application of micro-computed tomography with iodine staining to cardiac imaging, segmentation, and computational model development. *IEEE Trans Med Imaging.* 2013;**32**:8-17.
28. Stephenson RS, *et al*. Contrast enhanced micro-computed tomography resolves the 3-dimensional morphology of the cardiac conduction system in mammalian hearts. *PLoS One*. 2012;**7**:e35299.
29. Betz O, *et al*. Imaging applications of synchrotron X-ray phase-contrast microtomography in biological morphology and biomaterials science. I. General aspects of the technique and its advantages in the analysis of millimetre-sized arthropod structure. *J Microsc*. 2007;**227**:51-71.
30. Weitkamp T, *et al*. X-ray phase radiography and tomography of soft tissue using grating interferometry. *Eur J Radiol*. 2008;**68**:S13-7.
31. Eixarch E, *et al*. An experimental model of fetal growth restriction based on selective ligature of uteroplacental vessels in the pregnant rabbit. *Fetal Diagn Ther.* 2009;**26**: 203-211.
32. Paganin D, Gureyev TE, Mayo SC, Stevenson AW, Nesterets YI, Wilkins SW. X-ray omni microscopy. *J Microsc*. 2004;**214**:315-27.
33. Schindelin J, *et al*.. Fiji: an open-source platform for biological-image analysis. *Nat Methods*. 2012;**9**:676-82.
34. de Chaumont F, *et al*. Icy: an open bioimage informatics platform for extended reproducible research. *Nat Methods*. 2012;**9:**690-696.
35. Sommer C, Straehle C, Köthe U, Hamprecht FA. 8th IEEE International Symposium on Biomedical Imaging (ISBI 2011), *in press*.
36. Mathworks 2007b, version 7.5.0.342; MATLAB, The MathWorks Inc., Natick, Massachusetts, USA.

37. Auweter SD, *et al*. X-ray phase-contrast imaging of the breast--advances towards clinical implementation. *Br J Radiol*. 2014;**87**:20130606.
38. Hetterich H, *et al*. Phase-Contrast CT: Qualitative and Quantitative Evaluation of Atherosclerotic Carotid Artery Plaque. *Radiology*. 2014;131554. *In press*.
39. Sanchez S, *et al*. 3D microstructural architecture of muscle attachments in extant and fossil vertebrates revealed by synchrotron microtomography. *PLoS One*. 2013;**8**:e56992.
40. Kim J, *et al*. Altered branching patterns of Purkinje cells in mouse model for cortical development disorder. *Sci Rep*. 2011;**1**:122.
41. Baruchel J, Lodini A, Romanzetti S, Rustichelli F, Scrivani A. Phase-contrast imaging of thin biomaterials. *Biomaterials*. 2001;**22**:1515-20.

FIGURE CAPTIONS

Figure 1. X-ray phase-contrast synchrotron radiation-based micro-CT imaging of a rat heart. Details of cardiac anatomy can be observed with great detail and resolution: fiber orientation, aortic and tricuspid valves, false tendon or right ventricle moderator band. When doing volume rendering of the images, details of aortic or tricuspid valve can be observed; as well as the atrial pectinate muscles.

Figure 2. Detail of the aortic wall and the ventricular walls of a rat heart. In the aortic wall layers can be distinguished; whereas in the ventricular walls, orientation of fibers can be determined and classified as circumferential (circ) or lonigtudinal (long).

Figure 3. Volume rendered images depicting detailed cardiac anatomy of an IUGR and a control heart. IUGR fetal heart (top right) is smaller and with thinner walls compared to the control fetal heart (top left). Additionally, it can be appreciated that the coronary vessels are clearly dilated and much more prominent in the IUGR heart. In the bottom, detail of the right ventricle cavity from both hearts.

Figure 4. Segmentation of the coronary vascular tree. Coronary vascular tree can be visualized in detail when segmented (top). The differences between control and IUGR rabbit fetal hearts result even more evident when the segmentation of the coronary vessels is visualized as a quantification of the local radius of the vessels (bottom). Lighter colours mean bigger diameters; therefore the dilatation of the coronary arteries in IUGR is clearly visible.

Figure 5. Fiber orientation in myocardial walls. Fiber angle change across the walls within a slice in fetal rabbit control (top left) and IUGR (bottom left) hearts. Fiber angle change from endo- to epi-cardium from +90º to -90º. A visualisation of the resulting 3D fibre structure at the right.

FIGURES

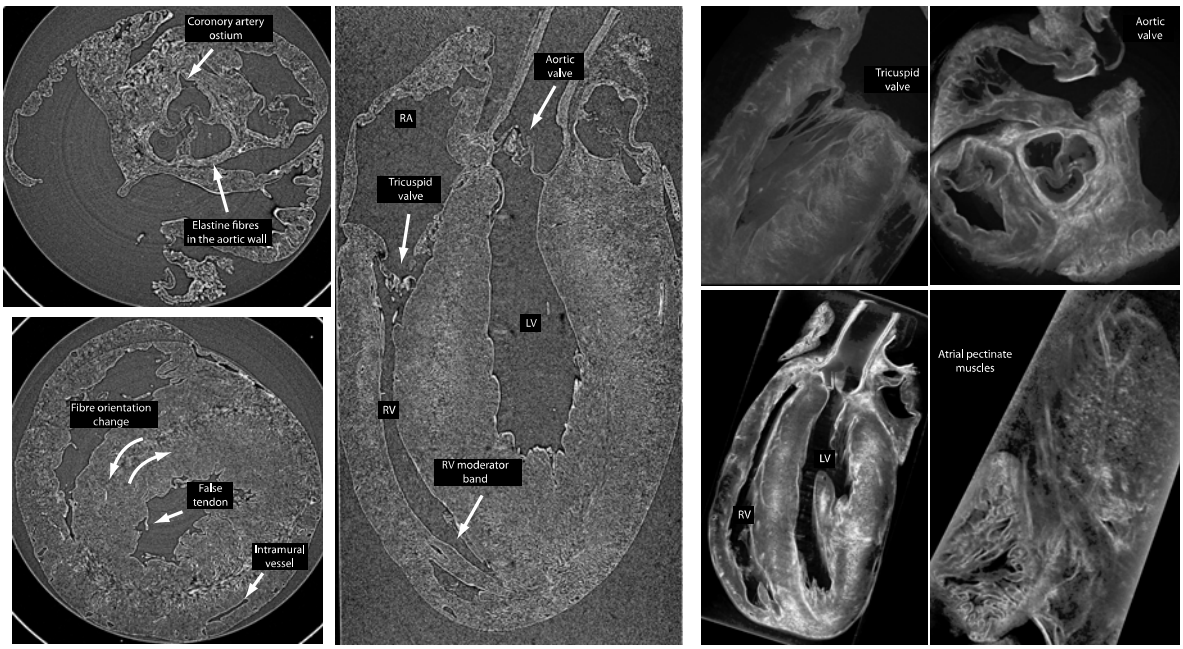

Figure 1

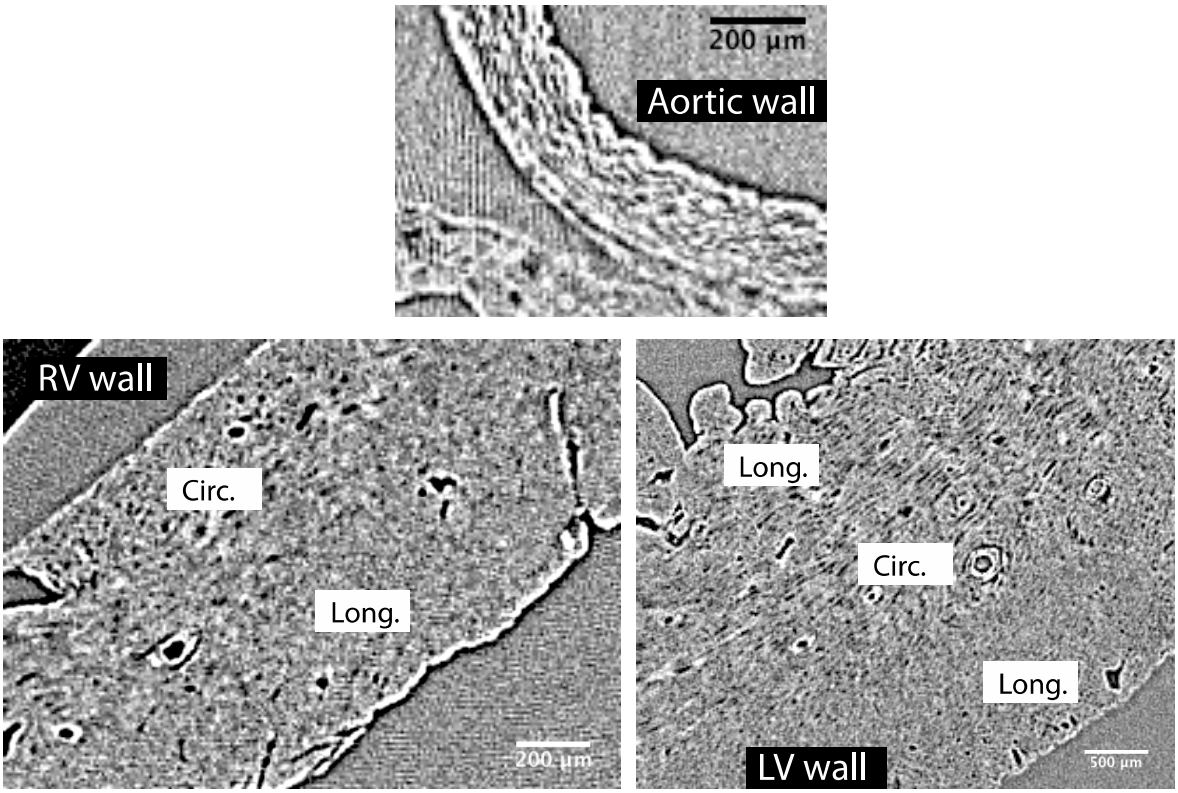
200 µm
Aortic wall
RV wall
Circ.
Long.
200 µm
Long.
Circ.
Long.
LV wall
500 µm

Figure 2

Figure 3

CONTROL

IUGR

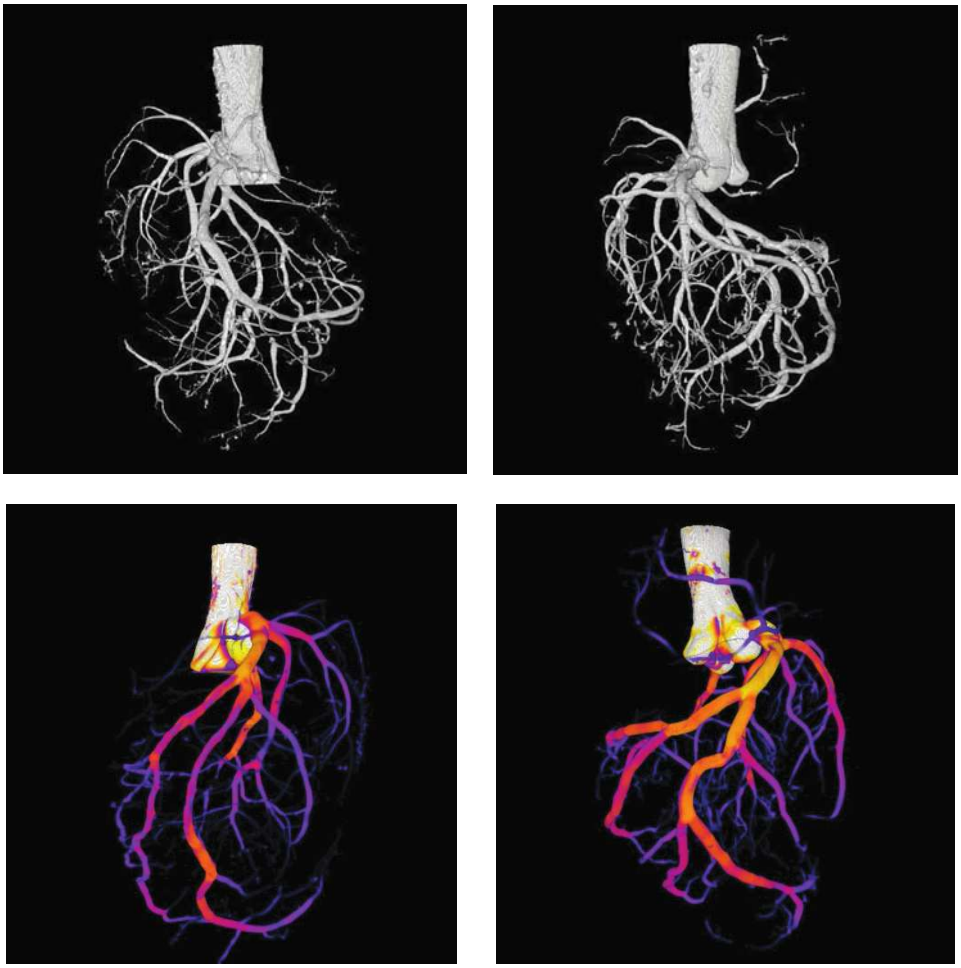

Figure 4

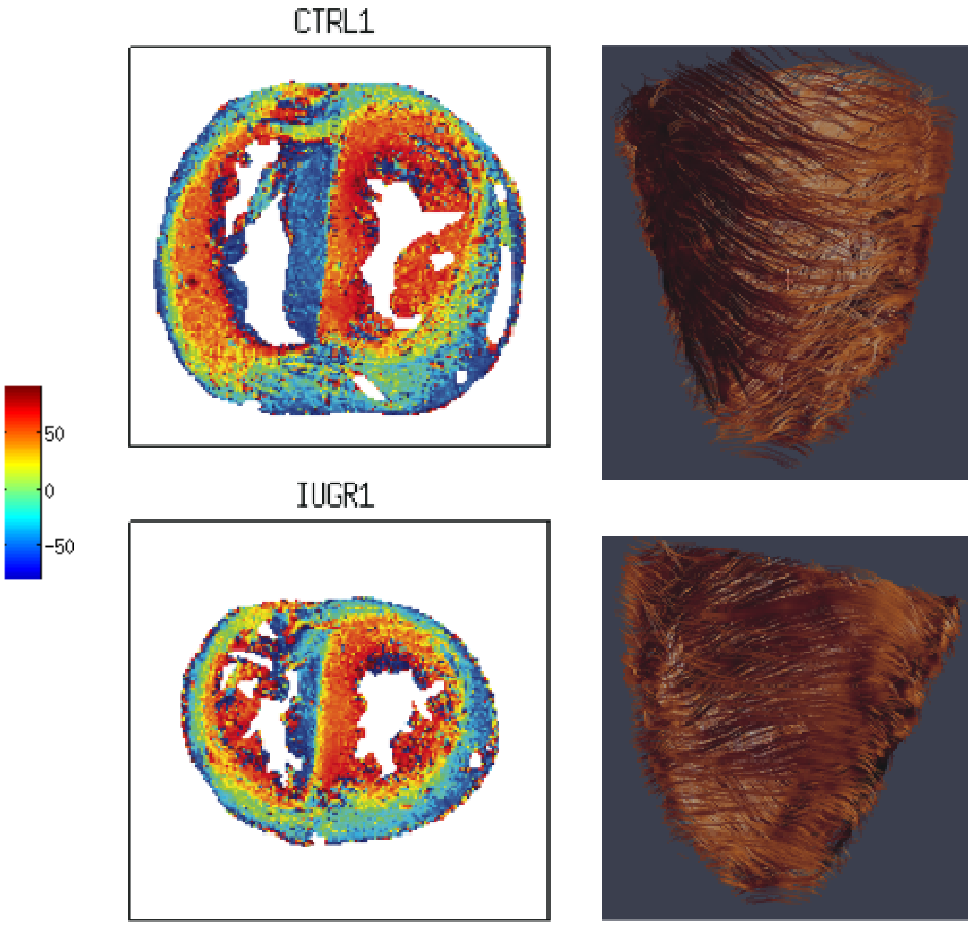

Figure 5

5.2. STUDY 2

Intrauterine growth restriction is associated with cardiac ultrastructural and gene expression changes related to the energetic metabolism in a rabbit model.

Gonzalez-Tendero A, Torre I, Garcia-Canadilla P, Crispi F, García-García F, Dopazo J, Bijnens B, Gratacós E. Am J Physiol Heart Circ Physiol. 2013; 305: H1752–H1760.

Status: Published.

Journal Impact Factor: 3.629

Quartile: 1st

Results from this study have been presented in

1. Gonzalez-Tendero A, Torre I, Garcia-Canadilla P, Crispi F, Amat-Roldan I, Hove-Madsen L, Llach A, García-García F, Dopazo J, Bijnens B, Gratacós E. Effects of intrauterine growth restriction on cardiomyocyte structure and function in a rabbit model. Mitochondria, calcium and the heart Minisymposium. Graz, Austria. April 2013. Poster.

2. Gonzalez-Tendero A, Torre I, Garcia-Garcia F, Dopazo J, Gratacós E. Intrauterine growth restriction is associated with a maturation delay of cardiac energetic microdomains. Frontiers in Cardiovascular Biology, European Society of Cardiology. London, UK. May 30 – April 1, 2012. Poster.

Am J Physiol Heart Circ Physiol 305: H1752–H1760, 2013.
First published October 4, 2013; doi:10.1152/ajpheart.00514.2013.

Intrauterine growth restriction is associated with cardiac ultrastructural and gene expression changes related to the energetic metabolism in a rabbit model

Anna Gonzalez-Tendero,[1] Iratxe Torre,[1,2] Patricia Garcia-Canadilla,[1,3] Fátima Crispi,[1,2,4] Francisco García-García,[5,6,7] Joaquin Dopazo,[5,6,7] Bart Bijnens,[3] and Eduard Gratacós[1,2,4]

[1]*Fetal and Perinatal Medicine Research Group, Institut d'Investigacions Biomèdiques August Pi i Sunyer, University of Barcelona, Barcelona, Spain;* [2]*Centro de Investigación Biomédica en Red de Enfermedades Raras, Hospital Clinic-University of Barcelona, Barcelona, Spain;* [3]*ICREA-PhySense, N-RAS, Universitat Pompeu Fabra, Barcelona, Spain;* [4]*Department of Maternal-Fetal Medicine, Institut Clínic de Ginecologia, Obstetrícia i Neonatologia, Barcelona, Spain;* [5]*Bioinformatics Department, Centro de Investigación Principe Felipe, Valencia, Spain;* [6]*Functional Genomics Node, INB, Centro de Investigación Principe Felipe, Valencia, Spain; and* [7]*Centro de Investigación Biomédica en Red de Enfermedades Raras, Centro de Investigación Principe Felipe, Valencia, Spain*

Submitted 3 July 2013; accepted in final form 28 September 2013

Gonzalez-Tendero A, Torre I, Garcia-Canadilla P, Crispi F, García-García F, Dopazo J, Bijnens B, Gratacós E. Intrauterine growth restriction is associated with cardiac ultrastructural and gene expression changes related to the energetic metabolism in a rabbit model. *Am J Physiol Heart Circ Physiol* 305: H1752–H1760, 2013. First published October 4, 2013; doi:10.1152/ajpheart.00514.2013.—Intrauterine growth restriction (IUGR) affects 7–10% of pregnancies and is associated with cardiovascular remodeling and dysfunction, which persists into adulthood. The underlying subcellular remodeling and cardiovascular programming events are still poorly documented. Cardiac muscle is central in the fetal adaptive mechanism to IUGR given its high energetic demands. The energetic homeostasis depends on the correct interaction of several molecular pathways and the adequate arrangement of intracellular energetic units (ICEUs), where mitochondria interact with the contractile machinery and the main cardiac ATPases to enable a quick and efficient energy transfer. We studied subcellular cardiac adaptations to IUGR in an experimental rabbit model. We evaluated the ultrastructure of ICEUs with transmission electron microscopy and observed an altered spatial arrangement in IUGR, with significant increases in cytosolic space between mitochondria and myofilaments. A global decrease of mitochondrial density was also observed. In addition, we conducted a global gene expression profile by advanced bioinformatics tools to assess the expression of genes involved in the cardiomyocyte energetic metabolism and identified four gene modules with a coordinated over-representation in IUGR: oxygen homeostasis (GO: 0032364), mitochondrial respiratory chain complex I (GO:0005747), oxidative phosphorylation (GO: 0006119), and NADH dehydrogenase activity (GO:0003954). These findings might contribute to changes in energetic homeostasis in IUGR. The potential persistence and role of these changes in long-term cardiovascular programming deserves further investigation.

cardiomyocyte intracellular organization; energetic metabolism; fetal cardiac programming; intracellular energetic units; intrauterine growth restriction

INTRAUTERINE GROWTH RESTRICTION (IUGR), due to placental insufficiency, affects up to 7–10% of pregnancies and is a major cause of perinatal mortality and long-term morbidity (1). Low birth weight, most likely due to IUGR, is strongly associated with increased risk of cardiovascular mortality in adulthood (7). This association is thought to be mediated through fetal cardiovascular programming. IUGR fetuses suffer from a chronic restriction of oxygen and nutrients (47), which triggers the initiation of a variety of adaptive structural (12, 14, 46, 51) and metabolic responses (25) due to a pressure/volume overload and, subsequently, with the objective of providing a more efficient myocardial performance. As a consequence, IUGR fetuses and newborns show signs of cardiovascular remodeling and altered function (21, 13, 14).

The effect of hypoxia and nutrient restriction during pregnancy in cardiac development and function has been previously studied, demonstrating the association of IUGR to a cardiac remodeling. Maternal hypoxia has been related to changes in cardiac structure and function (37, 38, 49), increased cardiac collagen content (50), and changes in cardiomyocyte proliferation and apoptosis (6, 28) and to long-term effects increasing cardiac susceptibility to ischemia-reperfusion injury by causing changes on myocardial energetic metabolism (39, 55). However, the underlying events of cardiac remodeling in IUGR at subcellular scale still remain poorly understood. The heart is an organ with high-energy requirements in the form of ATP to ensure proper functioning (29). Efficient energetic homeostasis depends on the correct arrangement of subcellular organelles. A close spatial interaction between mitochondria and the sarcomere contractile filaments is essential to ensure adequate and quick transportation of ATP. This is reached by the intracellular energetic units (ICEUs), which are structural and functional units, consisting of mitochondria located at the level of the sarcomeres between Z-lines interacting with surrounding myofilaments, sarcoplasmic reticulum, cytoskeleton, and cytoplasmic enzymes, that promote an endogenous cycling of adenine nucleotides between mitochondria and ATPases (40, 44, 45). Alterations in ICEUs arrangement together with an impaired local energetic regulation of the main cardiac ATPases have been described in cardiac pathophysiological processes (24). In addition, cardiomyocyte energetic homeostasis is regulated by a complex interaction of molecular pathways, mainly involving energy production through oxidative phosphorylation in the mitochondria (48). It has been widely described that disruption of mitochondrial oxidative phosphorylation plays a critical role in the development of heart failure (26, 35, 52). The oxidative phosphorylation takes place in the mitochondrial electron transport chain. It is composed of five complexes; in the complex I the enzyme NADH dehydrogenase catalyzes the reaction (2). Deficiencies in complex I

Address for reprint requests and other correspondence: E. Gratacós, Dept. of Maternal-Fetal Medicine, ICGON, Hospital Clinic. Sabino de Arana, 1 08028 Barcelona, Spain (e-mail: gratacos@clinic.ub.es).

function have been observed in dilated cardiomyopathy and in failing myocardium (41).

The goal of the present work was to evaluate the impact of chronic oxygen and nutrient restriction during a critical period for cardiac development, as present in IUGR, with regard to cardiomyocyte intracellular organization and gene expression of key pathways for energetic metabolism. For this purpose, the cardiomyocyte intracellular organization was studied by transmission electron microscopy. Additionally, the functional interpretation of the global gene expression profile was studied by means of advanced bioinformatics tools. The data presented here show changes in the cardiomyocyte intracellular organization in IUGR, specifically affecting ICEUs, together with an abnormal uprepresentation of blocks of genes acting together in a coordinated way, related to the cardiac oxygen homeostasis and energy production.

MATERIALS AND METHODS

Animal Model

New Zealand white rabbits were provided by a certified breeder. Dams were housed for 1 wk before surgery in separate cages on a reversed 12-h/12-h light cycle. Animals were fed a diet of standard rabbit chow and water ad libitum. Animal handling and all procedures were performed in accordance to applicable regulations and guidelines and with the approval of the Animal Experimental Ethics Committee of the University of Barcelona.

Six New Zealand white pregnant rabbits were used to reproduce a model of IUGR, following the method previously described (16, 17). At 25 days of gestation, selective ligature of uteroplacental vessels was performed as previously described (16, 17). Briefly, tocolysis (progesterone 0.9 mg/kg im) and antibiotic prophylaxis (Penicillin G 300.000 UI iv) were administered before surgery. Ketamine (35 mg/kg) and xylazine (5 mg/kg) were given intramuscularly for anesthesia induction. Inhaled anesthesia was maintained with a mixture of 1–5% isoflurane and 1–1.5 l/min oxygen. After a midline laparatomy, both uterine horns were exteriorized. The number of gestational sacs from each horn were counted and numbered. Pregnant rabbits have between 4 and 7 gestational sacs per horn. At random, one horn was assigned as the IUGR horn and the other horn was considered as the normal control growth. In all gestational sacs from the horn assigned as IUGR, a selective ligature of the 40–50% of the uteroplacental vessels was performed. No additional procedure was performed in the horn assigned as control. After the procedure, the abdomen was closed and animals received intramuscular meloxicam 0.4 $mg \cdot kg^{-1} \cdot 24\ h^{-1}$ for 48 h, as postoperative analgesia. Five days after surgery, at 30 days of gestation, a caesarean section was performed under the same anesthetic procedure and all living rabbit kits and their placentas were identified and weighted. Kits were anesthetized with an injection of ketamine and xylazine. After surgical removal from the chest cavity, hearts for gene expression analysis were immediately snap-frozen and stored at −80°C until the moment of use. Hearts for transmission electron microscopy imaging were processed as described in *Tissue processing*.

Electron Microscopy

Tissue processing. Hearts from 3 control and 3 IUGR rabbit fetuses, each control-IUGR pair coming from a different litter, were arrested in an ice-cold Ca^{2+}-free phosphate saline buffer immediately after surgical removal from the chest cavity. Random areas of left ventricle were dissected and cut into small pieces. Approximately 10 pieces from each left ventricle were incubated with 2% parafomaldehyde and 2.5% glutaraldehyde in phosphate buffer (PB) during 24 h at 4°C. Tissue pieces were then washed with PB and postfixed with 1% osmium tetroxide in PB containing 0.8% potassium ferricyanide at 4°C for 2 h. Next, samples were dehydrated in acetone, infiltrated with Epon resin during 2 days, embedded in the same resin, and polymerized at 60°C during 48 h. Semi-thin 500-nm sections were made to confirm the longitudinal orientation of cardiac sarcomeres under light microscope. Subsequently, 50-nm ultra-thin sections were cut using a Leica UC6 ultramicrotome (Leica Microsystems, Vienna, Austria) and mounted on Formvar-coated copper grids. Sections were stained with 2% uranyl acetate in water and lead citrate. Tissue sections were imaged using a JEM-1010 electron microscope (Jeol, Japan) equipped with a charge-coupled device camera Megaview III and the AnalySIS software (Soft Imaging System GmbH).

Morphological analysis. Morphological analysis of intracellular cardiomyocyte organization was performed in two randomly chosen left ventricle tissue pieces, from each subject. For each tissue piece, 50-nm ultra-thin sections were obtained from two ventricular areas separated 1 μm of distance. Images were taken at 20,000× magnification when an area containing longitudinal myofilaments surrounded by a mitochondrial network was observed. In this study, micrographs with disrupted mitochondria, disrupted sarcomeres or transversal or oblique orientation of sarcomeres were excluded from the quantification. Electron micrographs were taken and quantified in a blinded fashion and by one researcher (A. Gonzalez-Tendero). Images were analyzed from three viewpoints.

General cardiomyocyte cytoarchitecture: volume density estimation. The volume densities of myofilaments, mitochondria, and cytoplasm were estimated in 10 electron micrographs acquired from each heart. For this purpose, a grid in which each line intersection served as a sample point was generated on each image using ImageJ (36), according to standard stereological methods (20). Volume densities of the different structures were calculated by counting the number of points hitting the studied structures divided by the total number of points hitting the section, using a grid size of 0.02 a.u.

Mitochondria: area and number. The area of individual mitochondria was determined from 193 mitochondria in each study group. Individual mitochondria were delineated, and their area was measured using the AnalySIS software. The number of mitochondria was counted by using 10 randomly chosen images from each heart as previously described (22).

ICEUs arrangement. The cytoplasmic area and the mean distance between mitochondria and myofilaments within ICEUs were measured by delineating the area of cytoplasm existing between two consecutive z-disks and the immediately adjacent mitochondria, as shown in Fig. 1, using a custom-made GUI (Graphical User Interface) designed in MatLab (30). The area was automatically calculated, and the mean distance between mitochondria and myofilaments within

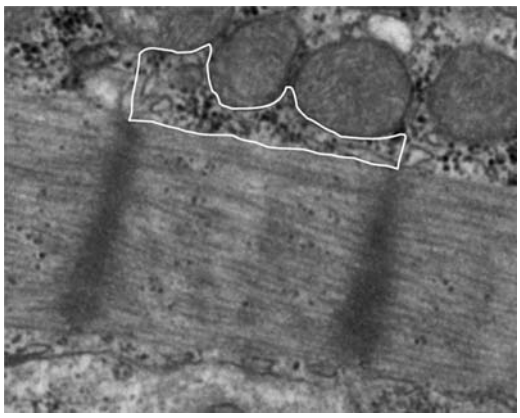

Fig. 1. Electron micrograph showing an example of the delineation used to automatically quantify the area of cytoplasm and the mean distance between mitochondria and myofilaments within intracellular energetic units (ICEUs).

ICEUs was obtained by evaluating the Euclidean distance of the delineated region (11). A total of 169 ICEUs were analyzed in the control group, whereas 154 ICEUs were analyzed in the IUGR group, obtained from 10 to 15 electron micrographs from each heart. We analyzed all the ICEUs found in the transmission electron microscopy images. However, ICEUs were discarded from the quantification when they were not clear or blurred or if the limits to mitochondria were not sharp enough.

Gene Set Expression Analysis

Gene expression microarray. The IUGR-gene expression profile was analyzed in 6 control and 6 IUGR rabbit fetuses, each control-IUGR pair coming from a different litter. In this study, special attention was paid to the expression profile of groups of genes related to energetic metabolism. Total RNA was isolated from 40 mg of each left ventricle. The extraction protocol was a combination of TRIzol as reagent and the RNeasy Mini kit (Qiagen). For each sample included in the study, the total amount of RNA was always above 25 μg with homogenous profile, showing an RNA integrity number between 9.3 to 9.9 (analyzed with RNA 6000 Nano and Bioanalyzer 2100; Agilent). Next, 500 ng of total RNA from each sample were labeled with the Quick Amp One-color Labelling kit (Agilent) and fluorochrome Cy3. Efficiency of labeling (Cy3pmol/μg) was analyzed using a Nanodrop spectrophotometer to check that values were above the minimum requirements (>1.65 μg and >9.0 pmols Cy3/μg). Additionally, a RNA 6000 Nano mRNA assay in the Bioanalyzer 2100 was done to assess that all the samples show a comparable profile and fragments size was as expected (200–2,000 bp). Then, 1,650 μg of RNA obtained from each labeled sample were hybridized during 17 h at 65°C with a Rabbit Microarray (Agilent Microarray Design ID 020908) containing 43,803 probe sequences obtained from the rabbit genome. All probe sequences included in the microarray were based on rabbit (*Oryctolagus cuniculus*) public transcript data. Finally, hybridization was quantified at 5 μm resolution (Axon 4000B scanner). Data extraction was done using Genepix Pro 6.0 software, and results were subjected to bioinformatics analysis.

Gene set analysis. Gene set analysis was carried out for the Gene Ontology (GO) terms using the FatiScan (3) algorithm, implemented in the Babelomics suite (4). This method detects significantly up- or downregulated blocks of functionally related genes in lists of genes ordered by differential expression. FatiScan can search for modules of genes that are functionally related by different criteria such as common annotations like GO terms.

The FatiScan algorithm studies the distribution of functional terms across the list of genes coming from the microarray experiment, extracting significantly under- and over-represented GO terms in a set of genes. GO terms were grouped in three categories: *1*) cellular components, that refer to the place in the cell where a gene product is active; *2*) biological processes, which refer to a biological objective to which a gene or gene product contributes; and *3*) molecular functions that represent all the biochemical activities of a gene product. FatiScan uses a Fisher's exact test for 2 × 2 contingency tables for comparing two groups of genes and extracting a list of GO terms whose distribution among the groups is significantly different. Given that many GO terms are simultaneously tested, the results of the test are corrected for multiple testing to obtain an adjusted *P* value. FatiScan returns adjusted *P* values based on the False Discovery Rate (FDR) method (10). GO annotation for the genes in the microarray were taken from the Blast2GO Functional Annotation Repository web page (http://bioinfo.cipf.es/b2gfar/). The raw microarray data have been deposited in the Gene Expression Omnibus database under accession number GSE37860.

Statistical Analysis

Statistical analysis of the morphological study was performed with the statistical package SPSS 18.0. Data are expressed as means ± SD or median (interquartile range, IQR). Statistical significance of differences between experimental groups was compared with an unpaired two-tailed *t*-test or Mann-Whitney test, depending whether variables followed a normal distribution. Differences were considered significant with probability values of $P < 0.05$. Statistical methods concerning gene expression analysis have been detailed in *Gene set analysis*.

RESULTS

Animal Model of IUGR: Fetal Biometry

Table 1 summarizes biometric outcome of the study groups. Birth weight, placental weigth, heart weight, crown-rump length, and abdominal girth decreased significantly in IUGR kits compared with normally growth kits. Additionally, heart-to-body weight ratio was increased in the IUGR group.

Morphological Analysis

General cardiomyocyte cytoarchitecture. Significant differences between IUGR and normally growth fetal myocardium could be observed regarding the arrangement of the intracellular components. A representative image of this is displayed in Fig. 2, *A* and *B*, showing that IUGR rabbits present a looser packing of mitochondria and an increased cytosolic space between mitochondria and myofilaments. Quantification of the volume densities of myofilaments, mitochondria, and cytoplasm is shown in Fig. 2*C*. Stereological examination of micrographs obtained from control and IUGR myocardium showed that the amount of myofilaments was not different between control and IUGR rabbits (mean 34.64 ± SD 4.04% in control vs. 34.74 ± 6.01% in IUGR; $P = 0.973$). On the other hand, changes in the relative volume occupied by mitochondria and cytoplasm were observed among control and IUGR myocardium. The relative volume occupied by mitochondria was significantly decreased in IUGR fetuses (34.59 ± 4.23% in control vs. 27.74 ± 5.28% in IUGR; $P = 0.032$), whereas the relative volume occupied by total cytoplasm was significantly increased under IUGR (30.77 ± 3.04% in control vs. 37.53 ± 4.97% in IUGR; $P = 0.018$). In this study we classified the cytoplasm into two categories according to its localization: *1*) cytoplasm located between mitochondria and myofilaments (ICEUs) and *2*) cytoplasm not located in the ICEUs, namely free cytoplasm. The cytoplasm existing within ICEUs was significantly increased under IUGR (6.47 ± 0.1.18% in control vs. 8.69 ± 1.75% in IUGR; $P = 0.027$). However, the free cytoplasm was not altered (24.31 ± 2.91% in control vs. 28.84 ± 5.27% in IUGR; $P = 0.095$).

Mitochondria: area and number. The average area of individual mitochondria as well as the number of mitochondria were quantified to test whether changes described in *General cardiomyocyte cyotarchitecture* could be due to changes in the mitochondrial size or number (Fig. 3). Results did not show statistically significant differences regarding the area of individual mitochondria

Table 1. *Biometry in experimental groups*

	Control	IUGR	*P* Value
Weight, g			
Birth	49.24 ± 8.03	29.76 ± 5.99	0.000*
Heart	0.43 ± 0.07	0.29 ± 0.07	0.001*
Heart/body, ×100	0.84 ± 0.12	1.02 ± 0.11	0.009*
Placenta	3.86 ± 1.06	2.23 ± 0.37	0.028*
Crown-rump length, mm	10.56 ± 0.46	8.94 ± 1.05	0.004*
Abdominal girth, mm	7.47 ± 0.93	6.38 ± 0.65	0.048*

Values are mean ± SD. IUGR, intrauterine growth restriction. *P value <0.05.

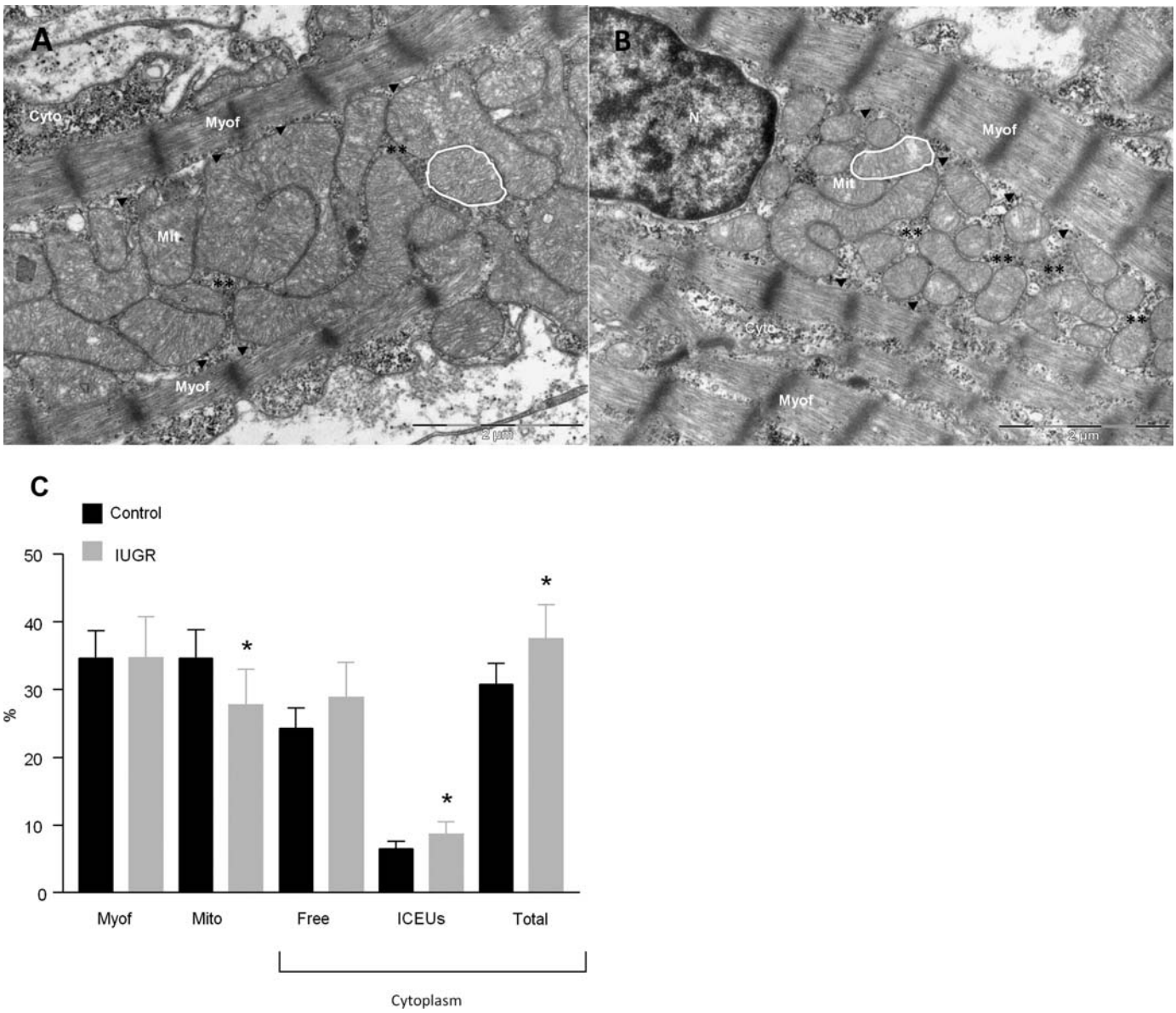

Fig. 2. Cytoarchitectural organization of cardiac myocytes. Representative micrographs show the typical organization of the intracellular space in control (*A*) and intrauterine growth restriction (IUGR; *B*) fetal cardiomyocytes. Although mitochondria are highly compacted and packed close to myofilaments in controls, they are looser packed, showing an increased cytosolic space both within the mitochondrial network (**) and between mitochondria and myofilaments (arrow heads) in IUGR. *C*: stereological measurements of fetal control and IUGR cardiomyocytes showing the relative volume occupied by myofilaments, mitochondria, free cytoplasm (Free), cytoplasm between mitochondria and myofilaments (ICEUs), and total cytoplasm (Total). *$P < 0.05$. Data in graphs are expressed as means ± SD. Magnification: 20,000×. Scale bar = 2 μm. Mit, mitochondria; Myof, myofilaments; Cyto, cytoplasm; N, nucleus.

(0.3094 ± 0.0595 μm^2 in control vs. 0.2407 ± 0.0176 μm^2 in IUGR; $P = 0.128$). Average number of mitochondria neither resulted to be different between control and IUGR hearts (27.47 ± 9.32 in control vs. 26.33 ± 8.06 in IUGR; $P = 0.627$).

ICEUs arrangement. The area and mean distance between mitochondria and myofilaments were automatically quantified (Fig. 4). Results showed that both the area of cytoplasm between mitochondria and myofilaments within ICEUs [median 120700 (IQR 87490–155500) nm^2 in control vs. 168600 (124100–236200) nm^2 in IUGR; $P = 0.015$; Fig. 4*E*] and the mean distance [105.7 (86.7–137.9) nm in control vs. 133.7 (104.7–182.3) nm in IUGR; $P = 0.037$; Fig. 4*F*] were significantly increased in IUGR rabbit myocardium.

Gene Set Expression Analysis

All experiments showed a good level of labeling and hybridization onto the Agilent microarray. Genes were ordered by differential expression between the two experimental conditions, and a ranked list with all genes of the experiment was obtained. We used the statistic of the statistical test for each gene, to order this list: genes at the top of list are more expressed in IUGR than in control group and genes at the bottom are more expressed in control than IUGR group. After analysis for a fold change higher than 0.5 and an adjusted *P* value lower than 0.05 (data not shown), there were not genes with significant differential expression. The output result of the

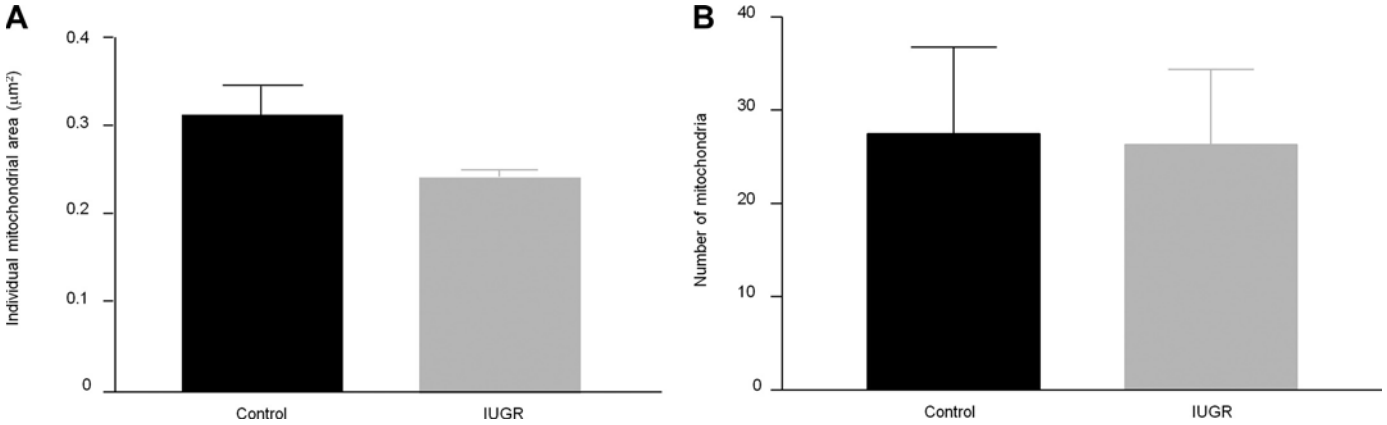

Fig. 3. Mitochondria area and number. *A*: average area of individual mitochondria, estimated delineating each mitochondria as shown in Fig. 2, *A* and *B*. *B*: average number of mitochondria. Data in graphs are expressed as means ± SD.

differential expression analysis (ranked list by the statistic of the test) was the input for the gene set analysis. On this full list of genes, Fatiscan detected groups of genes with the same expression pattern and sharing biological functions and extracted significantly under- and over-represented Gene Ontology terms in a set of genes after comparing two sub-lists of genes with different pattern of expression. The first list included genes more expressed in IUGR group, and the second, genes more expressed in the control group. Gene set analysis showed that IUGR subjects presented a statistically significant enrichment in groups of genes involved in energy production and cardiac energetic metabolism regulation (Table 2). Oxidative phosphorylation annotation (GO: 0006119, biological process) was found in 1.03% of the most upregulated genes in IUGR (list 1, more expressed in IUGR than control group), whereas only 0.17% of the most downregulated genes in IUGR contained the annotation (list 2, more expressed in control than IUGR group) (see Supplemental Material, Supplemental Table S. 1A). Similarly, the annotations for oxygen homeostasis (GO: 0032364, biological process) (Supplemental Table S. 1B), mitochondrial respiratory chain complex I (GO: 0005747, cellular component) (Supplemental Table S. 1C), and NADH dehydrogenase (GO: 0003954, molecular function) (Supplemental Table S. 1D) were found in 0.49%, 0.44%, and 0.35%, respectively, of the most upregulated genes in IUGR and only in 0.04%, 0%, and 0% of the most downregulated genes in IUGR, respectively. All P values were ≤ 0.001, and all adjusted P values were <0.08.

DISCUSSION

The study presented here shows an association between IUGR and a less organized intracellular arrangement of the cardiomyocyte organelles. The specific disarrangement of the ICEUs together with differences in the expression of key pathways for energy production suggest an impairment of the energetic metabolism under IUGR. This study can contribute to explain the process of fetal cardiac programming and the global contractile dysfunction previously described in IUGR fetuses and children (12, 13, 14).

The experimental IUGR model used in this study is based on the selective ligature of the uteroplacental vessels in pregnant rabbit at 25 days of gestation until 30 days of gestation. The model mimics IUGR in human pregnancy, since it induces a combined restriction of oxygen and nutrients, taking into account the role of the placenta (16, 17). Different gestational ages as well as different degrees of ligature severity were previously tested for this experimental IUGR model, with conclusions that the condition that best reproduced human IUGR due to placental insufficiency is the selective ligature of the 40–50% of the uteroplacental vessels at 25 days of gestation (16). It is known that in rabbits, complete organogenesis has been achieved at 19.5 days of gestation (9). The two previous statements together with the aim to reproduce late IUGR occurring in the third trimester of human pregnancy (which is mainly caused by placental and maternal vascular factors) lead to the rationale of the ligature from 25 to 30 days of gestation (16, 8). The severity of the experimental IUGR model reproducing human IUGR condition due to placental insufficiency, with regard to mortality rate and hemodynamic changes, has been previously described (16, 17). Cardiac function from IUGR kits is characterized by changes on cardiovascular Doppler parameters, with increased ductus venosus pulsatility index and increased isovolumetric relaxation time (17). Here we present the biometric changes induced by the selective ligature of 40–50% of the uteroplacental vessels, which result, as expected, in lower birth and heart weights, as well as decreased crown-rump length and abdominal girth. Additionally, an increase in heart to body weight is denoted in IUGR, which could be interpreted as a hypertrophic compensatory mechanism and is consistent with previous studies from experimental models of severe IUGR (28, 54, 55).

Our current analysis reports cardiomyocyte structural changes induced by IUGR. The stereological estimation of the volume densities of the different cellular components provides evidence that IUGR fetal hearts show a less organized intracellular arrangement, characterized by an increased relative volume occupied by cytoplasm and a decreased relative volume occupied by mitochondria. These changes under IUGR could be due to either alterations on cardiac development or hypoxia, or to mechanical stress caused by pressure or volume overload (49, 53). All the above mechanisms are believed to occur in and contribute to the development of cardiac dysfunction in IUGR, although the exact mechanisms are still not well understood. Recently it has been shown that experimentally induced pressure overload results in a depression of mitochondrial respiratory capacity together with a reduction of total

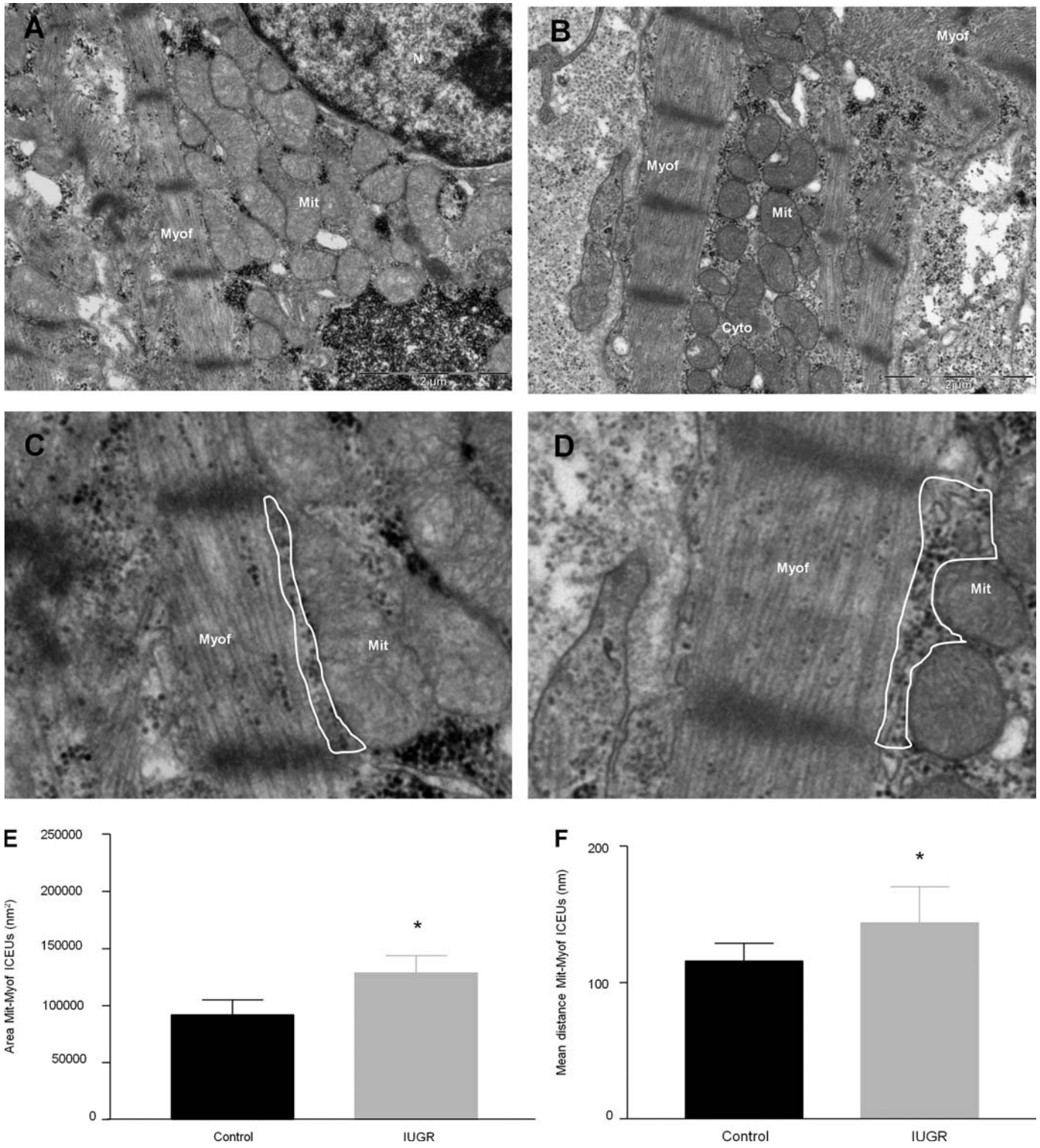

Fig. 4. Arrangement of ICEUs. Representative micrographs show an overview of a mitochondrial network surrounded by myofilaments in a control (*A*) and IUGR (*B*) fetal cardiomyocyte. *C* (control) and *D* (IUGR) are a detail of *A* and *B*, respectively, showing delineated ICEUs. Although in control myocardium mitochondria are closely apposed to myofilaments, the cytoplasmic space between mitochondria and myofilaments is greater in IUGR. *E* and *F*: quantification of the average area of cytoplasm and the mean distance between mitochondria and myofilaments within ICEUs, respectively. $*P < 0.05$. Data in graphs are expressed as means ± SD. Magnification: 20,000×. Scale bar = 2 μm. Mit, mitochondria; Myof, myofilaments; Cyto, cytoplasm; N, nucleus.

Table 2. *Gene set analysis with FatiScan*

Annotation	GO Annotation	Uprepresented in IUGR, %	Downrepresented in IUGR, %	*P* Value	Adjusted *P* Value	GO Type
Oxidative phosphorylation	0006119	1.03	0.17	1.15e-4	7.87e-2*	Biological process
Oxygen homeostasis	0032364	0.49	0.04	1.63e-4	7.82e-2*	Biological process
Mitochondrial respiratory chain complex I	0005747	0.44	0	1.39e-3	7.29e-2*	Cellular component
NADH dehydrogenase	0003954	0.35	0	4.37e-4	6.03e-2*	Molecular function

Gene Ontology (GO) annotations involved in energy production and cardiac energetic metabolism regulation with a statistically significant enrichment in IUGR. *Adjusted *P* value <0.08.

mitochondrial volume density, with a stronger effect on intermyofibrillar (IFM) compared with subsarcolemmal mitochondria (SSM) (42). Because our study samples are fetal, we cannot provide structural and functional differences between IFM and SSM (32). Despite that, our observations of a decrease on mitochondrial relative volume in IUGR are in line with the observations from Schwarzer et al. (42). The resulting structural remodeling shown in Fig. 4 from Schwarzer et al. (42) appears to be very similar to the structural remodeling presented in this study in IUGR hearts (Fig. 4). Additionally, in the same study (42), they relate a decrease in mitochondrial density with a decrease in mitochondrial size, since the citrate synthase activity is decreased in pressure overload but the mitochondrial number is not. We do not observe changes on the number or in the area of individual mitochondria. Since the stereological study shows a decreased relative volume occupied by mitochondria, we hypothesize that smaller mitochondrial size could be the reason for the decreased mitochondrial density (similar to what was described in pressure overloaded hearts) (42), despite the lack of significance, which might be attributed to sample size restrictions. The decrease in mitochondrial density but with no changes in myofibrillar content, as we show, has also been observed in fetal sheep subjected to high altitude hypoxia, which is in agreement with an alteration caused by the lack of oxygen during intrauterine life (27).

Concerning the relative volume occupied by cytoplasm, we observe that the total relative density of cytoplasm is increased in IUGR; however, when it is classified into free cytoplasm or cytoplasm within ICEUs, the former is not significantly increased, whereas the latter is increased in IUGR hearts. We show that both the area of cytoplasm and the mean distance between mitochondria and myofilaments within ICEUs are increased in IUGR myocardium. In fetal heart, energy transfer is believed to rely on the direct ATP and ADP channeling between organelles since the CK-bound (creatine kinase) system is not mature (23). Its efficiency mostly depends on the close interaction between mitochondria and myofilaments (24). In this regard, it has been reported that intracellular disorganization restricts ATP and ADP diffusion, decreasing the efficiency of energy transfer (5). Because ICEUs play a central role in maintaining cardiac energetic homeostasis, alterations on their structure could alter the energy production, utilization, and transfer, and as a consequence, cardiac function could be compromised (45). Based on previous studies, our data suggest that the abnormal arrangement of ICEUs could contribute to the development of less efficient hearts in IUGR, maybe due to a decrease on the energy transfer efficiency from mitochondria to the main cardiac ATPases. Such compromise of cardiac function due to alterations on ICEUs has been previously shown in heart failure (24). The abnormal arrangement of ICEUs in IUGR could also be interpreted as a maturation delay, since it has been described that during cardiac maturation there are major changes on the cardiomyocyte intracellular organization in which mitochondria get closer to myofilament to form the ICEUs (34).

Therefore, from one side our findings present a close similarity to the previously described in experimentally induced pressure overload cardiac dysfunction (18, 42). On the other side, it has been described that cytoarchitectural perturbations can lead to energetic alterations, and conversely perturbations of cellular energetic metabolism can lead to ultrastructural remodeling (52). In our study, it remains uncertain whether the structural changes could contribute to be a cause or a consequence of the cardiac dysfunction previously documented in IUGR.

Subsequently, we wanted to evaluate whether these structural changes are related to subtle changes on gene expression. For this purpose we performed a gene expression microarray experiment, which is complementary to the structural data and provides new evidence regarding the insults that IUGR hearts are receiving. We have used advanced bioinformatics analytic tools based on FatiScan gene set analysis (3), integrated in Babelomics (31). We propose the use of such procedure to scan ordered lists of genes and understand the biological processes operating behind them. Genes were ordered by differential expression between the two experimental conditions. There were not individual genes with significant differential expression. The output result of the differential expression analysis (ranked list by the statistic of the test) was the input for the gene set analysis. On this full list of genes, Fatiscan detected groups of genes with the same expression pattern and sharing biological functions. Therefore, the same analysis evaluated IUGR group and control group at the same time. Our analysis identified key gene pathways related to cardiac energy production, which were compromised under IUGR. This included oxygen homeostasis (GO: 0032364), oxidative phosphorylation (GO: 0006119), mitochondrial respiratory chain complex I (GO: 0005747), and NADH dehydrogenase activity (GO: 0003954). On one hand, alterations on the oxygen homeostasis and oxidative phosphorylation suggest that IUGR hearts are suffering from hypoxia. Previous studies have shown a 20–35% decrease in the oxidative phosphorylation in skeletal muscle from IUGR rats, leading to a decrease in ATP production and thus an impairment of skeletal muscle function (43). Additionally, exposure to chronic hypoxia has been related to a decrease in cardiac oxidative capacity in rats, which leads to a decline in ATP synthesis and in oxygen consumption (2). Hypoxia during early life has also been associated to persistent changes in genes linked to the regulation of cardiac metabolic processes that remain present long after the termina-

tion of the neonatal hypoxic insult (15). This may eventually be linked to the cardiovascular programming due to IUGR and the long-term persistence of the changes. On the other hand, alterations on the expression of mitochondrial respiratory chain complex I and specifically on the NADH dehydrogenase activity are again in line with the study of Schwarzer et al. (42) in pressure overload, in which they observe decreased function of the mitochondrial respiratory chain complex I. Our observations are also consistent with other studies in human IUGR in which a deficiency of the mitochondrial respiratory chain complex I has been observed (19).

Several study limitations and technical considerations should be mentioned. The morphological characterization of cardiomyocyte intracellular organization and ICEUs only provides structural information. Further studies are required to elucidate the functional consequences of these alterations. The bioinformatics gene set analysis used in this study is useful for studying diseases in which subtle differences are expected to occur, like in IUGR. Therefore, rather than expression changes on individual genes, alterations are expected to occur at the level of biological pathways and functionally related groups of genes. IUGR is thought to be a multifactorial disease in which several pathways and multiple members of a pathway might be involved, often resulting in only subclinical changes. However, we acknowledge that it is difficult to address the actual biological relevance of the gene expression findings. Future functional studies are required to relate the gene expression changes to the functional alterations at the cellular level. Finally, we do not evaluate the postnatal persistence in this study, which would provide valuable data of the long-term impact of the changes. However, this goal lies beyond the scope of the present study and should be investigated in future research.

In conclusion, we demonstrate that hearts from IUGR fetuses present a less organized intracellular arrangement of the cardiomyocyte organelles. These structural changes are accompanied with differences in the expression of groups of genes related to energy production and oxygen homeostasis. Overall, this study suggests that energetic metabolism is impaired in IUGR and provides new evidence to characterize cellular and subcellular mechanisms underlying cardiac remodeling in IUGR. Our findings might help to explain the global cardiac dysfunction previously documented in IUGR fetuses and children, and deserve further investigation to ascertain long-term persistence as part of the cardiovascular programming observed in IUGR.

ACKNOWLEDGMENTS

We thank Carmen López-Iglesias, head of the electron cryo-microscopy unit of CCiTUB (Centres Científics i Tecnològics de la Universitat de Barcelona), for support and advice with electron microscopy techniques.

GRANTS

This study was supported by grants from Ministerio de Economia y Competitividad PN de I+D+I 2008-2011 (ref. SAF2009_08815); Instituto de Salud Carlos III (ref. PI11/00051, PI11/01709) cofinanciado por el Fondo Europeo de Desarrollo Regional de la Unión Europea "Una manera de hacer Europa"; Centro para el Desarrollo Técnico Industrial (Ref. cvREMOD 2009-2012) apoyado por el Ministerio de Economia y Competitividad y Fondo de inversión local para el empleo, Spain; and AGAUR 2009 SGR Grant No. 1099. I. Torre was supported by a postdoctoral fellowship from Carlos III Institute of Health (Spain) (CD08/00176). P. Garcia-Canadilla acknowledges grant support to the Programa de Ayudas Predoctorales de Formación en Investigación en Salud del Instituto Carlos III, Spain (FI12/00362). A. Gonzalez-Tendero was supported by an IDIBAPS (Institut d'Investigacions Biomèdiques August Pi i Sunyer) predoctoral fellowship.

DISCLOSURES

No conflicts of interest, financial or otherwise, are declared by the author(s).

AUTHOR CONTRIBUTIONS

Author contributions: A.G.-T., I.T., F.C., and E.G. conception and design of research; A.G.-T., I.T., F.G.-G., and J.D. performed experiments; A.G.-T., I.T., P.G.-C., F.G.-G., and J.D. analyzed data; A.G.-T., I.T., F.C., B.B., and E.G. interpreted results of experiments; A.G.-T. prepared figures; A.G.-T. drafted manuscript; A.G.-T., I.T., F.C., B.B., and E.G. edited and revised manuscript; all authors approved final version of manuscript.

REFERENCES

1. **Alberry M, Soothill P.** Management of fetal growth restriction. *Arch Dis Child Fetal Neonatal Ed* 92: F62–F67, 2007.
2. **Al Ghouleh I, Khoo NK, Knaus UG, Griendling KK, Touyz RM, Thannickal VJ, Barchowsky A, Nauseef WM, Kelley EE, Bauer PM, Darley-Usmar V, Shiva S, Cifuentes-Pagano E, Freeman BA, Gladwin MT, Pagano PJ.** Oxidases and peroxidases in cardiovascular and lung disease: new concepts in reactive oxygen species signaling. *Free Radic Biol Med* 51: 1271–1288, 2011.
3. **Al-Shahrour F, Arbiza L, Dopazo H, Huerta-Cepas J, Mínguez P, Montaner D, Dopazo J.** From genes to functional classes in the study of biological systems. *BMC Bioinformatics* 8: 114, 2007.
4. **Al-Shahrour F, Carbonell J, Minguez P, Goetz S, Conesa A, Tárraga J, Medina I, Alloza E, Montaner D, Dopazo J.** Babelomics: advanced functional profiling of transcriptomics, proteomics and genomics experiments. *Nucleic Acids Res* 36: W341–W346, 2008.
5. **Anmann T, Guzun R, Beraud N, Pelloux S, Kuznetsov AV, Kogerman L, Kaambre T, Sikk P, Paju K, Peet N, Seppet E, Ojeda C, Tourneur Y, Saks V.** Different kinetics of the regulation of respiration in permeabilized cardiomyocytes and in HL-1 cardiac cells. Importance of cell structure/organization for respiration regulation. *Biochim Biophys Acta* 1757: 1597–1606, 2006.
6. **Bae S, Xiao Y, Li G, Casiano CA, Zhang L.** Effect of maternal chronic hypoxic exposure during gestation on apoptosis in fetal rat heart. *Am J Physiol Heart Circ Physiol* 285: H983–H990, 2003.
7. **Barker DJ.** Fetal origins of cardiovascular disease. *Ann Med* 1: 3–6, 1999.
8. **Bassan H, Trejo LL, Kariv N, Bassan M, Berger E, Fattal A, Gozes I, Harel S.** Experimental intrauterine growth retardation alters renal development. *Pediatr Nephrol* 15: 192–195, 2000.
9. **Beaudoin S, Barbet P, Bargy F.** Developmental stages in the rabbit embryo: guidelines to choose an appropriate experimental model. *Fetal Diagn Ther* 18: 422–427, 2003.
10. **Benjamini Y, Hochberg Y.** Controlling the false discovery rate a practical and powerful approach to multiple testing. *J R Statist Soc B* 57: 289–300, 1995.
11. **Breu H, Gil J, David Kirkpatrick D, Werman M.** Linear time Euclidean distance transform algorithms. *IEEE Trans Pattern Anal Mach Intell* 5: 529–533, 1995.
12. **Comas M, Crispi F, Cruz-Martinez R, Martinez JM, Figueras F, Gratacos E.** Usefulness of myocardial tissue Doppler vs. conventional echocardiography in the evaluation of cardiac dysfunction in early-onset intrauterine growth restriction. *Am J Obstet Gynecol* 203: e1–e7, 2010.
13. **Crispi F, Bijnens B, Figueras F, Bartrons J, Eixarch E, Le Noble F, Ahmed A, Gratacós E.** Fetal growth restriction results in remodeled and less efficient hearts in children. *Circulation* 121: 2427–2436, 2010.
14. **Crispi F, Hernandez-Andrade E, Pelsers MM, Plasencia W, Benavides-Serralde JA, Eixarch E, Le Noble F, Ahmed A, Glatz JF, Nicolaides KH, Gratacos E.** Cardiac dysfunction and cell damage across clinical stages of severity in growth-restricted fetuses. *Am J Obstet Gynecol* 199: e1–e8, 2008.
15. **Del Duca D, Tadevosyan A, Karbassi F, Akhavein F, Vaniotis G, Rodaros D, Villeneuve LR, Allen BG, Nattel S, Rohlicek CV, Hébert TE.** Hypoxia in early life is associated with lasting changes in left ventricular structure and function at maturity in the rat. *Int J Cardiol* 156: 165–173, 2012.
16. **Eixarch E, Figueras F, Hernández-Andrade E, Crispi F, Nadal A, Torre I, Oliveira S, Gratacós E.** An experimental model of fetal growth restriction based on selective ligature of uteroplacental vessels in the pregnant rabbit. *Fetal Diagn Ther* 26: 203–211, 2009.
17. **Eixarch E, Hernandez-Andrade E, Crispi F, Illa M, Torre I, Figueras F, Gratacos E.** Impact on fetal mortality and cardiovascular Doppler of

selective ligature of uteroplacental vessels compared with undernutrition in a rabbit model of intrauterine growth restriction. *Placenta* 32: 304–309, 2011.
18. **Friehs I, Cowan DB, Choi YH, Black KM, Barnett R, Bhasin MK, Daly C, Dillon SJ, Libermann TA, McGowan FX, del Nido PJ, Levitsky S, McCully JD.** Pressure-overload hypertrophy of the developing heart reveals activation of divergent gene and protein pathways in the left and right ventricular myocardium. *Am J Physiol Heart Circ Physiol* 304: H697–H708, 2013.
19. **Gibson K, Halliday JL, Kirby DM, Yaplito-Lee J, Thorburn DR, Boneh A.** Mitochondrial oxidative phosphorylation disorders presenting in neonates: clinical manifestations and enzymatic and molecular diagnoses. *Pediatrics* 122: 1003–1008, 2008.
20. **Gundersen HJ, Bendtsen TF, Korbo L, Marcussen N, Møller A, Nielsen K, Nyengaard JR, Pakkenberg B, Sørensen FB, Vesterby A, West MJ.** Some new, simple and efficient stereological methods and their use in pathological research and diagnosis. *APMIS* 96: 379–394, 1988.
21. **Hecher K, Snijders R, Campbell S, Nicolaides K.** Fetal venous, intracardiac, and arterial blood flow measurements in intrauterine growth retardation: relationship with fetal blood gases. *Am J Obstet Gynecol* 173: 10–15, 1995.
22. **Hiraumi Y, Iwai-Kanai E, Baba S, Yui Y, Kamitsuji Y, Mizushima Y, Matsubara H, Watanabe M, Watanabe K, Toyokuni S, Matsubara H, Nakahata T, Adachi S.** Granulocyte colony-stimulating factor protects cardiac mitochondria in the early phase of cardiac injury. *Am J Physiol* 29: 823–832, 2009.
23. **Hoerter JA, Kuznetsov A, Ventura-Clapier R.** Functional development of the creatine kinase system in perinatal rabbit heart. *Circ Res* 69: 665–676, 1991.
24. **Joubert F, Wilding JR, Fortin D, Domergue-Dupont V, Novotova M, Ventura-Clapier R, Veksler V.** Local energetic regulation of sarcoplasmic and myosin ATPase is differently impaired in rats with heart failure. *J Physiol* 586: 5181–5192, 2008.
25. **Kanaka-Gantenbein C.** Fetal origins of adult diabetes. *Ann N Y Acad Sci* 1205: 99–105, 2010.
26. **Lemieux H, Semsroth S, Antretter H, Höfer D, Gnaiger E.** Mitochondrial respiratory control and early defects of oxidative phosphorylation in the failing human heart. *Int J Biochem Cell Biol* 43: 1729–1738, 2011.
27. **Lewis AM, Mathieu-Costello O, McMillan PJ, Gilbert RD.** Quantitative electron microscopic study of the hypoxic fetal sheep heart. *Anat Rec* 256: 381–388, 1999.
28. **Lim K, Zimanyi MA, Black MJ.** Effect of maternal protein restriction during pregnancy and lactation on the number of cardiomyocytes in the postproliferative weanling rat heart. *Anat Rec (Hoboken)* 293: 431–437, 2010.
29. **Lopaschuk GD, Jaswal JS.** Energy metabolic phenotype of the cardiomyocyte during development, differentiation, and postnatal maturation. *J Cardiovasc Pharmacol* 56: 130–140, 2010.
30. **The Mathworks Inc.** Mathworks 2007b, version 7.5.0.342. MATLAB. Massachusetts: The MathWorks Inc.
31. **Medina I, Carbonell J, Pulido L, Madeira SC, Goetz S, Conesa A, Tárraga J, Pascual-Montano A, Nogales-Cadenas R, Santoyo J, García F, Marbà M, Montaner D, Dopazo J.** Babelomics: an integrative platform for the analysis of transcriptomics, proteomics and genomic data with advanced functional profiling. *Nucleic Acids Res* 38: W210–W213, 2010.
32. **Nassar R, Reedy MC, Anderson PA.** Developmental changes in the ultrastructure and sarcomere shortening of the isolated rabbit ventricular myocyte. *Circ Res* 61: 465–483, 1987.
33. **Nouette-Gaulain K, Malgat M, Rocher C, Savineau JP, Marthan R, Mazat JP, Sztark F.** Time course of differential mitochondrial energy metabolism adaptation to chronic hypoxia in right and left ventricles. *Cardiovasc Res* 66: 132–140, 2005.
34. **Piquereau J, Novotova M, Fortin D, Garnier A, Ventura-Clapier R, Veksler V, Joubert F.** Postnatal development of mouse heart: formation of energetic microdomains. *J Physiol* 588: 2443–2454, 2010.
35. **Porter GA, Hom J, Hoffman D, Quintanilla R, de Mesy Bentley K, Sheu SS.** Bioenergetics, mitochondria, and cardiac myocyte differentiation. *Prog Pediatr Cardiol* 31: 75–81, 2011.
36. **Rasband WS.** ImageJ. National Institutes of Health, Bethesda, Maryland, USA, http://imagej.nih.gov/ij/, 1997–2011.
37. **Ream M, Ray AM, Chandra R, Chikaraishi DM.** Early fetal hypoxia leads to growth restriction and myocardial thinning. *Am J Physiol Regul Integr Comp Physiol* 295: R583–R595, 2008.
38. **Rueda-Clausen CF, Morton JS, Davidge ST.** Effects of hypoxia-induced intrauterine growth restriction on cardiopulmonary structure and function during adulthood. *Cardiovasc Res* 81: 713–722, 2009.
39. **Rueda-Clausen CF, Morton JS, Lopaschuk GD, Davidge ST.** Long-term effects of intrauterine growth restriction on cardiac metabolism and susceptibility to ischaemia/reperfusion. *Cardiovasc Res* 90: 285–294, 2011.
40. **Saks V, Kuznetsov AV, Gonzalez-Granillo M, Tepp K, Timohhina N, Karu-Varikmaa M, Kaambre T, Dos Santos P, Boucher F, Guzun R.** Intracellular energetic units regulate metabolism in cardiac cells. *J Mol Cell Cardiol* 52: 419–436, 2012.
41. **Scheubel RJ, Tostlebe M, Simm A, Rohrbach S, Prondzinsky R, Gellerich FN, Silber RE, Holtz J.** Dysfunction of mitochondrial respiratory chain complex I in human failing myocardium is not due to disturbed mitochondrial gene expression. *J Am Coll Cardiol* 40: 2174–2181, 2002.
42. **Schwarzer M, Schrepper A, Amorim PA, Doenst T.** Pressure overload differentially affects respiratory capacity in interfibrillar and subsarcolemmal mitochondria. *Am J Physiol Heart Circ Physiol* 304: H529–H537, 2013.
43. **Selak MA, Storey BT, Peterside I, Simmons RA.** Impaired oxidative phosphorylation in skeletal muscle of intrauterine growth-retarded rats. *Am J Physiol Endocrinol Metab* 285: E130–E137, 2003.
44. **Seppet EK, Eimre M, Anmann T, Seppet E, Peet N, Käämbre T, Paju K, Piirsoo A, Kuznetsov AV, Vendelin M, Gellerich FN, Zierz S, Saks VA.** Intracellular energetic units in healthy and diseased hearts. *Exp Clin Cardiol* 10: 173–183, 2005.
45. **Seppet EK, Eimre M, Anmann T, Seppet E, Piirsoo A, Peet N, Paju K, Guzun R, Beraud N, Pelloux S, Tourneur Y, Kuznetsov AV, Käämbre T, Sikk P, Saks VA.** Structure-function relationships in the regulation of energy transfer between mitochondria and ATPases in cardiac cells. *Exp Clin Cardiol* 11: 189–194, 2006.
46. **Skilton MK, Evans N, Griffiths KA, Harmer JA, Celermajer D.** Aortic wall thickness in newborns with intrauterine growth restriction. *Lancet* 23: 1484–1486, 2005.
47. **Soothill PW, Nicolaides KH, Campbell S.** Prenatal asphyxia, hyperlacticaemia, hypoglycaemia, and erythroblastosis in growth retarded fetuses. *BMJ* 294: 1051–1053, 1987.
48. **Stanley WC, Recchia FA, Lopaschuk GD.** Myocardial substrate metabolism in the normal and failing heart. *Physiol Rev* 85: 1093–1129, 2005.
49. **Tintu A, Rouwet E, Verlohren S, Brinkmann J, Ahmad S, Crispi F, van Bilsen M, Carmeliet P, Staff AC, Tjwa M, Cetin I, Gratacos E, Hernandez-Andrade E, Hofstra L, Jacobs M, Lamers WH, Morano I, Safak E, Ahmed A, le Noble F.** Hypoxia induces dilated cardiomyopathy in the chick embryo: mechanism, intervention, and long-term consequences. *PLos One* 4: e5155, 2009.
50. **Tong W, Xue Q, Li Y, Zhang L.** Maternal hypoxia alters matrix metalloproteinase expression patterns and causes cardiac remodeling in fetal and neonatal rats. *Am J Physiol Heart Circ Physiol* 301: H2113–H2121, 2011.
51. **Turan S, Turan OM, Salim M, Berg C, Gembruch U, Harman CR, Baschat AA.** Cardiovascular transition to extrauterine life in growth-restricted neonates: relationship with prenatal Doppler findings. *Fetal Diagn Ther* 33: 103–109, 2013.
52. **Ventura-Clapier R, Garnier A, Veksler V, Joubert F.** Bioenergetics of the failing heart. *Biochim Biophys Acta* 1813: 1360–1372, 2011.
53. **Verburg BO, Jaddoe VW, Wladimiroff JW, Hofman A, Witteman JC, Steegers EA.** Fetal hemodynamic adaptive changes related to intrauterine growth: the Generation R Study. *Circulation* 117: 649–659, 2008.
54. **Wang KC, Zhang L, McMillen IC, Botting KJ, Duffield JA, Zhang S, Suter CM, Brooks DA, Morrison JL.** Fetal growth restriction and the programming of heart growth and cardiac insulin-like growth factor 2 expression in the lamb. *J Physiol* 589: 4709–4722, 2011.
55. **Xu Y, Williams SJ, O'Brien D, Davidge ST.** Hypoxia or nutrient restriction during pregnancy in rats leads to progressive cardiac remodeling and impairs postischemic recovery in adult male offspring. *FASEB J* 20: 1251–1253, 2006.

5.3. STUDY 3

Cardiac dysfunction is associated with altered sarcomere ultrastructure in intrauterine growth restriction

Iruretagoyena JI, Gonzalez-Tendero A, Garcia-Canadilla P, Amat-Roldan I, Torre I, Nadal A, Crispi F, Gratacos E. Am J Obstet Gynecol. 2014. doi: 10.1016/j.ajog.2014.01.023.

Status: Published.

Journal Impact Factor: 3.877

Quartile: 1st

Results from this study have been presented in

1. Iruretagoyena I, Torre I, Amat-Roldan I, Psilodimitrakopoulos S, Crispi F, Garcia-Canadilla P, Gonzalez-Tendero A, Nada A, Eixarch E, Loza-Alvarez P, Artigas D, Gratacos E. Ultrastructural analysis of myocardiocyte sarcomeric changes in relation with cardiac dysfunction in human fetuses with intrauterine growth restriction. 31th Annual Meeting.The Pregnancy Meeting· Society for Maternal-Fetal medicine. San Francisco, USA. February 2011. Oral communication.

BASIC SCIENCE: OBSTETRICS

Cardiac dysfunction is associated with altered sarcomere ultrastructure in intrauterine growth restriction

Jesus Igor Iruretagoyena, MD; Anna Gonzalez-Tendero, MSc; Patricia Garcia-Canadilla, MSc; Ivan Amat-Roldan, PhD; Iratxe Torre, PhD; Alfons Nadal, MD; Fatima Crispi, MD; Eduard Gratacos, MD

OBJECTIVE: The purpose of this study was to assess whether abnormal cardiac function in human fetuses with intrauterine growth restriction (IUGR) is associated with ultrastructural differences in the cardiomyocyte sarcomere.

STUDY DESIGN: Nine severe early-onset IUGR fetuses and 9 normally grown fetuses (appropriate growth for gestational age) who died in the perinatal period were included prospectively. Cardiac function was assessed by echocardiography and levels of B-type natriuretic peptide and troponin-I. Heart sections were imaged by second harmonic generation microscopy, which allowed unstained visualization of cardiomyocyte's sarcomere length.

RESULTS: Echocardiographic and biochemical markers showed signs of severe cardiac dysfunction in IUGR fetuses. Second harmonic generation microscopy demonstrated a significantly shorter sarcomere length in IUGR as compared with appropriate growth for gestational age fetuses.

CONCLUSION: IUGR is associated with changes in the cardiomyocyte contractile machinery in the form of shorter sarcomere length, which could help to explain the cardiac dysfunction previously documented in IUGR.

Key words: cardiac function, cardiomyocyte, intrauterine growth restriction, sarcomere, second harmonic generation microscopy

Cite this article as: Iruretagoyena JI, Gonzalez-Tendero A, Garcia-Canadilla P, et al. Cardiac dysfunction is associated with altered sarcomere ultrastructure in intrauterine growth restriction. Am J Obstet Gynecol 2014;210:●●●●.

Intrauterine growth restriction (IUGR) affects 7-10% of all pregnancies and constitutes an important cause of perinatal death and long-term morbidity.[1-3] Epidemiologic evidence has long suggested a link between low birthweight and increased cardiovascular death in adulthood.[4] Recent studies have demonstrated that IUGR fetuses present cardiovascular dysfunction in utero[5-8] that persists postnatally in the form of cardiovascular dysfunction and remodelling.[9,10] However, the molecular mechanisms underlying the relationship between IUGR and increased risk of cardiovascular disease are understood poorly.[11]

The basic unit of cardiomyocyte's contractile machinery is the sarcomere. Disruption of normal sarcomere structure is involved in cardiac dysfunction and remodeling in a substantial number of cardiac conditions such as inherited cardiomyopathies,[12,13] anthracyclines cardiotoxicity,[14] and heart failure.[15] Second harmonic generation microscopy (SHGM) is a recent technique that is based on a nonlinear optical effect known as second harmonic generation. SHGM is used widely in biomedical research as an imaging technique that allows the measurement of morphologic features at subcellular level, including sarcomere length and pattern[16,17] by identification of the myosin of thick filaments of sarcomere.[18,19] Recently, our group has validated an automated method to better quantify sarcomere length in the fetal heart.[20]

From the Fetal and Perinatal Medicine Research Group, Institut d'Investigacions Biomèdiques August Pi i Sunyer (IDIBAPS) (Drs Iruretagoyena, Amat-Roldan, Torre, Crispi, and Gratacos, Ms Gonzalez-Tendero, and Ms Garcia-Canadilla); Departments of Maternal-Fetal Medicine (Drs Iruretagoyena, Crispi, and Gratacos) and Pathology (Dr Nadal), Hospital Clinic, Universitat de Barcelona; Physense, Departament de Tecnologies de la Informació i les Comunicacions (DTIC), Universitat Pompeu Fabra (Ms Garcia-Canadilla); and Centro de Investigación Biomédica en Red de Enfermedades Raras (CIBERER) (Drs Crispi and Gratacos), Barcelona, Spain.

Received Aug. 21, 2013; revised Nov. 27, 2013; accepted Jan. 15, 2014.

Supported in part by grants from Instituto de Salud Carlos III and Ministerio de Economia y Competitividad (FIS-PI11/01709, FIS PI11/00051, PI12/00801, and SAF2012-37196) cofinanciado por el Fondo Europeo de Desarrollo Regional de la Unión Europea "Una manera de hacer Europa" and Cerebra Foundation for the Brain Injured Child (Carmarthen, Wales, UK); the Programa de Ayudas Predoctorales de Formación en investigación en Salud (FI12/00362) from the Instituto Carlos III, Spain (P.G.C.); an IDIBAPS (Institut d'Investigacions Biomèdiques August Pi i Sunyer) predoctoral fellowship (A.G.T.); and the Programa de Ayudas Postdoctorales Sara Borrell (CD08/00176) from the Instituto de Salud Carlos III, Spain (I.T.).

The authors report no conflict of interest.

Presented at the 31st annual meeting of the Society for Maternal-Fetal Medicine, San Francisco, CA, Feb. 6-11, 2011.

Reprints: Eduard Gratacos, Department of Maternal-Fetal Medicine (ICGON), Hospital Clinic, Sabino de Arana 1, 08028, Barcelona, Spain. gratacos@clinic.ub.es.

0002-9378/$36.00 • • http://dx.doi.org/10.1016/j.ajog.2014.01.023

We hypothesized that cardiac dysfunction in IUGR could be associated with disruption of normal sarcomere structure. Within a large prospective research program to characterize cardiac function in IUGR,[9] we conducted a nested case-control study. Cardiac tissue was retrieved from 9 IUGR fetuses who died around delivery and from 9 appropriate growth for gestational age (AGA) fetuses who were selected from patients who underwent termination of pregnancy. Cardiac tissue was analyzed by means of SHGM, and sarcomere length was assessed in cases and control subjects.

Materials and Methods

Study groups

The study population included 9 severe early-onset IUGR and 9 AGA fetuses from 19-33 weeks of gestation who died in the perinatal period because of perinatal complications or medical termination of pregnancy. Cases were singleton pregnancies with IUGR that had been included in a large prospective cohort that evaluated cardiac dysfunction in IUGR.[9] AGA fetuses were selected among women who underwent termination of pregnancy because of severe maternal disease or noncardiac malformations. Intracardiac injection of potassium chloride was performed electively to induce cardiac arrest before induction of labor according to local standard protocols in those cases that undergo termination of pregnancy after 22 weeks.

The study protocol was approved by the Ethics Committee at the participating institution, and all patients provided written informed consent. Exclusion criteria were chromosomal anomalies or evidence of fetal infection. In all pregnancies, gestational age was calculated based on the crown-rump length at the first-trimester ultrasound examination. *IUGR* was defined as an estimated fetal weight at <10th percentile according to local reference curves[21] together with umbilical artery (UA) pulsatility index (PI) at >2 standard deviations.[22]

Fetal ultrasound assessment

All cases underwent ultrasonographic examination of fetal well-being and hemodynamics within 48 hours of delivery or fetal death, including complete morphologic examination, fetal weight, UA, middle cerebral artery, and cerebroplacental ratio. Ultrasound assessment was performed with a Siemens Sonoline Antares (Siemens Medical Systems, Erlangen, Germany) or a Voluson 730 Expert (GE Medical Systems, Milwaukee, WI) with 6-4 or 6-2 MHz curved array probes. All Doppler estimations were done in the absence of fetal body movements and, if required, with maternal voluntary suspended respiration. The angle of insonation was kept at <30°, and the wall filter was set to 70 Hz to avoid sound artifacts. The mechanical and thermal indices were maintained at <1. UA PI was obtained from a free loop of the umbilical cord. Middle cerebral artery PI was measured in a transverse view of the fetal skull at the level of its origin from the Circle of Willis. Cerebroplacental ratio was calculated as middle cerebral artery P/UA PI.[21] All individual Doppler data were normalized by conversion of the measurements into z-scores (standard deviation from the gestational age mean).[22]

Fetal echocardiography

Echocardiographic measurements performed within 48 hours of delivery or fetal death included ductus venosus PI, left myocardial performance index (MPI), and diastolic ventricular filling ratios. Ductus venosus PI was obtained from a mid-sagittal or alternatively transverse section of the fetal abdomen.[23] Left MPI was obtained in a cross-sectional image of the fetal thorax and an apical 4-chamber view, placing the Doppler sample volume on the medial wall of the ascending aorta including the aortic and mitral valve. The movements (clicks) of the valves in the Doppler trim were used as landmarks to calculate the isovolumetric contraction and relaxation time, and the ejection time. MPI was calculated as (isovolumetric contraction + relaxation time)/ejection time.[24-27] Mitral and tricuspid diastolic ventricular filling ratios were obtained in an apical 4-chamber view, with the Doppler sample volume just below the atrioventricular valves, and were calculated by division of early diastolic by atrial peak inflow velocities.[25] Echocardiographic parameters were normalized into z-scores.[23-25]

Cardiovascular markers in fetal blood

Fetal umbilical ethylenediaminetetraacetic acid–treated blood was obtained from the umbilical vein after cord clamp at delivery in cases or at cardiocentesis in fetuses who underwent termination of pregnancy. All samples were processed within 1 hour. Plasma was separated by centrifugation at 1400*g* for 10 minutes at 4°C; samples were stored immediately at −80°C until assay. Cord blood levels of B-type natriuretic peptide (BNP) were measured with an immunoassay system (ADVIA Centaur BNP; Siemens Healthcare Diagnostics, Deerfield, IL), as described previously.[28] Troponin-I levels were measured with commercially available assays from Centaur CP–troponin-I assay (Siemens Healthcare Diagnostics).

Heart tissue collection

Heart samples were collected at autopsy. A transverse section of the upper third of posterior left ventricular wall was obtained and then fixed in 3.7% paraformaldehyde, dehydrated, and embedded in paraffin. Subsequently, 30-μm–thick sections were cut from the paraffin blocks for microscopic examination with a Leica microtome (Leica RM 2135; Leica Microsystems Heidelberg GmbH, Manheim, Germany). Finally, sections were mounted onto Silane- (Sigma-Aldrich, St. Louis, MO) coated thin slides. Tissue sections were deparaffined with xylene, hydrated with decreasing concentrations of ethanol (100°/96°/70°), and finally covered with Mowiol 4-88 mounting medium (Sigma-Aldrich). All samples were processed and imaged by the same person (A.G.-T.).

SHGM of heart tissue

Detection of SHGM was performed with a Leica TCS-SP5 laser scanning spectral confocal multiphoton microscope (Leica Microsystems Heidelberg GmbH) equipped with a Near Infrared laser (Mai Tai Broad Band 710-990 nm, 120 femptosecond pulse) and DMI6000

inverted microscope (Advanced Optical Microscopy Unit from Scientific and Technological Centres from University of Barcelona). Second Harmonic images were acquired from 30-μm−thick unstained tissue sections with a ×25 water immersion objective (numeric aperture 0.95) and an oil immersion condenser (NA 1.40 OilS1). Acquisition features were 400 Hz of scan speed, 810 nm excitation light, and emission collected through a 405-nm filter with transmitted light photomultiplier tube, 16-bit depth, and a resolution of 40 nm/pixel. Between 4 and 10 different areas were imaged for each tissue section. For image acquisition, cardiac longitudinal myofibers were oriented at 45 degrees to maximize signal to noise ratio of SHGM from muscle fibers. The distinctive biperiod pattern of sarcomeres[29] was obtained and characterized by 2 distances: intrasarcomeric distance of A-bands (A-A band) and the sarcomere length, which was measured as the distance between Z-lines (Z-Z line). Measurements of both distances were performed automatically by a custom algorithm that was based on the analysis of the autocorrelation of the SHGM intensity profile in a myofiber, as previously reported[20] (Figure 1). Briefly, the local myofiber orientation was estimated, and the tracking of all the myofibers in the image was performed automatically. After that, the SHGM intensity profile was obtained for each myofiber in the image (Figure 1, B and C). Then, the autocorrelation of the intensity profile was calculated and fitted with a parametric model to compute the A-A band and Z-Z line mean distances of all the sarcomeres that formed the myofiber. This procedure was repeated for all the myofibers. Finally, the distances that had been measured in all the myofibers were averaged to obtain the mean A-A band and Z-Z line distances in the image.

Statistical analysis

Results are expressed as median ± interquartile range. Comparisons between IUGR and AGA were performed by the chi-square test, the Student *t* test, and the Mann-Whitney *U* analysis. To compute the differences in the sarcomeric distances between IUGR and AGA, 4 areas of each individual image were selected randomly and considered for statistical analysis by the Student *t* test, because 4 was the minimum number of analyzed areas in 1 individual. This procedure was repeated 30 times, and the mean probability value ($\hat{p}$) was calculated as

$$\hat{p} = 10^{\wedge}\left(\frac{1}{30}\sum_{i=1}^{30}\log[p(i)]\right)$$

where p was the probability value of the *t* test. Differences were considered significant with probability values of $< .05$. Data were analyzed with the SPSS statistical software (version 15.0; SPSS Inc, Chicago, IL).

FIGURE 1
Second harmonic generation microscopy image from cardiac tissue

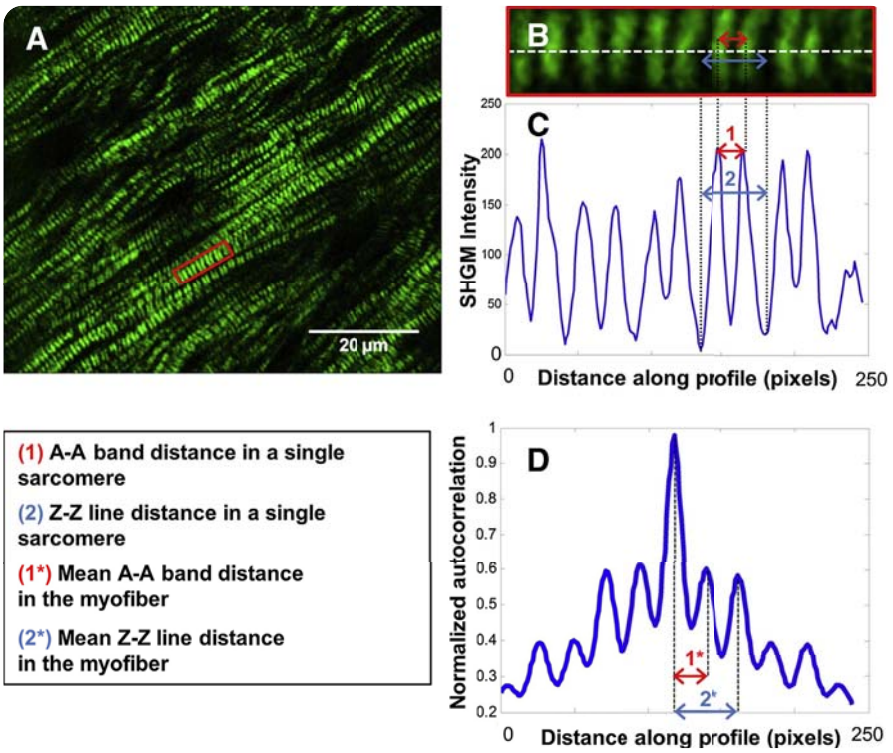

A, A typical second harmonic generation microscopy image of fetal cardiac tissue that can be measured readily when zoomed in (*red box*), as shown in **B**; **C,** second harmonic generation microscopy intensity profile from single myofiber to measure the intrasarcomeric A-A band distance (*red arrow*) and the sarcomere length or Z-Z line distance in a single sarcomere (*blue arrow*); **D,** normalized autocorrelation of the second harmonic generation microscopy intensity profile in the myofiber that was obtained by automated fiber profiling after the computation of local fiber orientation; the *red arrow* indicates the mean A-A band distance (*1**), and the *blue arrow* indicates the mean sarcomere length or Z-Z line distance in the myofibers (*2**).

SHGM, second harmonic generation microscopy.

Iruretagoyena. Ultrastructural changes of cardiomyocyte sarcomere in IUGR. Am J Obstet Gynecol 2014.

RESULTS

Study populations

Table 1 displays perinatal and Doppler data of the study groups. All included cases were very severe early-onset IUGR cases with a birthweight that ranged from 169-900 g. As expected, IUGR cases showed signs of placental insufficiency and hemodynamic redistribution by Doppler ultrasound evaluation and a lower birthweight percentile. The percentage of cardiac arrest with potassium chloride was similar among the study

TABLE 1
Prenatal Doppler evaluation and perinatal characteristics of the study groups

Variable	AGA	IUGR	*P* value
Prenatal ultrasound assessment			
Gestational age at scan, wk	22.2 (4)	22.0 (4)	.917
Umbilical artery pulsatility index (z-scores)	−0.2 (1.5)	20.6 (25.3)	.025
Middle cerebral artery pulsatility index (z-scores)	0.7 (1.4)	−1.5 (3.2)	.077
Cerebroplacental ratio (z-scores)	0.4 (1.2)	−3.5 (2.2)	.003
Perinatal characteristics			
Gestational age at delivery, wk	22.6 (3)	22.1 (5)	.894
Termination of pregnancy, %	100	44	.034
Cardiac arrest with potassium chloride, %	55	44	.996
Birthweight, g	590 (195)	350 (255)	.045
Birthweight percentile	45 (32)	0 (0)	.001
Heart/body weight ×100, g	0.56 (0.2)	0.83 (0.33)	.019

Data are given as median (interquartile range).

AGA, appropriate growth for gestational age; *IUGR*, intrauterine growth restriction.

Iruretagoyena. Ultrastructural changes of cardiomyocyte sarcomere in IUGR. Am J Obstet Gynecol 2014.

groups. Pregnancy termination in AGA was performed because of maternal schizophrenia (n = 1) or fetal agenesis of the corpus callosum (n = 5), hydrocephalus (n = 1), lissencephaly (n = 1), or neural tube defect (n = 1). Among cases, termination of pregnancy was indicated in 4 pregnancies at 22-23 weeks gestation because of maternal signs of severe preeclampsia together with severe IUGR. The remaining 5 IUGR cases were born on average at 25 weeks gestation and died in utero because of severe IUGR or within the first week of life because of respiratory complications of extreme prematurity. In all cases and control subjects, cardiac structural integrity was confirmed prenatally by ultrasound evaluation and at the autopsy. Heart/body weight was significantly increased in IUGR fetuses as compared with AGA fetuses.

TABLE 2
Ultrasound and blood cardiovascular markers in AGA and IUGR fetuses

Variable	AGA	IUGR	*P* value
Echocardiographic indices			
Ductus venosus pulsatility index (z-scores)	0 (0.7)	6.7 (7.3)	.014
Isovolumic contraction time (z-scores)	0.1 (0.8)	0.5 (2)	.089
Ejection time (z-scores)	0 (0.7)	−1.2 (3.1)	.056
Isovolumic relaxation time (z-scores)	0.2 (1)	3.9 (4.3)	.032
Left myocardial performance index (z-scores)	−0.1 (1)	4.7 (6.5)	.044
Left E/A ratio (z-scores)	0.1 (0.2)	2.3 (2.7)	.027
Right E/A ratio (z-scores)	−0.1 (0.9)	5.2 (8.5)	.011
Fetal blood biomarkers			
B-type natriuretic peptide, pg/mL	65 (48)	340 (538)	.004
Troponin-I, ng/mL	0.02 (0.02)	0.08 (0.60)	.069

Data are given as median (interquartile range).

AGA, appropriate growth for gestational age; *IUGR*, intrauterine growth restriction.

Iruretagoyena. Ultrastructural changes of cardiomyocyte sarcomere in IUGR. Am J Obstet Gynecol 2014.

Cardiovascular assessment

Table 2 displays results on cardiovascular assessment in cases and control subjects. IUGR fetuses showed signs of cardiac dysfunction denoted by increased ductus venosus-PI, MPI, diastolic ventricular filling ratios and fetal blood BNP concentrations. Troponin-I concentrations showed a nonsignificant trend to higher values in IUGR compared with AGA.

SHGM of heart tissue

Ultrastructural results are shown in Table 3 and Figures 1 and 2. SHGM showed a shorter sarcomere length in IUGR samples compared with AGA. There were significant differences in the distance between 2 Z-lines that delimited 1 sarcomere and a trend towards a decreased distance between intrasarcomeric A-bands.

Comment

This study provides evidence that IUGR is associated with cardiac dysfunction and ultrastructural cardiomyocyte changes in the form of shorter sarcomere length.

In the present study, IUGR fetuses showed signs of severe hemodynamic deterioration and cardiac dysfunction by echocardiography and cord blood BNP. This finding was expected because all cases were early-onset severe IUGR fetuses, and it is consistent with previous studies that demonstrated cardiac dysfunction in IUGR, which correlates linearly with the degree of fetal deterioration.[5-8] Increased BNP production may result from increased volume overload and/or by direct effect of hypoxia.[6-8]

Additionally, IUGR fetuses showed a nonsignificant trend to increased values of troponin-I, which is also in line with previous studies that have demonstrated signs of myocardial cell damage in growth restriction.[8] An increase in heart-to-body weight was also denoted in IUGR, which could be explained as a compensatory mechanism, and is consistent with some previous data from experimental models of severe IUGR.[30-32] Overall, the underlying pathophysiologic condition of cardiac remodeling and dysfunction in IUGR is complex because hypoxia and pressure plus volume overload may affect the developing myocardium.

The striking finding of this study was the observation of shorter sarcomere length in IUGR fetuses compared with AGA fetuses. The sarcomere is a key element of heart contractility. A shorter sarcomere has been described in experimental cardiac ischemic conditions.[33] Shorter sarcomeres have less actin and myosin cross bridges and less contractile force and reduced range of shortening.[34,35] Because cardiac energy consumption is dependent on the number of recruited cross bridges, a shorter sarcomere uses less energy contracting over a smaller distance, which allows the heart to be operative under energy restriction conditions.[35] As a tradeoff, shorter sarcomeres lose force and stability in unfavorable working conditions.[36,37] Shorter sarcomeres in IUGR might reflect an adaptive mechanism to cope with chronic oxygen and nutrient restriction. This would allow increased efficiency through lower energy consumption but result in reduced contractile function. Therefore, changes that have been observed in sarcomere length are consistent with reduced longitudinal systolic function and stroke volume that have been observed in IUGR fetuses and children.[8,9] This finding deserves further investigation to clarify the involvement of critical proteins for sarcomere structure and function, such as titin, myosin and myosin binding protein C, which previously have been described to be abnormal in IUGR [10,31] and in inherited and acquired cardiomyopathies.[38,39]

TABLE 3
Ultrastructural evaluation of sarcomere in AGA and IUGR fetuses

Variable	AGA	IUGR	*P* value
Intrasarcomere distance (A-A band), μm	0.76 (0.09)	0.73 (0.08)	.14
Sarcomere length (Z-Z line), μm	1.71 (0.15)	1.60 (0.12)	.02

Data are given as median (interquartile range).

AGA, appropriate growth for gestational age; *IUGR*, intrauterine growth restriction.

Iruretagoyena. Ultrastructural changes of cardiomyocyte sarcomere in IUGR. Am J Obstet Gynecol 2014.

This study has several limitations and considerations. First, the limited sample size probably has prevented the demonstration of statistically significant changes in the A-A band length and troponin-I concentrations. Second, we acknowledge that differences of perinatal outcome (mainly spontaneous vs elective termination of pregnancy), blood sampling, and body size could have interfered in the results. However, results were adjusted by fetal size, and the study populations showed a similar gestational age and percentage of cardiac arrest with potassium chloride. Third, it could be thought that sarcomere length differences could be attributed to differences in cardiac arrest on systole or diastole. We acknowledge that such differences have been described[40]; however, in our study, a similar proportion of subjects in each group received potassium chloride to arrest the heart in diastole. Subjects who were not arrested in diastole might have an ultrastructure closer to diastole than systole because any delay in fixative penetration into the tissue would allow sarcomeres to begin to relax.[40] Fourth, the study was limited to the left ventricle. We acknowledge that there might be regional changes among the ventricles that could have been overlooked in this study. Finally, the severity of the selected IUGR cases prevented us from drawing conclusions about milder forms of IUGR.

In conclusion, we have shown here that abnormal cardiac function that is observed in IUGR fetuses is associated with ultrastructural changes at cardiomyocyte sarcomere levels. These changes could represent part of the fetal adaptive response to the adverse environment of IUGR, which might help to

FIGURE 2
Sarcomere length in AGA and IUGR fetuses

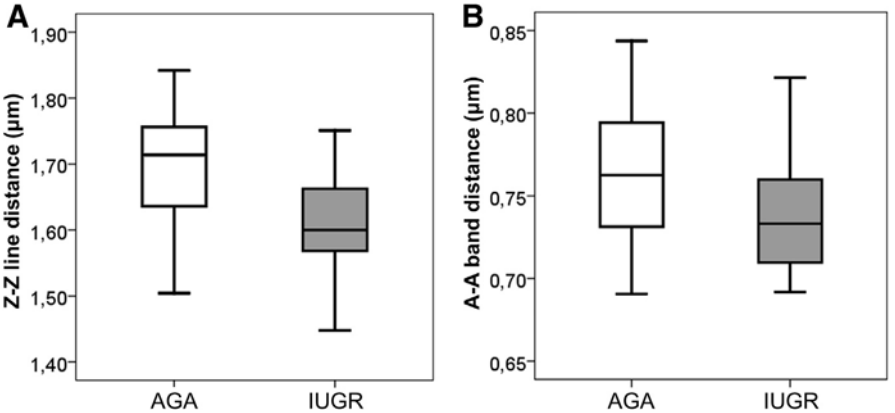

A, Sarcomere length or Z-Z line distance and **B,** intrasarcomere (A-A band) distance in normally grown and growth-restricted fetuses.

AGA, appropriate growth for gestational age; *IUGR*, intrauterine growth restriction.

Iruretagoyena. Ultrastructural changes of cardiomyocyte sarcomere in IUGR. Am J Obstet Gynecol 2014.

explain cardiovascular remodeling in utero and in childhood[9] and increased cardiovascular risk in adulthood[3] as described in IUGR. Further characterization of the sarcomere components and the molecules that are involved in their regulation is warranted to better understand their involvement in cardiac dysfunction in IUGR. The results of this study may open novel research lines that will aim to clarify the molecular mechanisms underlying cardiac adaptation and programming in IUGR. ■

ACKNOWLEDGMENTS

We thank Anna Bosch and Dr Maria Calvo from the Advanced Optical Microscopy Unit from Scientific and Technological Centres from the University of Barcelona for their support and advice with second harmonic generation and confocal techniques. The samples used in this project were provided by the Hospital Clínic-IDIBAPS Biobank with appropiate ethical approval.

REFERENCES

1. Alberry M, Soothill P. Management of fetal growth restriction. Arch Dis Child Fetal Neonatal Ed 2007;92:62-7.
2. Bernstein IM, Horbar JD, Badger GJ, et al. Morbidity and mortality among very low-birthweight neonates with intrauterine growth restriction: the Vermont Oxford Network. Am J Obstet Gynecol 2000;182:198-206.
3. Turan S, Turan OM, Salim M, et al. Cardiovascular transition to extrauterine life in growth-restricted neonates: relationship with prenatal Doppler findings. Fetal Diagn Ther 2013;33:103-9.
4. Barker DJ, Osmond C, Golding J, Kuh D, Wadsworth M. Growth in utero, blood pressure in childhood and adult life, and mortality from cardiovascular disease. BMJ 1989;298:564-7.
5. Hecher K, Campbell S, Doyle P, Harrington K, Nicolaides K. Assessment of fetal compromise by Doppler ultrasound investigation of the fetal circulation: arterial, intracardiac, and venous blood flow velocity studies. Circulation 1995;91:129-38.
6. Makikallio K, Vuolteenaho O, Jouppila P, Rasanen J. Ultrasonographic and biochemical markers of human fetal cardiac dysfunction in placental insufficiency. Circulation 2002;105:2058-63.
7. Girsen A, Ala-Kopsala M, Makikallio K, Vuolteenaho O, Rasanen J. Cardiovascular hemodynamics and umbilical artery N-terminal peptide of proB-type natriuretic peptide in human fetuses with growth restriction. Ultrasound Obstet Gynecol 2007;29:296-303.
8. Crispi F, Hernandez-Andrade E, Pelsers MM, et al. Cardiac dysfunction and cell damage across clinical stages of severity in growth-restricted fetuses. Am J Obstet Gynecol 2008;199:254.e1-8.
9. Crispi F, Bijnens B, Figueras F, et al. Fetal growth restriction results in remodeled and less efficient hearts in children. Circulation 2010;121:2427-36.
10. Tintu A, Rouwet E, Verlohren S, et al. Hypoxia induces dilated cardiomyopathy in the chick embryo: mechanism, intervention, and long-term consequences. PLoS One 2009;4:e5155.
11. Palinski W, Napoli C. Impaired fetal growth, cardiovascular disease, and the need to move on. Circulation 2008;117:341-3.
12. Carmignac V, Salih MA, Quijano-Roy S, et al. C-terminal titin deletions causes a novel early-onset myopathy with fatal cardiomyopathy. Ann Neurol 2007;61:340-51.
13. Carrier L, Bonne G, Bahrend E, et al. Organization and sequence of human cardiac myosin binding protein C gene (MYBPC3) and identification of mutations predicted to produce truncated proteins in familial hypertrophic cardiomyopathy. Circ Res 1997;80:427-34.
14. Sawyer DB, Peng X, Chen B, Pentassuglia L, Lim CC. Mechanisms of anthracycline cardiac injury: can we identify strategies for cardioprotection? Prog Cardiovasc Dis 2010;53:105-13.
15. Hanft LM, Korte FS, McDonald KS. Cardiac function and modulation of sarcomeric function by length. Cardiovasc Res 2008;77:627-36.
16. Campagnola PJ, Millard AC, Terasaki M, Hoppe PE, Malone CJ, Mohler WA. Three-dimensional high-resolution second-harmonic generation imaging of endogenous structural proteins in biological tissues. Biophys J 2002;81:493-508.
17. Plotnikov S, Juneja V, Isaacson A, Mohler W, Campagnola P. Optical clearing for improved contrast in second harmonic generation imaging of skeletal muscle. Biophys J 2006;90:328-39.
18. Kenny AM, Walsh SJ, Zubrowski B, et al. Measurement of muscle disease by quantitative second-harmonic generation imaging. J Biomed Opt 2008;13:044018.
19. Plotnikov SV, Millard A, Campagnola PJ, Mohler WA. Characterization of the myosin-based source for second-harmonic generation from muscle sarcomeres. Biophys J 2006;90:693-703.
20. Garcia-Canadilla P, Torre I, Gonzalez-Tendero A, et al. Automated morphometric characterization of cardiac fibers by second harmonic microscopy imaging. Proc IEEE Int Symp Biomed Imaging 2011:1379-82.
21. Figueras F, Meler E, Iraola A, et al. Customized birthweight standards for a Spanish population. Eur J Obstet Gynecol 2007;136:20-4.
22. Baschat AA, Gembruch U. The cerebroplacental Doppler ratio revisited. Ultrasound Obstet Gynecol 2003;21:124-7.
23. Hecher K, Campbell S, Snijders R, Nicolaides K. Reference ranges for fetal venous and atrioventricular blood flow parameters. Ultrasound Obstet Gynecol 1994;4:390-1.
24. Cruz-Martínez R, Figueras F, Bennasar M, et al. Normal reference ranges from 11 to 41 weeks' gestation of fetal left modified myocardial performance index by conventional Doppler with the use of stringent criteria for delimitation of the time periods. Fetal Diagn Ther 2012;32:79-86.
25. DeVore GR. Assessing fetal cardiac ventricular function. Semin Fetal Neonatal Med 2005;10:515-41.
26. Tsutsumi T, Ishii M, Eto G, Hota M, Kato H. Serial evaluation for myocardial performance index in fetuses and neonates using a new Doppler index. Pediatr Int 1999;41:722-7.
27. Tei C, Ling LH, Hodge DO, et al. New index of combined systolic and diastolic myocardial performance: a simple and reproducible measure of cardiac function: a study in normals and dilated cardiomyopathy. J Cardiol 1995;26:357-66.
28. Belenky A, Smith A, Zhang B, et al. The effect of class-specific protease inhibitors on the stabilization of B-type natriuretic peptide in human plasma. Clin Chim Acta 2004;340:163-72.
29. Boulesteix T, Beaurepaire E, Sauviat MP, Schanne-Klein MC. Second-harmonic microscopy of unstained living cardiac myocytes: measurements of sarcomere length with 20-nm accuracy. Opt Lett 2004;29:2031-3.
30. Wang KC, Zhang L, McMillen IC, et al. Fetal growth restriction and the programming of heart growth and cardiac insulin-like growth factor 2 expression in the lamb. J Physiol 2011;589:4709-22.
31. Xu Y, Williams SJ, O'Brien D, Davidge ST. Hypoxia or nutrient restriction during pregnancy in rats leads to progressive cardiac remodeling and impairs postischemic recovery in adult male offspring. FASEB J 2006;20:1251-3.
32. Lim K, Zimanyi MA, Black MJ. Effect of maternal protein restriction during pregnancy and lactation on the number of cardiomyocytes in the postproliferative weanling rat heart. Anat Rec (Hoboken) 2010;293:431-7.
33. Möllmann H, Nef HM, Kostin S, et al. Ischemia triggers BNP expression in the human myocardium independent from mechanical stress. Int J Cardiol 2010;143:289-97.
34. de Tombe PP, Mateja RD, Tachampa K, Mou YA, Farman GP, Irving TC. Myofilament length dependent activation. J Mol Cell Cardiol 2010;48:851-8.
35. Sela G, Yadid M, Landesberg A. Theory of cardiac sarcomere contraction and the

adaptive control of cardiac function to changes in demands. Ann N Y Acad Sci 2010;1188:222-30.

36. Agarkova I, Ehler E, Lange S, Schoenauer R, Perriard JC. M-band: a safeguard for sarcomere stability? J Muscle Res Cell Motil 2003;24:191-203.

37. Agarkova I, Perriard JC. The M-band: an elastic web that crosslinks thick filaments in the center of the sarcomere. Trends Cell Biol 2005;15:477-85.

38. Kruger M, Linke WA. Titin-based mechanical signalling in normal and failing myocardium. J Mol Cell Cardiol 2009;46:490-8.

39. Barefield D, Sadayappan. Phosphorylation and function of cardiac myosin protein-C in health and disease. J Mol Cell Cardiol 2010;48:866-75.

40. Sonnenblick EH, Ross J Jr, Covell JW, Spotnitz HM, Spiro D. The ultrastructure of the heart in systole and diastole. Changes in sarcomere length. Circ Res 1967;21:423-31.

5.4. STUDY 4

Permanent cardiac sarcomere changes in a rabbit model of intrauterine growth restriction

Torre I, González-Tendero A, García-Cañadilla P, Crispi F, García-García F, Bijnens B, Iruretagoyena I, Dopazo J, Amat-Roldán I, Gratacós E.

Status: submitted to PlosOne

Journal Impact Factor: 3.73

Quartile: 1st

Results from this study have been presented in

1. Torre I, Gonzalez-Tendero A, Garcia-Cañadilla P, Crispi F, Garcia-Garcia F, Iruretagoiena I, Dopazo J, Amat-Roldan I, Gratacos E. Sarcomere permanent morphometric changes underlie cardiac programming in intrauterine growth restriction. Frontiers in Cardiovascular Biology, European Society of Cardiology. London, UK. May 30 – April 1, 2012. Poster.

2. Garcia-Canadilla P, Torre I, Gonzalez-Tendero A, Iruretagoyena I, Eixarch E, Crispi F, Gratacos E, Amat-Roldan I. Automated morphometric characterization of cardiac fibers by second harmonic microscopy imaging. Proc IEEE Int Symp Biomed Imaging. 2011;1379-1382. Poster.

PERMANENT CARDIAC SARCOMERE CHANGES IN A RABBIT MODEL OF INTRAUTERINE GROWTH RESTRICTION

Iratxe Torre, PhD[1], Anna González-Tendero,MSc[1], Patricia García-Cañadilla, MSc[1,2], Fátima Crispi MD, PhD[1], Francisco García-García BSc[3,4], Bart Bijnens, PhD[6], Igor Iruretagoyena, MD[1], Joaquin Dopazo PhD[3,4,5] , Ivan Amat-Roldán, PhD[1] , Eduard Gratacós MD, PhD[1].

[1]BCNatal - Barcelona Center for Maternal-Fetal and Neonatal Medicine (Hospital Clínic and Hospital Sant Joan de Deu), IDIBAPS, University of Barcelona, and Centre for Biomedical Research on Rare Diseases (CIBER-ER), Barcelona, Spain; [2] Physense, Departament de Tecnologies de la Informació i les Comunicacions (DTIC), Universitat Pompeu Fabra, Barcelona, Spain; [3] Bioinformatics Department, Centro de Investigación Principe Felipe (CIPF). Avda. Autopista del Saler 16, 46012 Valencia, Spain; [4] Functional Genomics Node, INB, CIPF, Valencia, Spain; [5] Centro de Investigación Biomédica en Red de Enfermedades Raras (CIBERER). CIPF, Valencia, Spain; [6] ICREA – Universitat Pompeu Fabra, Barcelona, Spain

Correspondence:

Eduard Gratacós

BCNatal | Barcelona Center for Maternal Fetal and Neonatal Medicine

Hospital Clínic and Hospital Sant Joan de Déu

Sabino de Arana 1, 08028, Barcelona, Spain.

Phone: +34932279946 or +34932279906.

Fax: +34932275605. E-mail: gratacos@clinic.ub.es

ABSTRACT

Background: Intrauterine growth restriction (IUGR) induces fetal cardiac remodelling and dysfunction, which persists postnatally and may explain the link of low birth weight with increased cardiovascular mortality in adulthood. However, the cellular and molecular bases for these changes are not well understood. We tested the hypothesis that IUGR in a rabbit model is associated with structural and functional gene expression changes in the fetal sarcomere cytoarchitecture, which remain present in adulthood.

Methods and Results: IUGR was induced in New Zealand pregnant rabbits by selective ligation of the utero-placental vessels. Fetal echocardiography demonstrated more globular hearts and signs of cardiac dysfunction in IUGR as compared to controls. Second harmonic generation microscopy (SHGM) showed a shorter sarcomere, A-band and thick-thin filament interaction lengths that were already present *in utero* and persisted at 70 postnatal days (adulthood). Sarcomeric M-band (GO: 0031430) functional term was over-represented in gene expression bioinformatic set-analysis of IUGR fetal hearts.

Conclusion: The results suggest that IUGR induces cardiac dysfunction and permanent changes at the sarcomere level.

Key words: cardiovascular disease, echocardiography, intrauterine growth restriction, myocardium, sarcomere, second harmonic generation microscopy.

INTRODUCTION

Intrauterine growth restriction (IUGR) is a major cause of perinatal mortality and long term morbidity [1] affecting up to 7-10% of pregnancies. IUGR results in low birth weight, which has been epidemiologically associated with an increased risk of cardiovascular disease in adulthood [2] mediated by fetal cardiovascular programming. Fetuses with IUGR suffer from chronic oxygen and nutrients restriction [3], which most probably triggers an adaptive hemodynamic cardiovascular adaptation [4, 5] associated with *in utero* volume and pressure overload [6]. Consequently, IUGR fetuses and newborns show signs of cardiovascular remodelling and dysfunction, including reduced annular peak velocities [7] and increased carotid intima-media thickness [8]. These fetal changes seem to persist postnatally, resulting in cardiovascular remodelling, as shown in human children [9] and in adult animal models [10, 11]. Although the effects of IUGR on cardiac organ remodelling have been characterized, the features of cardiac fetal programming at subcellular scale are poorly documented. Identifying cellular involvement and molecular pathways of cardiac programming may provide a better understanding into the pathogenesis of the disease and could be an opportunity to design therapeutic interventions reducing the burden of cardiovascular disease from early life.

The sarcomere is the basic functional unit of the cardiac contractile machinery. Changes in sarcomere structure and its key proteins have been observed in models of cardiac dysfunction and failure [12 - 14]. In a previous experimental study, we demonstrated that chronic pre-natal hypoxia induced permanent post-natal changes in the isoforms and content of sarcomeric proteins, including titin and myosin [10]. Interestingly, in another recent study in human hearts, we have demonstrated that severe IUGR is associated with changes in sarcomere length together with signs of cardiac dysfunction [15]. Sarcomere length is strongly related to sarcomere function and contraction force, and has been described to be consistently altered in a substantial number of conditions associated with cardiac failure [16 – 18].

In the current study, we aim to evaluate the long term impact of IUGR on sarcomere structure in an experimental rabbit model of IUGR previously described by our group [19] that reproduces the main biometric and cardiovascular features observed in human IUGR. Hearts from IUGR fetuses as well as hearts from young adult rabbits were evaluated in order to assess the postnatal persistence of the changes on sarcomere architecture. Additionally, bioinformatics gene expression analysis of the fetal hearts combined with the functional interpretation of the global gene expression profile were also assessed to gain further insight on associated changes in pathways and proteins regulating the sarcomere.

METHODS

Experimental model of IUGR

New Zealand White rabbits were provided by a certified breeder and housed for 1 week before surgery in separate cages on a reversed 12/12 h light cycle. Dams were fed a diet of standard rabbit chow and water *ad libitum.* Animal handling and all procedures were carried out in accordance to applicable regulations and guidelines and with the approval of the Animal Experimental Ethics Committee of the University of Barcelona (permit number: 310/11 - 5999) and all efforts were made to minimize suffering.

Ten New Zealand White pregnant rabbits were used to reproduce a previously described experimental model of IUGR [19, 20]. Briefly, at 25 days of gestation dams were intramuscularly administered ketamine 35 mg/kg and xylazine 5mg/kg for anesthesia induction. Tocolysis (progesterone 0,9 mg/kg intramuscularly) and antibiotic prophylaxis (Penicillin G 300.000 UI endovenous) were administered prior to surgery. An abdominal midline laparotomy followed by the selective ligature of the 40-50% of the utero-placental vessels of each gestational sac was performed in all gestational sacs in one of the two uterine horns randomly selected. The gestational sacs in the other uterine horn were considered as normal growth controls as no ligature was performed. The abdomen was then closed and animals received subcutaneous meloxicam 0.4 mg/kg/24 h for 48 h, as postoperative analgesia. Five days after surgery, the same anaesthetic procedure was applied to perform a caesarean section. At this moment, fetal echocardiography was performed. Subsequently, rabbit kits were obtained and randomly assigned to two age study groups: i) fetal (30 days of gestation) and young adult (70 days post-natal) group. Hearts from rabbits included in the fetal group were obtained through a thoracotomy after anesthesia. Hearts for gene expression study were immediately snap frozen and stored at -80ºC until use. Hearts for multiphoton microscopy imaging were arrested in Ca^{2+}-free buffer and fixed in 4% paraformaldehyde in phosphate buffer for 24 hours at 4ºC. Fetuses included in the young adult group were breast-fed by a wet-nurse rabbit until the age of 25 days. At the age of 70 postnatal days, animals were anesthetized and hearts were excised and fixed in 4% paraformaldehyde in phosphate buffer.

Fetal echocardiography

Echocardiography was performed in 10 paired control and IUGR rabbit fetuses at the time of the caesarean section by placing the probe directly on the uterine wall using a Vivid q (General Electric Healthcare, Horten, Norway) 1.4-2.5 MHz phased array probe. The angle of insonation was kept <30º in all measurements and a 70 Hz high pass filter was used to avoid slow flow noise. Ultrasound evaluation included: (1) Ductus venosus

pulsatility index obtained in a midsagittal section or transverse section of the fetal abdomen positioning the Doppler gate at its isthmic portion; (2) Aortic isthmus pulsatility index obtained in a sagittal view of the fetal thorax with a clear view of the aortic arch placing the sample volume between the origin of the last vessel of aortic arch and the aortic joint of the ductus arteriosus; (3) Left and right sphericity indices calculated as base-to-apex length / basal ventricular diameter measured from 2-dimensional images in an apical 4-chamber view at end-diastole; (4) Left ventricular free wall thickness measured by M-mode in a transverse 4-chamber view; (5) Left ejection fraction estimated by M-mode from a transverse 4-chamber view according to Teicholz formula; (6) Longitudinal systolic (S') peak velocities at the mitral annulus measured by spectral tissue Doppler from an apical 4-chamber view.

Second Harmonic Generation Microscopy (SHGM)

Fixed fetal and young adult hearts were dehydrated and embedded in paraffin. Transversal 30 μm heart sections were cut in a microtome (Leica RM 2135) and mounted onto silane coated thin slides. After deparaffination with xylene and hydration with decreasing ethanol concentrations (100º / 96º / 70º), sections were covered with Mowiol 4-88 mounting medium (Sigma-Aldrich).

Detection of SHGM, from unlabelled cardiac tissue samples which were identified to contain mostly cardiomyocytes and no collagen, was performed with a Leica TCS-SP5 laser scanning spectral confocal multiphoton microscope (Leica Microsystems Heidelberg GmbH, Manheim, Germany) equipped with a Near Infrared laser (Mai Tai Broad Band 710-990 nm, 120 fempto second pulse), at the Advanced Optical Microscopy Unit from Scientific and Technological Centres from University of Barcelona. 7 control and 7 IUGR hearts from both the fetal and the young adult group were included in the analysis. For each heart, between 8 and 10 SHGM images, randomly chosen from the left ventricular mid-wall, were acquired. Each image included an average of 15 cardiac muscle fibers containing 200 sarcomeres approximately. The image resolution was 40 nm/pixel. Left ventricular cardiac fibers, which are mostly oriented in a single axis in optical sections of approximately 1.5 microns, were aligned at 45 degrees to maximize Signal to Noise Ratio (SNR) of SHGM. All tissue sections consisted of almost parallel fibres and were contained in a single plane by the sample preparation to avoid any bias in measurements. This certified that the statistical differences are related to group differences and contributions from other source of experimental error are marginal.

Figure 1 shows the distinctive biperiodic pattern of sarcomeres, imaged by means of SHGM, and their characterization by two distances in unstained intact sarcomeres: resting sarcomere lengths (SL), measured

as the distance between the two Z-discs delimiting each sarcomere; and intra-sarcomeric A-band lengths (ABL), defined as the distance between the two intra-sarcomeric segments of the A-band, divided by the M-band. Additionally, since SHGM arises from the thick-thin filament overlap in mature and developing sarcomeres [21], its length was calculated as the mean width of the A-band-related peak (namely in our study as thick-thin filament interaction length; TTIL). The three distinctive sarcomere distances (SL, ABL and TTIL) were measured automatically with a custom algorithm based on an optimal fitting of a parametric model of the autocorrelation function of the SHGM intensity profile in sarcomere fibers, as previously reported [22]. Briefly, the local orientation of the sarcomere fibers was estimated to perform automatically the following tracking of all the fibers within an image. After that, the SHGM intensity profile within each fiber was obtained and its autocorrelation function was computed. Finally, the autocorrelation function of the intensity profile was fitted with a parametric model to extract the average SL, ABL and TTIL of all the sarcomeres in the fiber. This calculation was performed for all the sarcomere fibers in the image. Additionally, a ratio between SL and ABL was calculated to further assess the quality of the acquired images and comparable physiological conditions between study groups. When this ratio was above 2.25, the sample was excluded from the analysis since the typical SHGM pattern of cardiac sarcomeres was lost.

Gene expression microarray

The gene expression profile was analyzed in 6 paired control and IUGR rabbit fetal hearts at 30 days of gestation as previously described [23]. This study focused on the expression profile of the cardiomyocyte contractile machinery - the sarcomere. Total RNA was isolated from left ventricle (RNeasy Mini kit, Qiagen), labelled with Quick Amp One-color Labelling kit (Agilent) and fluorochrome Cy3 and hybridized with a Rabbit Microarray (Agilent Microarray Design ID 020908). The hybridization was quantified at 5 μm resolution (Axon 4000B scanner) and data extraction was performed using Genepix Pro 6.0. Data obtained from the microarray were pre-processed and subjected to bioinformatics analysis from two viewpoints. Firstly, a differential gene expression *analysis* in order to identify up- or down-regulated individual genes associated with IUGR, carried out using the *limma* [24] package from Bioconductor (http://www.bioconductor.org/). Differential gene expression of the samples in each group was assessed with the adjusted P value for every gene included in the microarray and with the fold change. Multiple testing adjustments of p-values were done according to Benjamini and Hochberg [25] methodology. All the pre-processing steps described can be carried out with the Babelomics software [26].

Secondly, a gene set analysis was carried out for the Gene Ontology (GO) annotations using FatiScan [27], implemented in the Babelomics suite [28] as previously described [23]. FatiScan looks for modules of genes that are functionally related, based on various criteria such as common annotations as GO terms. GO terms were grouped in three classes: i) cellular components; ii) biological processes and iii) molecular functions. GO annotations for the genes in the microarray where taken from Blast2GO Functional Annotation Repository web page (http://bioinfo.cipf.es/b2gfar/) [29].The raw microarray data is deposited in the Gene Expression Omnibus database under accession number GSE37860.

Statistical Analysis

Data were analyzed with the statistical package SPSS 15.0 (version 15.0; SPSS Inc, Chicago, IL). Data are expressed as mean ± standard deviation or median (Interquartile range (IQR)). Paired comparisons between the control and IUGR groups were done with t-test analysis. Differences were considered significant with probability values of $p<0.05$. A classical parametric ANOVA test was carried out to compute significance between IUGR and control populations in experiments concerning SHGM analysis. Statistical methods related to the gene expression analysis have been detailed in its previous corresponding section.

RESULTS

Fetal biometric and echocardiographic results

Table 1 details the fetal biometric and echocardiographic data. While absolute fetal body and heart weights were significantly lower in IUGR, heart to body weight ratio was significantly increased in IUGR fetuses as compared to controls. Fetal echocardiography showed a more globular cardiac shape with lower right sphericity index but similar wall thickness in IUGR as compared to controls. Despite similar results in ejection fraction, mitral annular peak velocities (S') were significantly lower in IUGR as compared to controls. Additionally, ductus venosus and aortic isthmus pulsatility indices were significantly increased in IUGR fetuses.

Fetal sarcomere morphometry

Seven paired control and IUGR rabbits were quantified demonstrating a readily detectable SHGM signal from unstained left ventricular sarcomeres. A representative image is displayed in **Figure 2A** and a magnification of it is shown in **Figure 1**

As compared with controls, IUGR fetuses showed shorter sarcomere length (controls: 1.658 μm ± 0.094 vs. IUGR 1.531 μm ± 0.114, p=0.042) **(Figure 2B)**. Intra-sarcomeric A-band length was also found to be decreased by IUGR (controls 0.772 μm ± 0.044 vs. IUGR 0.705 μm ± 0.060, p=0.035) **(Figure 2C)**. Additionally, thick-thin filament interaction length was shorter in IUGR (controls 0.104 μm ± 0.006 vs. IUGR 0.096 μm ± 0.007, p=0.048) **(Figure 2D)**. The ratio between sarcomere length and intrasarcomeric A-band length was similar in the study groups (controls 2.15 ± 0.02 vs. IUGR 2.17 ± 0.03).

Post-natal persistence of cardiac sarcomeric changes

Unstained young adult rabbit sarcomeres from left ventricular samples, in seven paired control and IUGR rabbits (70 postnatal days), produced a readily detectable SHGM signal **(Figure 3A)** with a pattern similar to the one observed in fetal sarcomeres, with similar ratios between sarcomere length and intrasarcomeric A-band length (controls 2.11 ± 0.02 vs. IUGR 2.11 ± 0.01). A significant decrease in sarcomere length (controls 1.720 μm ± 0.068 vs. IUGR 1.626 μm ± 0.084 , p=0.04) and intrasarcomeric A-band length (controls 0.817 μm ± 0.036 vs. IUGR 0.772 μm ± 0.041, p=0.049) were observed in IUGR as compared to controls**(Figure 3B, C)**.

Additionally, sarcomeric thick-thin filament interaction length was shorter in IUGR (control 0.103 μm ± 0.005 vs. IUGR 0.097 μm ± 0.005, p=0.045) as compared to controls **(Figure 3D)**.

Bioinformatic analysis of gene expression microarray data

Differential gene expression

All experiments showed a good level of labelling and hybridization onto the Agilent microarray. Differential gene expression (when analysing for a fold change higher than 0.5 and an adjusted p-value lower than 0.05 - data not shown) was similar in both experimental conditions for all the cardiomyocyte sarcomere components included in the microarray.

Gene set analysis: functional interpretation of microarray data

A statistically significant enrichment in the group of genes composing the sarcomeric *M-band* (GO: 0031430) functional class (P raw <0.001; P adj =0.069) was observed in fetal IUGR hearts. The GO cellular component M-band is represented in **Figure 4** as an acyclic graph. *M band* annotation was found in 1.6 % of the most up-regulated genes in IUGR. On the other hand, only 0.69 % of the most down-regulated genes in IUGR contained the annotation (p value < 0.001; adjusted p-value < 0.1). **Table 2** shows the most relevant genes that define the *M band* (GO: 0031430). The remaining sarcomeric functional terms identified by the gene set analysis were not found to be significantly modified due to IUGR.

DISCUSSION

The present study shows an association between IUGR and fetal and postnatal permanent sarcomeric structural changes together with altered fetal cardiac function and sarcomere related gene expression changes. Since sarcomere length has been shown to have an important influence on cardiac contractility [30], the observed decrease in its length might be an important determinant of the currently described changes on cardiac shape and function. These findings provide important clinical and research suggestions that open future research to further characterize the molecular basis of cardiac dysfunction and remodelling observed in IUGR individuals.

The experimental approach used in this study chronically reduces the blood supply to the fetuses by performing a selective ligature of the uteroplacental vessels in pregnant rabbits [19], and has been shown to reproduce the main biometric and fetal hemodynamic features observed in human growth restriction [20]. Signs of fetal hypoxia are demonstrated by an increased pulsatility in the aortic isthmus flow as a reflection of the shift of blood towards the brain circulation in response to hypoxia, which is produced by a combination of brain vasodilation and systemic hypertension [31]. Additionally, the echocardiographic evaluation confirmed that IUGR results in more globular hearts, together with signs of systolic longitudinal dysfunction, which is similar to those observed in human fetuses and children [7, 9, 32].

Sarcomere length is important in myofilament force generation by different mechanisms since it has an effect on actin-myosin cross-bridge recruitment [33]. In this regard, sarcomere length is associated with the degree of thick-thin filament overlap, which affects the probability of actin-myosin cross-bridge formation and thus the capacity to generate force [34]. Shorter sarcomeres have been found in animal models of a variety of cardiac diseases, including ischemic contracture [16], diastolic dysfunction [17], and dilated cardiomyopathy and heart failure [18]. Additionally, in a recent paper using human biopsies, passive force-length analysis suggested a shorter sarcomere length in pressure-overloaded myocardium compared to volume overload and control donors [35]. We recently described changes on the cardiomyocyte intracellular organization in the same experimental animal model of IUGR [23] that resemble to changes induced by pressure overload [36]. The permanent changes in sarcomere structure, as observed here in IUGR, could be as well a response to the known sustained increase in fetal blood pressure that occurs in IUGR. Supporting this notion, recent findings suggest that isolated neonatal cardiomyocytes undergo structural modifications within their myofibrils in response to changes in environmental stiffness, resulting in differences in resting sarcomere length [37].

Additionally, the observed changes in sarcomere length are consistent with previous research where we showed that chronic prenatal hypoxia led to a shift in the expression of titin isoform N2BA (larger and more compliant isoform) towards isoform N2B (smaller and stiffer isoform) [10]. This protein extends from the center of the sarcomere to the *Z* line, thus acting as a developmental template for sarcomere assembly [38]. Titin is thought to be a major determinant of the sarcomere length [39, 17].

We recently published a work in which post-mortem cardiac samples from human fetuses that suffered severe IUGR were studied using the same SHGM methodology in order to assess changes in sarcomere morphometry [15]. Interestingly, results were strongly consistent with the ones described herein in the animal model: shorter sarcomere length in IUGR. This consistency strengthens the hypothesis that changes in sarcomere length could help to explain subclinical cardiac dysfunction previously described in human fetuses and children [9], and observed in IUGR rabbits in this study. The shorter sarcomere length and thick-thin filament interaction length might indicate a decrease in the number of binding events for cross-bridges between actin and myosin. Since cardiac muscle energy consumption depends on the number of recruited cross-bridges [40] shorter sarcomere length and thick-thin filament interaction length could be interpreted as an adaptive mechanism to cope with the oxygen and/or glucose restriction in IUGR. Importantly, in this study we show evidence of the postnatal persistence of the changes on sarcomere morphometry, which can not be assessed in humans. This observation might be relevant to explain the increased risk of cardiovascular disease and mortality in adult life related to IUGR as well as to understand the fetal cardiac programming.

Advanced bioinformatics analytic approaches were used in this study to complement the observations of SHGM and provide further evidence of the existence of functional gene expression differences encompassing structural changes. Fetal gene set analysis included a family of different tests designed to detect modules of functionally-related genes [41, 42]. Among them, we used FatiScan [27], integrated in Babelomics [26], which has been employed to successfully detect coordinated variations in blocks of genes [43]. The results demonstrated functional differences in a basic structure for the sarcomeric cytoskeleton, the M-band, which plays an important organizational role during myofibrillogenesis by performing the regular packing of the nascent thick (myosin) filaments [44]. This finding is in line with previous observations suggesting that specific structural alterations at the M-band might be part of a general adaptation of the sarcomeric cytoskeleton to unfavorable working conditions in early stages of dilated cardiomyopathy, correlating with an impaired ventricular function [45]. Moreover, they suggest an underlying basis for the abnormal sarcomere

cytoarchitecture observed in IUGR. Genes included in the M-band functional class involve a variety of associated molecules to this structure with key roles in sarcomere assembly and function, including titin, obscurin and myomesin. Interference with the physiological function of these proteins is of pathogenic relevance for human cardiomyopathies [46]. The findings warrant further investigation to clarify the individual role of sarcomere proteins in the generation of permanent structural changes of the contractile machinery under IUGR.

Several study limitations and technical considerations merit discussion. We used SHGM to measure sarcomere length. The technique has been validated to accurately visualize the SHGM signal produced by cardiac myosin thick filaments in unstained sarcomeres from different species with an accuracy of 20 nm [21, 22, 47]. SHGM offers comparable results to those provided by electron microscopy with the additional advantage of imaging larger tissue areas [22]. Sarcomere length values in this study were consistent with measurements using electron and light microscopy in fixed rabbit cardiomyocytes, and showed increasing values with cardiac maturation [48, 49]. The bioinformatics analysis of gene expression data used herein has been shown to be useful for studying diseases like IUGR in which subtle differences are expected. This study illustrates the existence of sarcomere changes, but it provides a limited view of the mechanistic or molecular pathways underlying such changes. We acknowledge that with the present study is difficult to address the actual biological relevance of the gene expression and bioinformatics analysis and future studies are required to gain further insight on the relevance and to elucidate pathways that might be responsible for the observed changes. Additionally, results provided by bioinformatics gene set analysis strongly depend on the capabilities of bioinformatics tools and gene annotations, which are constantly evolving. Thus, gene pathways that are not well described yet might remain undetectable with current tools

In conclusion, this study provides new clues towards understanding the cellular and molecular mechanisms underlying cardiac remodelling through fetal programming and persisting in adulthood. Together, the findings presented here support that IUGR induces permanent changes in cardiac sarcomere morphometry, associated with functional changes in proteins involved in sarcomere function and assembly. These changes might help to explain the stiffer and less deforming hearts of fetuses and adults suffering from IUGR, and open new lines of research aiming at characterizing and interfering with the mechanisms of adaptation leading to cardiovascular remodelling in IUGR.

ACKNOWLEDGEMENTS

We thank Anna Bosch and Dr Maria Calvo from the Advanced Optical Microscopy Unit from Scientific and Technological Centres from University of Barcelona, for their support and advice with Second Harmonic Generation Microscopy techniques.

FUNDING SOURCES

This study was supported by grants from Ministerio de Economia y Competitividad PN de I+D+I 2008-2011 (ref. SAF2009_08815, SAF2012-37196 and BIO2011-27069); Instituto de Salud Carlos III (ref. PI11/00051, PI11/01709, PI12/00801) cofinanciado por el Fondo Europeo de Desarrollo Regional de la Unión Europea "Una manera de hacer Europa"; Centro para el Desarrollo Técnico Industrial (Ref. cvREMOD 2009-2012) apoyado por el Ministerio de Economia y Competitividad y Fondo de inversión local para el empleo, Spain; The Cerebra Foundation for the Brain Injured Child (Carmarthen, Wales, UK); Obra Social "La Caixa" (Spain); Fundació Mutua Madrileña (Spain); Fundació Agrupació Mutua (Spain); AGAUR 2009 SGR grant nº 1099 and Red Temática de Investigación Cooperativa en cancer (ref. RD06/0020/1019). I.T. was supported by a post-doctoral fellowship from Carlos III Institute of Health (Spain) (CD08/00176) during the time these studies were performed. P.G.C. acknowledges grant support to the Programa de Ayudas Predoctorales de Formación en Investigación en Salud del Instituto Carlos III, Spain (FI12/00362). A.G.T. was supported by an IDIBAPS (Institut d'Investigacions Biomèdiques August Pi i Sunyer) predoctoral fellowship.

DISCLOSURES

None.

REFERENCES

1. Alberry M, Soothill P (2007) Management of fetal growth restriction. Arch Dis Child Fetal Neonatal Ed 92: F62-F67.
2. Barker DJ (1999) Fetal origins of cardiovascular disease. Ann Med 1: 3-6.
3. Soothill PW, Nicolaides KH, Campbell S (1987) Prenatal asphyxia, hyperlacticaemia, hypoglycaemia, and erythroblastosis in growth retarded fetuses. BMJ 294: 1051–1053.
4. Hecher K, Campbell S, Doyle P, Harrington K, Nicolaides K (1995) Assessment of fetal compromise by Doppler ultrasound investigation of the fetal circulation. Circulation 91: 129-138.
5. Tchirikov M, Schroder HJ, Hecher K (2006) Ductus venosus shunting in the fetal venous circulation: regulatory mechanisms, diagnostic methods and medical importance. Ultrasound Obstet Gynecol 27: 452–461.
6. Verburg BO, Jaddoe VW, Wladimiroff JW, Hofman A, Witteman JC, Steegers EA (2008) Fetal hemodynamic adaptive changes related to intrauterine growth: the Generation R Study. Circulation 117: 649-659.
7. Comas M, Crispi F, Cruz-Martinez R, Martinez JM, Figueras F, Gratacós E (2010) Usefulness of myocardial tissue Doppler vs. conventional echocardiography in the evaluation of cardiac dysfunction in early-onset intrauterine growth restriction. Am J Obstet Gynecol 203: 45.e1-45.e7.
8. Skilton MK, Evans N, Griffiths KA, Harmer JA, Celermajer D (2005) Aortic wall thickness in newborns with intrauterine restriction. Lancet 23: 1484–1486.
9. Crispi F, Bijnens B, Figueras F, Bartrons J, Eixarch E, et al. (2010) Fetal growth restriction results in remodeled and less efficient hearts in children. Circulation 121: 2427-2436.
10. Tintu A, Rouwet E, Verlohren S, Brinkmann J, Ahmad S, et al. (2009) Hypoxia induces dilated cardiomyopathy in the chick embryo: mechanism, intervention, and long-term consequences. PLoS One 4: e5155.
11. Ream M, Ray AM, Chandra R, Chikaraishi DM (2008) Early fetal hypoxia leads to growth restriction and myocardial thinning. Am J Physiol Regul Integr Comp Physiol 295: R583-595.
12. Haddad F, Bodell PW, Baldwin KM (1995) Pressure-induced regulation of myosin expression in rodent heart. J Appl Physiol 4: 1489-1495.
13. Warren CM, Jordan MC, Roos KP, Krzesinski PR, Greaser ML (2003) Titin isoform expression in normal and hypertensive myocardium. Cardiovasc Res 59: 86-94.

14. Falcão-Pires I, Palladini G, Gonçalves N, van der Velden J, Moreira-Gonçalves D, et al. (2011) Distinct mechanisms for diastolic dysfunction in diabetes mellitus and chronic pressure-overload. Basic Res Cardiol 106: 801-814.
15. Iruretagoyena JI, Gonzalez-Tendero A, Garcia-Canadilla P, Amat-Roldan I, Torre I, Nadal A, Crispi F, Gratacos E (2014) Cardiac dysfunction is associated with altered sarcomere ultrastructure in intrauterine growth restriction. Am J Obstet Gynecol doi: 10.1016/j.ajog.2014.01.023.
16. Anderson PG, Bishop SP, Digerness SB (1987) Transmural progression of morphologic changes during ischemic contracture and reperfusion in the normal and hypertrophied rat heart. Am J Phatol 129: 152-167.
17. Radke MH, Peng J, Wu Y, McNabb M, Nelson OL, et al. (2007) Targeted deletion of titin N2B region leads to diastolic dysfunction and cardiac atrophy. Proc Natl Acad Sci U S A 104: 3444-3449.
18. Chen JF, Murchison EP, Tang R, Callis TE, Tatsuguchi M, et al. (2008) Targeted deletion of Dicer in the heart leads to dilated cardiomyopathy and heart failure. Proc Natl Acad Sci U S A 105: 2111-2116.
19. Eixarch E, Figueras F, Hernandez-Andrade E, Crispi F, Nadal A, et al. (2009) An experimental model of fetal growth restriction based on selective ligature of uteroplacental vessels in the pregnant rabbit. Fetal Diagn Ther 26: 203-211.
20. Eixarch E, Hernandez-Andrade E, Crispi F, Illa M, Torre I, et al. (2011) Impact on fetal mortality and cardiovascular Doppler of selective ligature of uteroplacental vessels compared with undernutrition in a rabbit model of intrauterine growth restriction. Placenta 32: 304-309.
21. Plotnikov SV, Millard AC, Campagnola PJ, Mohler WA (2006) Characterization of the myosin-based source for second-harmonic generation from muscle sarcomeres. Biophys J 90: 693-703.
22. Garcia-Cañadilla P, Torre I, González-Tendero A, Iruretagoyena I, Eixarch E, et al. (2011) Automated morphometric characterization of cardiac fibers by second harmonic microscopy imaging. Proc IEEE Int Symp Biomed Imaging 1379-1382. Conference paper.
23. Gonzalez-Tendero A, Torre I, Garcia-Canadilla P, Crispi F, García-García F, et al. (2013) Intrauterine growth restriction is associated with cardiac ultrastructural and gene expression changes related to the energetic metabolism in a rabbit model. Am J Physiol Heart Circ Physiol 305: H1752–H1760.
24. Smyth GK (2004) Linear models and empirical bayes methods for assessing differential expression in microarray experiments. Stat Appl Genet Mol Biol 3: Article3.

25. Benjamini Y, Hochberg Y (1995) Controlling the false discovery rate a practical and powerful approach to multiple testing. J R Statist Soc B 57: 289-300.
26. Medina I, Carbonell J, Pulido L, Madeira SC, Goetz S, et al. (2010) Babelomics: an integrative platform for the analysis of transcriptomics, proteomics and genomic data with advanced functional profiling. Nucleic Acids Res 38: W210-W213.
27. Al-Shahrour F, Arbiza L, Dopazo H, Huerta-Cepas J, Mínguez P, et al. (2007) From genes to functional classes in the study of biological systems. BMC Bioinformatics 8: 114.
28. Al-Shahrour F, Carbonell J, Minguez P, Goetz S, Conesa A, et al. (2008) Babelomics: advanced functional profiling of transcriptomics, proteomics and genomics experiments. Nucleic Acids Res 36: W341-346.
29. Götz S, Arnold R, Sebastián-León P, Martín-Rodríguez S, Tischler P, et al. (2011) B2G-FAR, a species-centered GO annotation repository. Bioinformatics 27: 919-924.
30. Fukuda N, Sasaki D, Ishiwata S, Kurihara S (2001) Length dependence of tension generation in rat skinned cardiac muscle: role of titin in the Frank-Starling mechanism of the heart. Circulation 104: 1639-1645.
31. Fouron JC, Skoll A, Sonesson SE, Pfizenmaier M, Jaeggi E, Lessard M (1999) Relationship between flow through the fetal aortic isthmus and cerebral oxygenation during acute placental circulatory insufficiency in ovine fetuses. Am J Obstet Gynecol 181: 1102-1107.
32. Crispi F, Hernandez-Andrade E, Pelsers MM, Plasencia W, Benavides-Serralde JA, et al. (2008) Cardiac dysfunction and cell damage across clinical stages of severity in growth-restricted fetuses. Am J Obstet Gynecol 199: 254.e1-254.e8.
33. Wannenburg T, Heijne GH, Geerdink JH, Van Den Dool HW, Janssen PM, de Tombe PP (2000) Cross-bridge kinetics in rat myocardium: effect of sarcomere length and calcium activation. Am J Physiol Heart Circ Physiol 279: H779-H790.
34. Gordon AM, Homsher E, Regnier M (2000) Regulation of contraction in striated muscle. Physiol Rev 80: 853-924.
35. Chaturvedi RR, Herron T, Simmons R, Shore D, Kumar P, et al. (2010) Passive stiffness of myocardium from congenital heart disease and implications for diastole. Circulation 121: 979-988.

36. Schwarzer M, Schrepper A, Amorim PA, Osterholt M Doenst T (2012) Pressure Overload Differentially Affects Respiratory Capacity in Interfibrillar and Subsarcolemmal Mitochondria. Am J Physiol Heart Circ Physiol 304: H529-H537.
37. Rodriguez AG, Han SJ, Regnier M, Sniadecki NJ (2011) Substrate stiffness increases twitch power of neonatal cardiomyocytes in correlation with changes in myofibril structure and intracellular calcium. Biophys J 101: 2455-2464.
38. Tskhovrebova L, Trinick J (2003) Titin: properties and family relationships. Nat Rev Mol Cell Biol 4: 679-689.
39. Labeit S, Kolmerer B, Linke WA (1997) The giant protein titin. Emerging roles in physiology and pathophysiology. Circ Res 80: 290-294.
40. Sela G, Yadid M, Landesberg A (2010) Theory of cardiac sarcomere contraction and the adaptive control of cardiac function to changes in demands. Ann N Y Acad Sci 1188: 222-230.
41. Mootha VK, Lindgren CM, Eriksson KF, Subramanian A, Sihag S, et al. (2003) PGC-1alpha-responsive genes involved in oxidative phosphorylation are coordinately downregulated in human diabetes. Nat Genet 34: 267-273.
42. Kim SY, Volsky DJ (2005) PAGE: parametric analysis of gene set enrichment. BMC Bioinformatics 6: 144.
43. Prado-Lopez S, Conesa A, Armiñán A, Martínez-Losa M, Escobedo-Lucea C, et al. (2010) Hypoxia promotes efficient differentiation of human embryonic stem cells to functional endothelium. Stem Cells 28: 407-418.
44. Agarkova I, Perriard JC (2005) The M-band: an elastic web that crosslinks thick filaments in the center of the sarcomere. Trends Cell Biol 15: 477-485.
45. Schoenauer R, Emmert MY, Felley A, Ehler E, Brokopp C, et al. (2011) EH-myomesin splice isoform is a novel marker for dilated cardiomyopathy. Basic Res Cardiol 106: 233-247.
46. Fukuzawa A, Lange S, Holt M, Vihola A, Carmignac V, et al (2008). Interactions with titin and myomesin target obscurin and obscurin-like 1 to the M-band: implications for hereditary myopathies. J Cell Sci 121: 1841-1851.
47. Boulesteix T, Beaurepaire E, Sauviat MP, Schanne-Klein MC (2004) Second-harmonic microscopy of unstained living cardiac myocytes: measurements of sarcomere length with 20-nm accuracy. Opt Lett 29: 2031-2033.

48. Nassar R, Reedy MC, Anderson PA (1987) Developmental changes in the ultrastructure and sarcomere shortening of the isolated rabbit ventricular myocyte. Circ Res 61: 465-483.
49. Wu Y, Wu EX (2009) MR study of postnatal development of myocardial structure and left ventricular function. J Magn Reson Imaging 30: 47-53.

FIGURE LEGENDS

Figure 1. Schematic representation of the sarcomere cytoskeleton distances. **A**, an illustration of the sarcomere elementary parts; **B**, a sarcomere image by electron microscopy; **C**, a SHGM image of a myofibril; and **D**, a SHGM intensity profile along the myofibril showing the distances measured to characterize the sarcomere cytoskeleton: sarcomere length (SL), intra-sarcomeric A-band lengths (ABL) and thick-thin filament interaction length (TTIL).

Figure 2. Ultrastructural sarcomere changes in fetal hearts from IUGR and controls. A, A representative SHGM image from unstained fetal rabbit left ventricle. The sarcomeres are clearly delimited by thick black lines (Z-discs) and the SHGM signal originates from the thick myosin filaments (in green). In the central region of the myosin filaments appears a thinner black line, identified as the M-band. Scale bar= 20 μm. **B** and **C,** show average distances between two consecutives Z-discs (SL) and intrasarcomeric A-bands (ABL), respectively. **D,** shows thick-thin filament interaction length (TTIL), as the mean width of the A-band-related peaks. Data are expressed as mean ± SD.

Figure 3. Ultrastructural sarcomere changes in adult hearts from IUGR and controls. A, Representative SHGM image from unstained adult rabbit left ventricle. Scale bar= 20 μm. **B** and **C,** show average distances between two consecutive Z discs (SL) and two intrasarcomeric A bands (ABL), respectively. **D,** shows the length of thick-thin filament interaction length (TTIL). Data are expressed as mean ± SD.

Figure 4. Gene ontology analysis. Acyclic graph showing the M-line cellular component significantly over-represented (in red) in IUGR compared to healthy control hearts. In the GO hierarchy, biological knowledge can be represented as a tree where functional terms near the root of the tree make reference to more general concepts while deeper functional terms near the leaves of the tree make reference to more specific concepts. If a gene is annotated to a given level, then is automatically considered to be annotated at all the upper levels up to the root.

TABLES

Table 1. Fetal biometric and echocardiographic results in IUGR and control fetuses.

	Control	IUGR	P-value
N	10	10	
Fetal Biometry			
Fetal weight (g)	48.97 (12.46)	29.94 (7.72)	0.000 *
Heart weight (g)	0.37 (0.10)	0.29 (0.09)	0.006 *
Heart weight / Fetal weight)*100	0.79 (0.11)	1.10 (0.31)	0.009 *
Fetal hemodynamics			
Ductus venosus pulsatility index	0.75 (0.25)	1.33 (0.75)	0.008 *
Aortic isthmus pulsatility index	3.05 (0.45)	3.85 (1.16)	0.009 *
Cardiac morphometry			
Left sphericity index	1.54 (0.34)	1.51 (0.26)	0.073
Right sphericity index	1.56 (0.24)	1.32 (0.23)	0.004 *
Left ventricle wall thickness (mm)	1.45 (0.37)	1.41 (0.31)	0.978
Systolic function			
Left ejection fraction (%)	89.1 (8.2)	82 (24.6)	0.39
Mitral annular systolic peak velocity (cm/s)	1.91 (0.27)	1.59 (0.33)	0.046 *

All values are median (interquartile range). P-value was calculated by t-test. *g:* grams; *mm:* millimeters; *cm/s*: centimetres/second.

Table 2. Results from most relevant sequences included in M-band functional class identified by FatiScan gene set analysis (M-band (GO: 0031430) block of genes). A fold change value above 0 indicates up-regulation in IUGR vs. controls.

Name	ID	Fold change
OBSCN (Obscurin)	ENSOCUT00000011554	0.266
OBSL (Obscurin-like protein 1)	ENSOCUT00000011142	0.171
Titin	ENSOCUT00000016899	0.265
Myopalladin	ENSOCUT00000009940	0.405
Myomesin-2	ENSOCUT00000013143	0.265

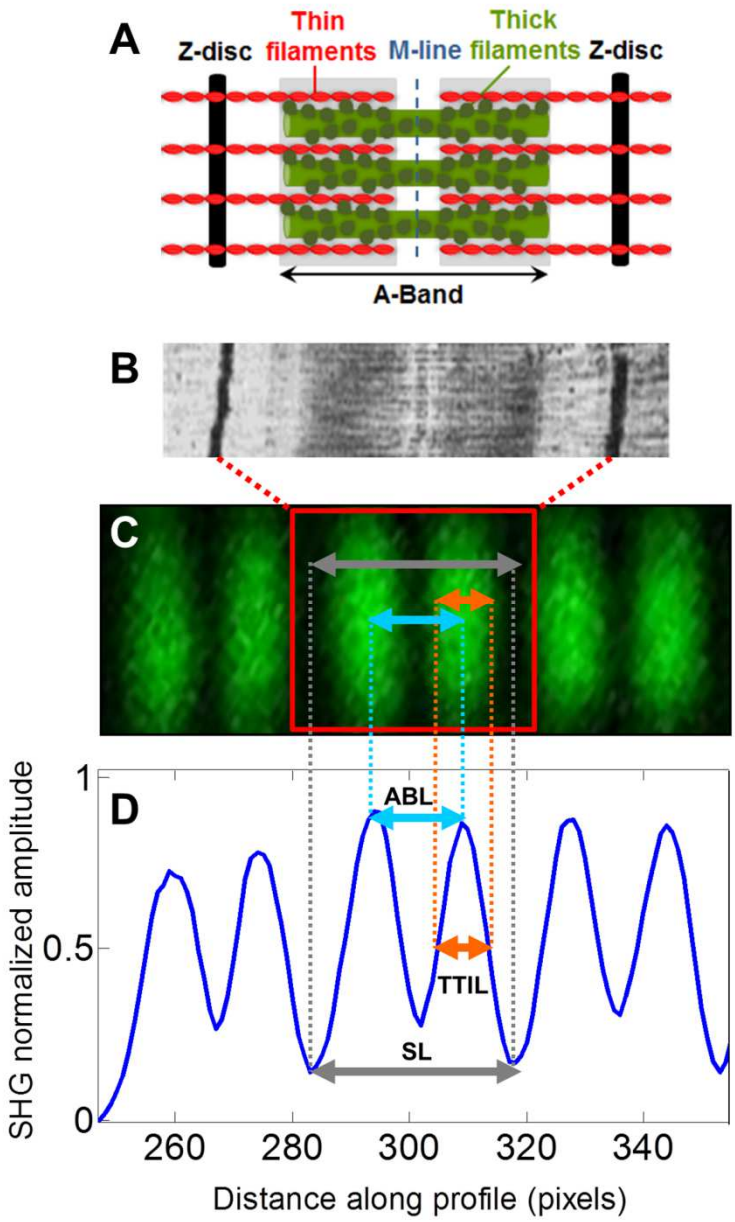
A
Thin
filaments
Thick
filaments
Z-disc
M-line
Z-disc
A-Band
B
C
D
ABL
TTIL
SL
SHG normalized amplitude
1
0.5
0
260
280
300
320
340
Distance along profile (pixels)

Figure 1.

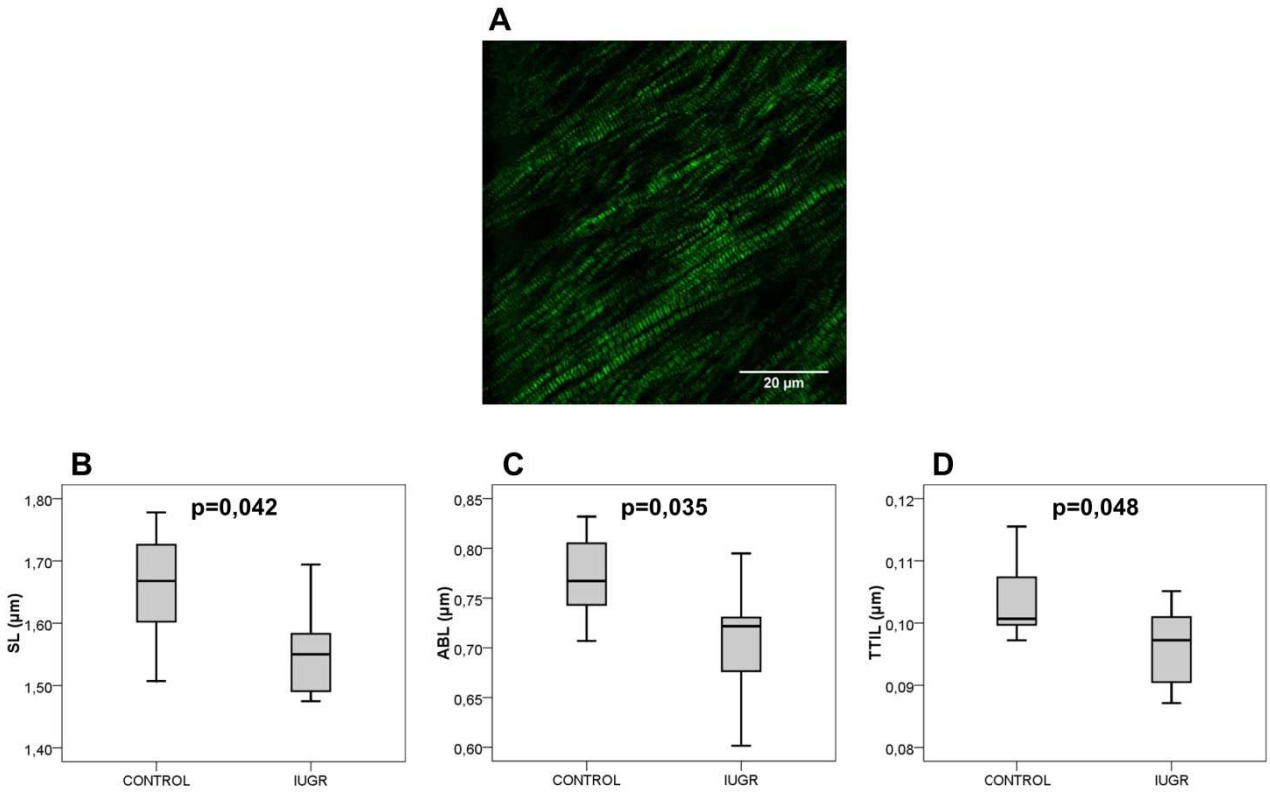
A
20 µm
B
p=0,042
SL (µm)
1,80
1,70
1,60
1,50
1,40
CONTROL
IUGR
C
p=0,035
ABL (µm)
0,85
0,80
0,75
0,70
0,65
0,60
CONTROL
IUGR
D
p=0,048
TTIL (µm)
0,12
0,11
0,10
0,09
0,08
CONTROL
IUGR

Figure 2.

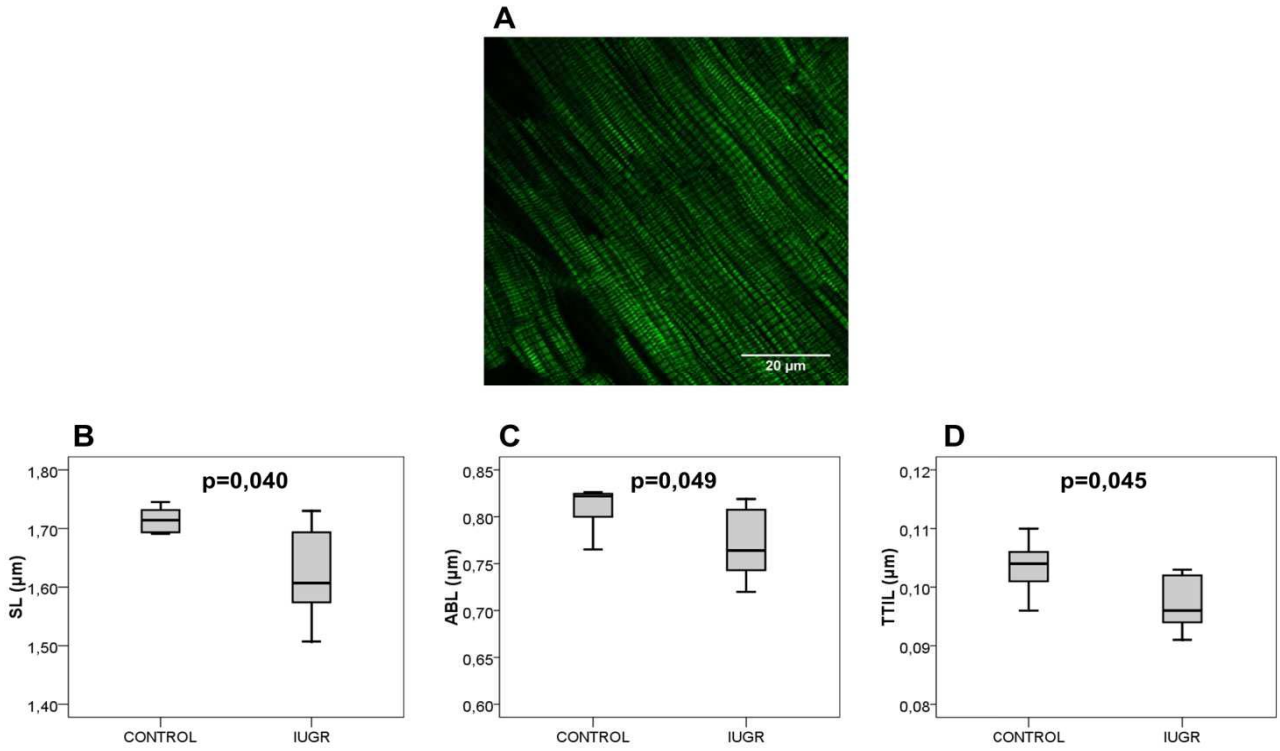
A
20 µm
B
p=0,040
SL (µm)
1,80
1,70
1,60
1,50
1,40
CONTROL
IUGR
C
p=0,049
ABL (µm)
0,85
0,80
0,75
0,70
0,65
0,60
CONTROL
IUGR
D
p=0,045
TTIL (µm)
0,12
0,11
0,10
0,09
0,08
CONTROL
IUGR

Figure 3.

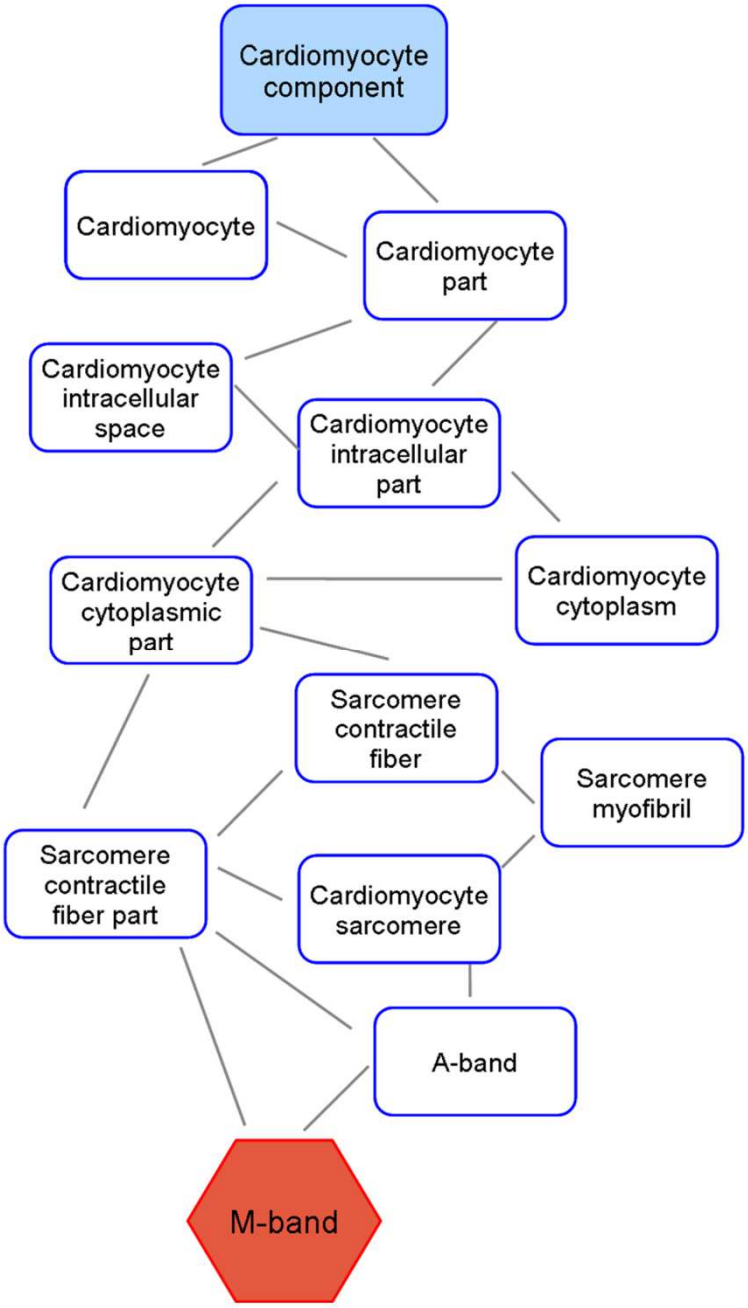
Cardiomyocyte component
Cardiomyocyte
Cardiomyocyte part
Cardiomyocyte intracellular space
Cardiomyocyte intracellular part
Cardiomyocyte cytoplasmic part
Cardiomyocyte cytoplasm
Sarcomere contractile fiber
Sarcomere myofibril
Sarcomere contractile fiber part
Cardiomyocyte sarcomere
A-band
M-band

Figure 4.

6. RESULTS

6. RESULTS

6.1 Lower birthweight and signs of placental insufficiency in IUGR

Human IUGR population (study 3)

For the human IUGR population, Table 2 displays perinatal and Doppler data. All included cases were very severe early-onset IUGR cases with a birthweight ranging from to 169 to 900 g. As expected IUGR cases showed signs of placental insufficiency and hemodynamic redistribution by Doppler ultrasound, and a lower birthweight centile. The percentage of cardiac arrest with potassium chloride was similar among the study groups. Pregnancy termination in controls was performed due to maternal schizophrenia (1) or fetal agenesis of the corpus callosum (5), hydrocephalus (1), lissencephaly (1) or neural tube defect (1). Among cases, termination of pregnancy was indicated in four pregnancies at 22-23 weeks due to maternal signs of severe preeclampsia together with severe IUGR. The remaining five IUGR cases were born on average at 25 weeks and died in utero due to severe IUGR or within the first week of life due to respiratory complications of extreme prematurity. In all cases and controls cardiac structural integrity was confirmed prenatally by ultrasound and at the autopsy. Heart/body weight was significantly increased in IUGR fetuses as compared to controls

Table 2. Prenatal Doppler evaluation and perinatal characteristics of the study groups.

	Control	IUGR	*P-value*
Prenatal ultrasound assessment			
Gestational age at scan (weeks)	22.2 (4)	22.0 (4)	*0.917*
Umbilical artery pulsatility index (z-scores)	-0.2 (1.5)	20.6 (25.3)	*0.025**
Middle cerebral artery pulsatility index (z-scores)	0.7 (1.4)	-1.5 (3.2)	*0.077*
Cerebroplacental ratio (z-scores)	0.4 (1.2)	-3.5 (2.2)	*0.003**
Perinatal characteristics			
Gestational age at delivery (weeks)	22.6 (3)	22.1 (5)	*0.894*
Termination of pregnancy (%)	100%	44%	*0.034**
Cardiac arrest with potassium chloride (%)	55%	44%	*0.996*
Birthweight (g)	590 (195)	350 (255)	*0.045**
Birthweight percentile	45 (32)	0 (0)	*0.001**
Heart/body weight (x100) (g)	0.56 (0.2)	0.83 (0.33)	*0.019**

Data are expressed as median (interquartile range). * p-value < 0.05.

Experimental model of IUGR (studies 1, 2 and 4)

Biometric outcome of the study groups of the experimental model of IUGR is summarized in Table 3. Birth weight, placental weight, heart weight, crown-rump length and abdominal girth decreased significantly in IUGR kits compared to normally growth kits. Additionally, heart to body weight ratio was increased in the IUGR group.

Table 3. Biometry in experimental groups of the animal model of IUGR.

	Control	IUGR	P value
Birth weight (g)	49.24±8.03	29,76±5.99	0.000*
Heart weight (g)	0.43±0.07	0.29±0.07	0.001*
Heart/body weight (x100) (g)	0.84±0.12	1.02±0.11	0.009*
Placental weight (g)	3.86±1.06	2.23±0.37	0.028*
Crown-rump length (mm)	10.56±0.46	8.94±1.05	0.004*
Abdominal girth	7.47±0.93	6.38±0.65	0.048*

Data are expressed as mean ± SD. * p-value < 0.05.

6.2. Abnormal cardiac fiber orientation and dilated coronary arteries in IUGR (study 1)

The postprocessing and analysis of the images obtained from X-ray phase contrast synchrotron radiation-based micro-CT shows changes on the cardiac detailed anatomy, myofiber structure and vasculature in IUGR fetal hearts compared to fetal control hearts.

In Figure 6, detailed cardiac anatomy of control and IUGR fetal hearts can be appreciated. It shows surface rendered images of cuts trough two fetal rabbit hearts. The IUGR heart (right) is clearly smaller than the normal one (left). Additionally, the coronaries are clearly dilated and much more prominent in the IUGR heart.

Figure 7 (left) shows the local helix angle of the fibres within a slice of the fetal rabbit myocardial wall with a visualisation of the resulting 3D fibre structure at the right. The gradual change from predominantly longitudinal at the epicardial side, towards more circumferential in the mid-myocardium and again longitudinal at the epicardial side of the left ventricle can be observed. A rather abrupt change in the mid of the interventricular septum is present. In IUGR, predominantly in the RV wall, there seems a reduction in the longitudinally oriented fibres with more predominance of the circumferential ones.

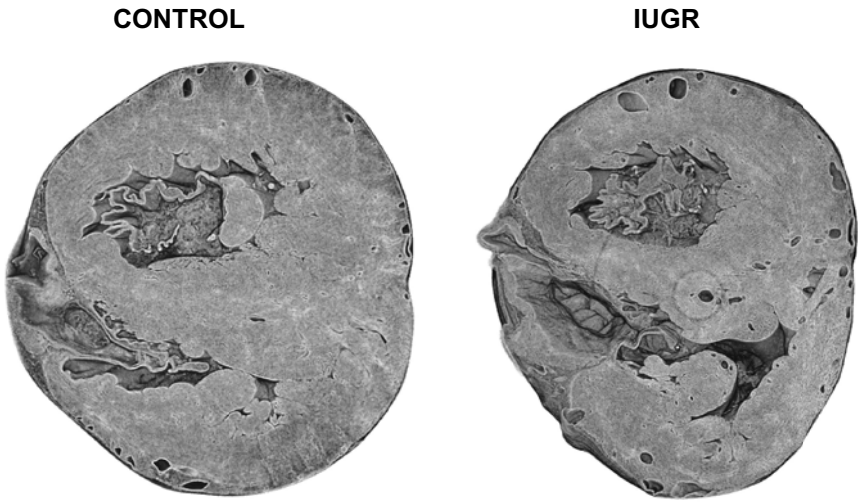

Figure 6. Volume rendered images depicting detailed cardiac anatomy. IUGR heart (right) is smaller and with thinner walls compared to the control heart (left). Additionally, it can be appreciated that coronary vessels are clearly dilated and much more prominent in the IUGR heart.

The dilatation of the coronary arteries in IUGR fetal rabbit hearts is clearly visible in Figure 8 where it can be oserved and quantified. It shows the segmented arterial trees (top) as well as a visualisation of the local radius of the vessels (bottom).

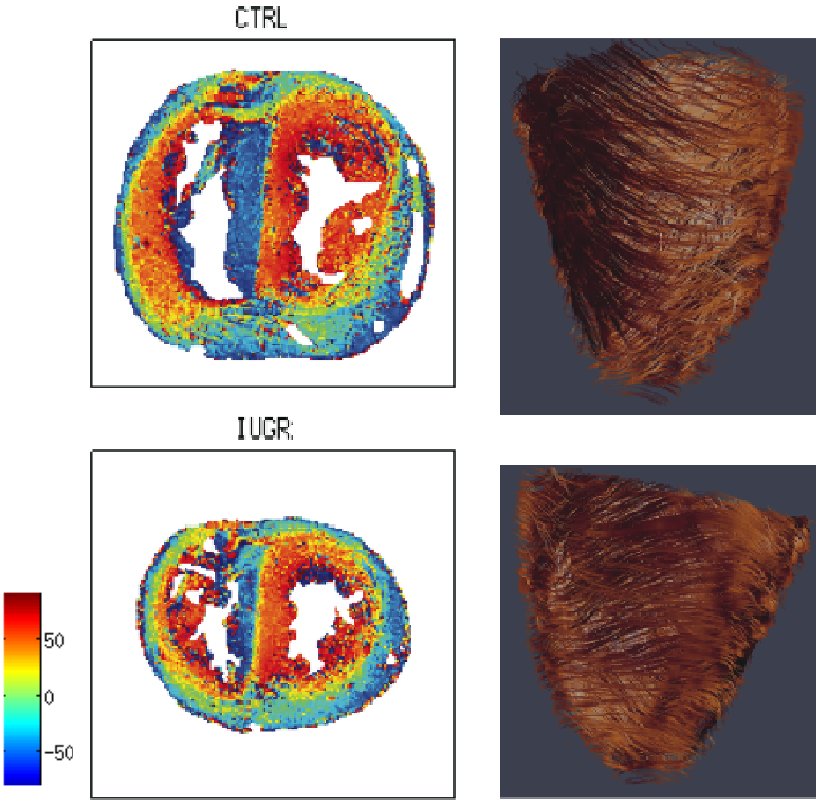

Figure 7. Fiber orientation in myocardial walls. Fiber angle change across the walls within a slice in fetal rabbit control (top left) and IUGR (bottom left) hearts. Fiber angle change from endo- to epi-cardium from +90º to -90º. A visualisation of the resulting 3D fibre structure at the right.

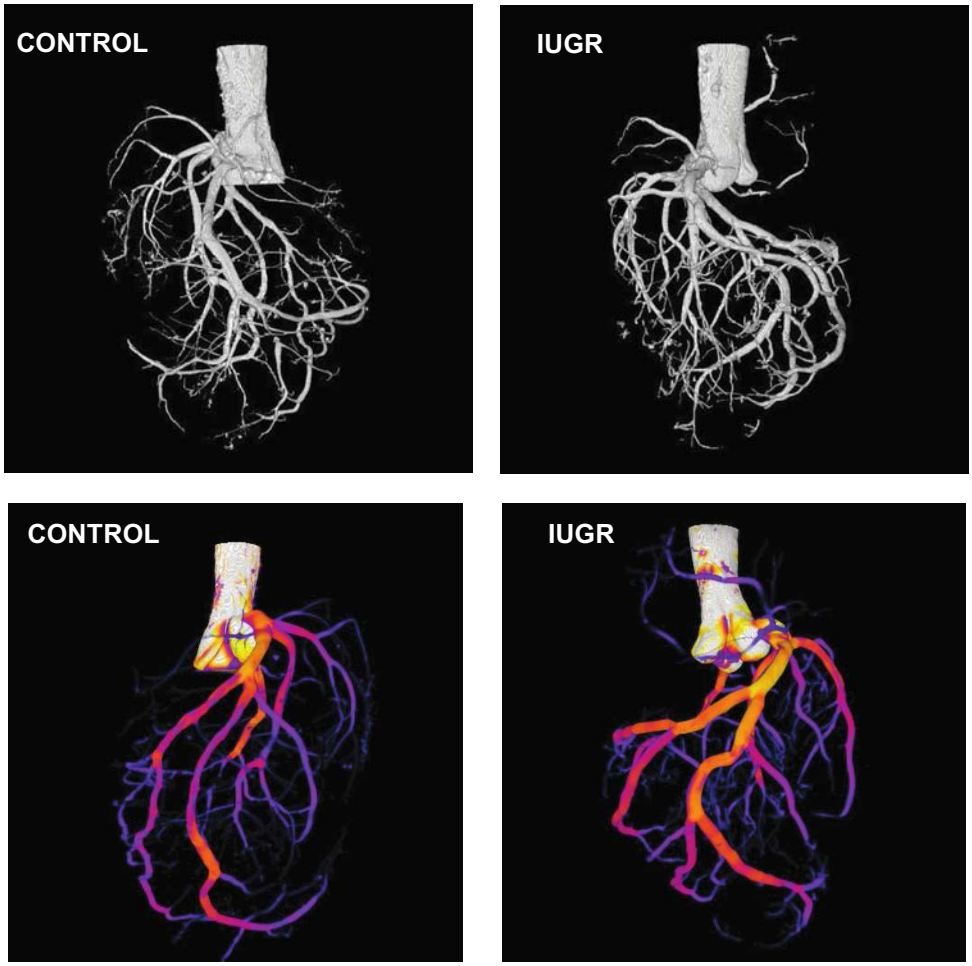

Figure 8. Segmentation of the coronary vascular tree. Coronary vascular tree can be clearly visualized when segmented (top). The differences between control and IUGR rabbit fetal hearts result even more evident when the segmentation of the coronary vessels is visualized as a quantification of the local radius of the vessels (bottom). Lighter colours mean bigger diameters; therefore the dilatation of the coronary arteries in IUGR can be clearly observed.

6.3. Altered intracellular arrangement in IUGR cardiomyocytes (study 2)

General cardiomyocyte cyotarchitecture

The electron microscopy study showed significant differences between IUGR and control fetal rabbit myocardium regarding the arrangement of the intracellular components. A representative image of this is displayed in Figure 9A-B, showing that IUGR rabbits present a looser packing of mitochondria and an increased cytosolic space between mitochondria and myofilaments. Quantification of the volume densities of myofilaments, mitochondria and cytoplasm is shown in Figure 9C. Stereological examination of micrographs obtained from control and IUGR myocardium showed that the amount of myofilaments was not different

between control and IUGR rabbits (mean 34.64 ± SD 4.04% in control *vs*. 34.74 ± 6.01% in IUGR, p=0.973). On the other hand, changes in the relative volume occupied by mitochondria and cytoplasm were observed among control and IUGR myocardium. The relative volume occupied by mitochondria was significantly decreased in IUGR fetuses (34.59 ± 4.23% in control *vs.* 27.74 ± 5.28% in IUGR, p=0.032), while the relative volume occupied by total cytoplasm was significantly increased under IUGR (30.77 ± 3.04% in control *vs.* 37.53 ± 4.97% in IUGR, p=0.018). In this study we classified the cytoplasm into two categories according to its localization: i) cytoplasm located between mitochondria and myofilaments (ICEUs) and ii) cytoplasm not located in the ICEUs, namely free cytoplasm. The cytoplasm existing within ICEUs was significantly increased under IUGR (6.47 ± 0.1.18% in control *vs.* 8.69 ± 1.75% in IUGR, p=0.027). However, the free cytoplasm was not altered (24.31 ± 2.91% in control *vs.* 28.84 ± 5.27 % in IUGR, p=0.095).

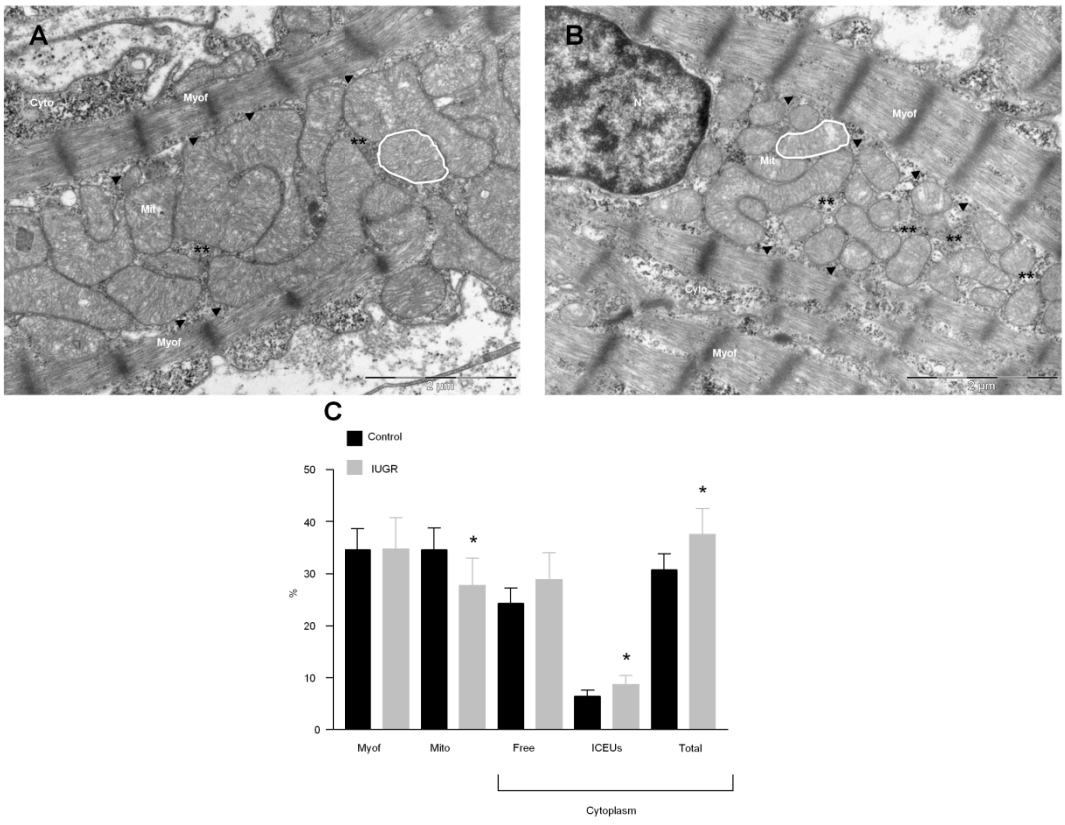

Figure 9. Cytoarchitectural organization of cardiomyocytes. Representative micrographs showing the typical organization of the intracellular space in control (**A**) and IUGR (**B**) fetal cardiomyocytes. While mitochondria are highly compacted and packed close to myofilaments in controls, they are looser packed showing an increased cytosolic space both within the mitochondrial network (**) and between mitochondria and myofilaments (arrow heads) in IUGR. **C**, stereological measurements of fetal control and IUGR cardiomyocytes showing the relative volume occupied by myofilaments, mitochondria, free cytoplasm (Free), cytoplasm between mitochondria and myofilaments (ICEUs) and total cytoplasm (Total). *p<0.05. Data in graphs are expressed as mean ± SD. Magnification: 20000x. Scale bar=2 μm. Mit (mitochondria), Myof (myofilaments), Cyto (cytoplasm), N (nucleus).

Mitochondrial area and number

The average area of individual mitochondria as well as the number of mitochondria were quantified in order to test whether changes in the relative volume occupied by mitochondria could be due to changes in the mitochondrial size or number (Fig 10). Results did not show statistically significant differences regarding the area of individual mitochondria (0.3094 ± 0.0595 μm^2 in control *vs.* 0.2407 ± 0.0176 μm^2 in IUGR; p=0.128). Average number of mitochondria neither resulted to be different between control and IUGR hearts (27.47 ± 9.32 in control vs. 26.33 ± 8.06 in IUGR; p=0.627).

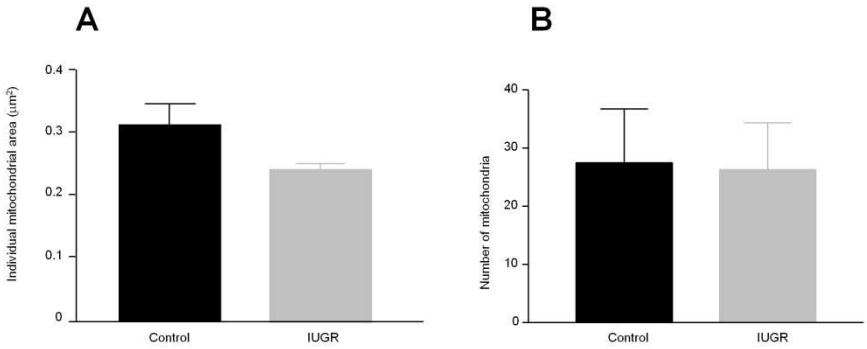

Figure 10. Mitochondria area and number. **A,** average area of individual mitochondria, estimated delineating each mitochondria as shown in Fig 3.A and B. **B**, average number of mitochondria. Data in graphs are expressed as mean ± SD.

ICEUs arrangement

Subsequently, the area and mean distance between mitochondria and myofilaments were automatically quantified (Fig 11). Results showed that both the area of cytoplasm between mitochondria and myofilaments within ICEUs (median 120700 (IQR 87490-155500) nm^2 in control *vs.* 168600 (124100-236200) nm^2 in IUGR, p=0.015) (Fig 11E) and the mean distance (105.7 (86.7-137.9) nm in control *vs.* 133.7 (104.7-182.3) nm in IUGR, p=0.037) (Fig 11F) were significantly increased in IUGR rabbit myocardium.

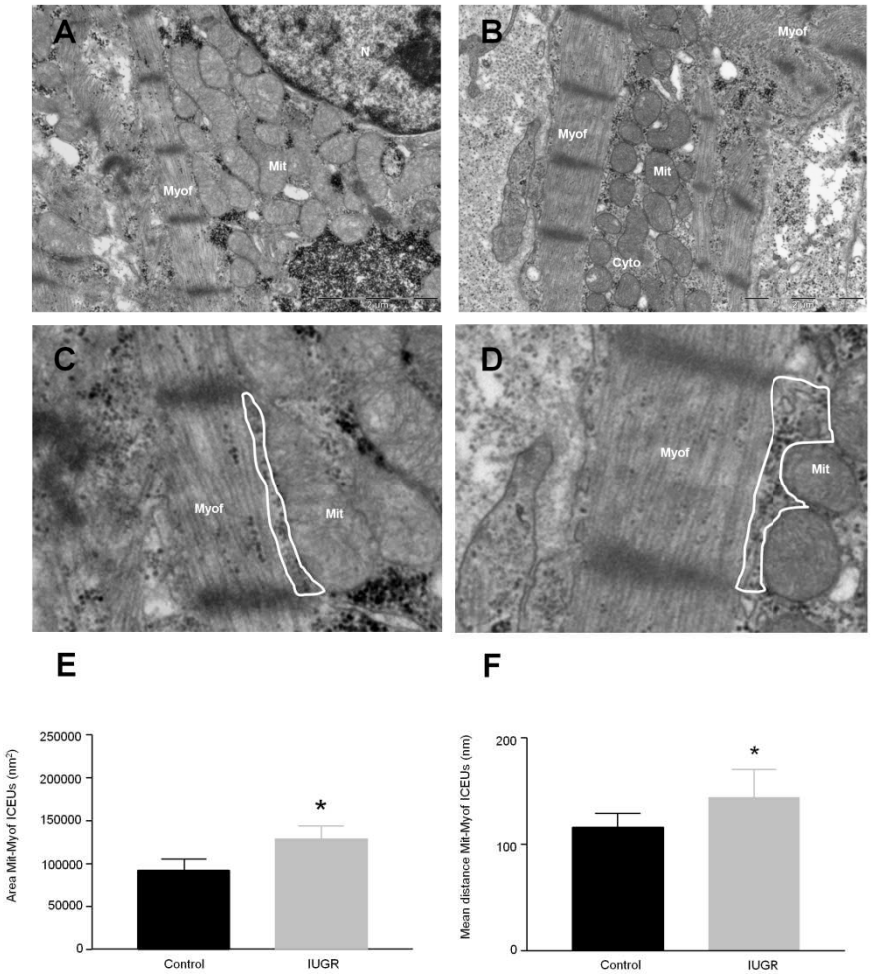

Figure 11. Arrangement of ICEUs. Representative micrographs show an overview of a mitochondrial network surrounded by myofilaments in a control (**A**) and IUGR (**B**) fetal cardiomyocyte. **C** (control) and **D** (IUGR) are a detail of **A** and **B**, respectively, showing delineated ICEUs. Although in control myocardium mitochondria are closely apposed to myofilaments, the cytoplasmic space between mitochondria and myofilaments is greater in IUGR. *E* and F: quantification of the average area of cytoplasm and the mean distance between mitochondria and myofilaments within ICEUs, respectively. **P* _ 0.05. Data in graphs are expressed as means ± SD. Magnification: 20,000X. Scale bar = 2 µm. Mit, mitochondria; Myof, myofilaments; Cyto, cytoplasm; N, nucleus.

6.4. IUGR induces shorter sarcomere length in utero (study 3)

Second Harmonic Generation Microscopy of heart tissue

Evaluation of the ultrastructure of the sarcomere was performed in human fetal cardiac tisse. A representative image is displayed in of the SHG signa is shown in Figure 5. Images

show that sarcomere borders are clearly delimited by two neighbouring Z-discs, visualized as thick dark regions. The SHG signal originates from the thick myosin filaments, corresponding to the A-band. A thin black line is observed in the centre of the A-band, corresponding to the crossbridge-free portion of the thick filaments, identified as the M-band.

Quantification of SHG microscopy images showed a shorter sarcomere length in IUGR samples as compared to controls Figure 12. There were significant differences in the distance between two Z-lines delimiting one sarcomere and a trend towards a decreased distance between intrasarcomeric A-bands.

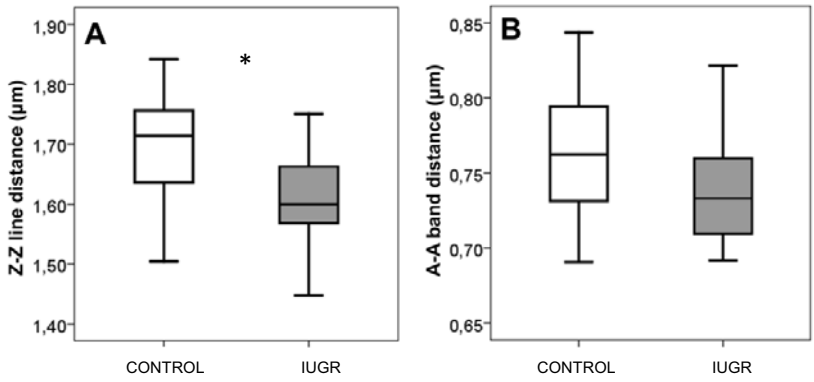

Figure 12. Sarcomere morphometry. A, Sarcomere length or Z-Z line distance and **B**, intrasarcomere (A-A band) distance in normally grown and growth-restricted fetuses.

6.5. Postnatal persistence of sarcomere changes in IUGR (studies 3 and 4)

Characterization of the sarcomere ultrastructure by measuring its lengths was as well performed in the experimental model of IUGR. The quantification of SHG microscopy images showed that as compared to controls, IUGR subjects had a shorter sarcomere length (1.658 µm ± 0.094 vs. 1.531 µm ± 0.114 in controls and IUGR respectively, p=0.042) (Fig 13B). Intra-sarcomeric A-band length was also found to be decreased by IUGR (0.772 µm ± 0.044 vs. 0.705 µm ± 0.060 in control and IUGR, respectively, p=0.035) (Fig 13C). Additionally, thick-thin filament interaction length was shorter in IUGR (0.104 µm ± 0.006 vs. 0.096 µm ± 0.007 in control and IUGR, respectively. P=0.048) (Fig 13D). The ratio between sarcomere length and intrasarcomeric A-band length was similar in the study groups (2.15 ± 0.02 vs. 2.17 ± 0.03 in control and IUGR, respectively).

Next purpose was to determine if alterations affecting sarcomere ultrastructure persist in postnatal life. Seven paired control and IUGR young adult rabbits (70 postnatal days), with similar ratios between sarcomere length and intrasarcomeric A-band length (2.11 ± 0.02 vs. 2.11 ± 0.01 in control and IUGR, respectively), were analyzed. Similar to what we found in fetal tissue, the measurements showed significant decreases in sarcomere length (1.720 μm ± 0.068 vs. 1.626 μm ± 0.084 in control and IUGR, respectively. p=0.04) and intrasarcomeric A-band length (0.817 μm ± 0.036 vs. 0.772 μm ± 0.041 in control and IUGR, respectively. p=0.049) due to IUGR (Fig 14B, C). Additionally, sarcomeric thick-thin filament interaction length was shorter in IUGR (0.103 μm ± 0.005 vs. 0.097 μm ± 0.005 in controls and IUGR, respectively. p=0.045) (Fig 14D).

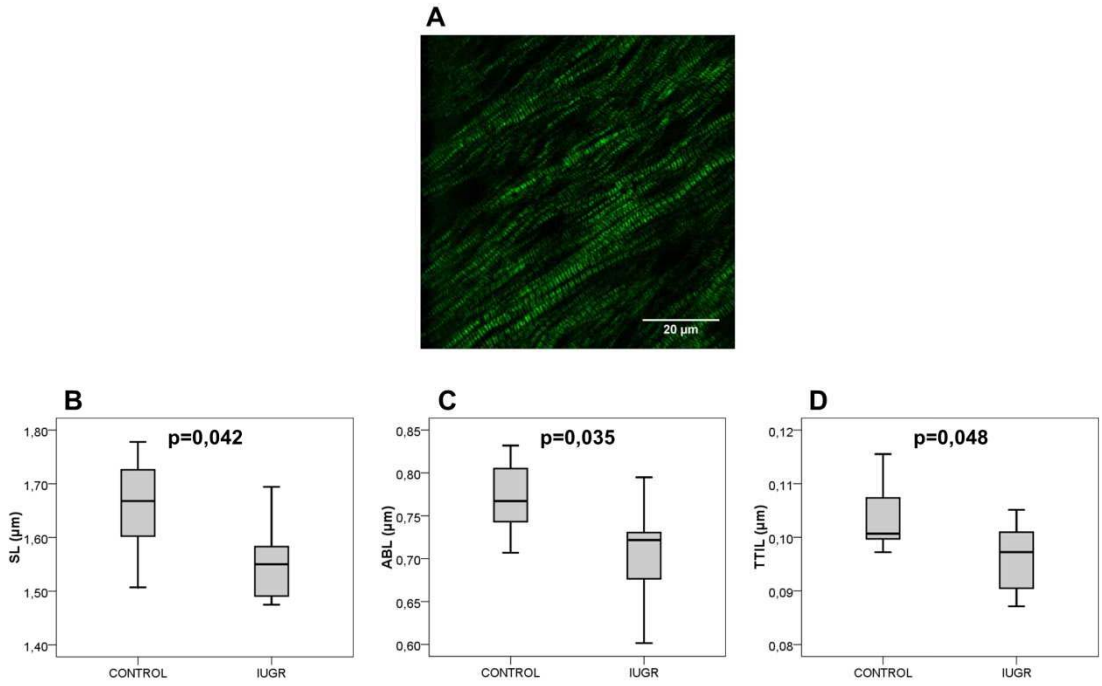

Figure 13. Ultrastructural sarcomere changes in fetal hearts from IUGR and controls. A, A representative SHGM image from unstained fetal rabbit left ventricle. The sarcomeres are clearly delimited by thick black lines (Z-discs) and the SHGM signal originates from the thick myosin filaments (in green). In the central region of the myosin filaments appears a thinner black line, identified as the M-band. Scale bar= 20 μm. **B** and **C,** show average distances between two consecutives Z-discs (SL) and intrasarcomeric A-bands (ABL), respectively. **D,** shows thick-thin filament interaction length (TTIL), as the mean width of the A-band-related peaks. Data are expressed as mean ± SD.

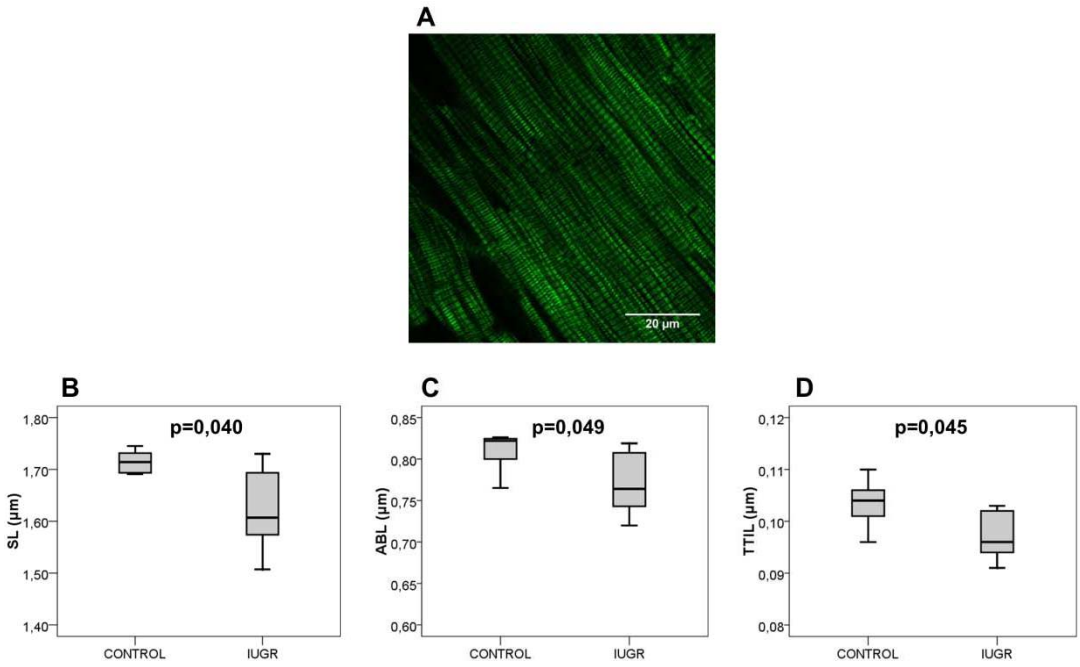

Figure 14. Ultrastructural sarcomere changes in adult hearts from IUGR and controls. A, Representative SHGM image from unstained adult rabbit left ventricle. Scale bar= 20 µm. **B** and **C,** show average distances between two consecutive Z discs (SL) and two intrasarcomeric A bands (ABL), respectively. **D,** shows thick-thin filament interaction length (TTIL). Data are expressed as mean ± SD.

6.6. Ultrastructural changes in IUGR are associated with cardiac functional changes (studies 2, 3 and 4)

Human IUGR fetuses show signs of cardiac dysfunction

In order to assess the potential association of the described structural changes with an abnormal cardiac function, we aimed to evaluate cardiac function in both study populations studied in this thesis.

On one hand, echocardiographic evaluation of human fetuses (Table 4) shows that IUGR fetuses presented signs of global cardiac dysfunction and diastolic dysfunction, denoted by increased DV PI, MPI and E/A ratios.

On the other hand, fetal blood cardiovascular biomarkers (Table 4) detection showed an increase of B-type natriuretic peptide and a non-significant trend to higher values of TnI in IUGR compared to controls.

Table 4. Ultrasound and fetal blood cardiovascular markers in control and IUGR human fetuses.

	Control	IUGR	*P-value*
Echocardiographic indices			
Ductus venosus pulsatility index (z-scores)	0 (0.7)	6.7 (7.3)	*0.014**
Isovolumic contraction time (z-scores)	0.1 (0.8)	0.5 (2)	*0.089*
Ejection time (z-scores)	0 (0.7)	-1.2 (3.1)	*0.056*
Isovolumic relaxation time (z-scores)	0.2 (1)	3.9 (4.3)	*0.032**
Left myocardial performance index (z-scores)	-0.1 (1)	4.7 (6.5)	*0.044**
Left E/A (z-scores)	0.1 (0.2)	2.3 (2.7)	*0.027**
Right E/A (z-scores)	-0.1 (0.9)	5.2 (8.5)	*0.011**
Fetal blood biomarkers			
B-type natriuretic peptide (pg/mL)	65 (48)	340 (538)	*0.004**
Troponin-I (ng/mL)	0.02 (0.02)	0.08 (0.60)	*0.069*

Data are median (interquartile range). * p- value < 0.05

The experimental model reproduces cardiac dysfunction of human IUGR

Echocardiographic evaluation to assess cardiac morphometry and function in the experimental model of IUGR, detailed in Table 5, shows that IUGR hearts are more globular with lower sphericity index (significantly different for the right ventricle, borderline for the left) but similar wall thickness compared to controls. Despite similar results in ejection fraction, mitral annular peak velocities (S') were significantly lower in IUGR as compared to controls, denoting a systolic dysfunction. Additionally, DVPI and AoIPI were significantly increased in IUGR fetuses.

Table 5. Fetal echocardiographic results in the experimental model of IUGR.

	Control	IUGR	P-value
N	10	10	
Fetal hemodynamics			
Ductus venosus pulsatility index	0.75 (0.25)	1.33 (0.75)	0.008 *
Aortic isthmus pulsatility index	3.05 (0.45)	3.85 (1.16)	0.009 *
Cardiac morphometry			
Left sphericity index	1.54 (0.34)	1.51 (0.26)	0.073
Right sphericity index	1.56 (0.24)	1.32 (0.23)	0.004 *
Left ventricle wall thickness (mm)	1.45 (0.37)	1.41 (0.31)	0.978
Systolic function			
Left ejection fraction (%)	89.1 (8.2)	82 (24.6)	0.390
Mitral annular systolic peak velocity (cm/s)	1.91 (0.27)	1.59 (0.33)	0.046 *

Data are median (interquartile range). * p- value < 0.05

IUGR induces changes in the expression of functional groups of genes

In order to complement the structural results showing changes induced by IUGR in the experimental model, we performed a gene expression study in order to detect potential genes with differential expression that could be responsible for the observed changes.

Gene expression microarrays output was analyzed from two viewpoints:

Differential gene expression: Analysing for a fold change higher than 0.5 and an adjusted p-value lower than 0.05, there were not genes with significant differential expression.

Gene set analysis: The output result of the differential expression analysis (ranked list by the statistic of the test) was the input for the gene set analysis. On this full list of genes, Fatiscan detected groups of genes with the same expression pattern and sharing biological functions and extracted significantly under- and over-represented Gene Ontology terms in a set of genes after comparing two sub-lists of genes with different pattern of expression: the first list included genes more expressed in IUGR group and the second list with genes more expressed in control group. Therefore, this analysis evaluated both the IUGR group and control group at the same time. Gene set analysis showed that IUGR subjects presented a statistically significant enrichment in groups of genes involved in energy production, cardiac energetic metabolism regulation and the sarcomere M-band (Table 6). Oxidative phosphorylation annotation (GO: 0006119, biological process) was found in 1.03% of the most up-regulated genes in IUGR (list 1, more expressed in IUGR than control group), while only 0.17% of the most down-regulated genes in IUGR contained the annotation (list 2, more expressed in control than IUGR group). Similarly, the annotations for oxygen homeostasis (GO: 0032364, biological process), mitochondrial respiratory chain complex I (GO: 0005747, cellular component) and NADH dehydrogenase (GO: 0003954, molecular function) were found in 0.49%, 0.44% and 0.35% respectively, of the most up-regulated genes in IUGR, and only in 0.04%, 0% and 0% of the most down-regulated genes in IUGR, respectively. All p-values were ≤ 0.001 and all adjusted p-values were < 0.08. In relation to the sarcomere, gene set analysis detected an enrichment of the M-band annotation (GO: 0031430, cellular component), which was found in 1.6% of the most up-regulated genes in IUGR, while only 0.69% of the most down-regulated genes in IUGR contained the annotation (Table 6). All p-values were ≤ 0.001 and all adjusted p-values were < 0.08.

Table 6. Gene set analysis with FatiScan.

Annotation	Up-represented in IUGR	Down-represented in IUGR	p-value	adj. p-value	GO type
Oxidative phosphorylation (GO: 0006119)	1.03%	0.17%	1.15e-4	7.87e-2 *	Biological process
Oxygen homeostasis (GO: 0032364)	0.49%	0.04%	1.63e-4	7.82e-2 *	Biological process
Mitochondrial respiratory chain complex I (GO: 0005747)	0.44%	0%	1.39e-3	7.29e-2 *	Cellular component
NADH dehydrogenase (GO: 0003954)	0.35%	0%	4.37e-4	6.03e-2 *	Molecular function
M band (GO: 0031430)	1.6%	0.69%	8.79 e-4	6.91 e-2	Cellular Component

Gene Ontology annotations involved in energy production and cardiac energetic metabolism regulation with a statistically significant enrichment in IUGR. * adjusted p-value < 0.08.

7. DISCUSSION

7. DISCUSSION

This thesis consists on a multiscale characterization of cardiac remodeling induced by IUGR, mainly focusing on the structure. Overall, this thesis provides evidence that IUGR induces cardiac remodeling affecting the organ as a whole, the cardiomyocyte as well as specific organelles like the sarcomere. Cardiac remodeling in IUGR has been studied, but it still remains poorly understood. This thesis provides information to improve current understanding of the pathophisiology of cardiac remodeling and dysfunction induced by IUGR.

Two different study populations have been used in this thesis to characterize cardiac remodeling in IUGR. On the one hand, a human population of fetuses that died in utero due to maternal complications of pregnancy or during the perinatal period (study 3); and on the other hand, an experimental model in New Zealand rabbit that reproduces main biometric and cardiovascular dysfunction features of human IUGR (studies 1, 2 and 4).

The experimental model used in this study to reproduce IUGR is based on the selective ligature of the uteroplacental vessels in pregnant rabbit at 25 days of gestation until 30 days of gestation and it has been previously validated by our research group [101,102]. The model mimics IUGR in human pregnancy, since it induces a combined restriction of oxygen and nutrients, taking into account the role of the placenta [101,102]. Different gestational ages as well as different degrees of ligature severity were previously tested for this experimental IUGR model, concluding that the condition that best reproduced human IUGR due to placental insufficiency is the selective ligature of the 40-50% of the uteroplacental vessels at 25 days of gestation [101]. It is known that in rabbits, complete organogenesis is achieved at 19.5 days of gestation [124]. The two previous statements together with the aim to reproduce late IUGR occurring in the third trimester of human pregnancy (which is mainly caused by placental and maternal vascular factors), lead to the rationale of the ligature from 25 to 30 days of gestation [101,125]. The severity of the experimental IUGR model reproducing human IUGR condition due to placental insufficiency, with regard to mortality rate and hemodynamic changes has been previously described [101,102]. Signs of placental insufficiency are observed in ultrasound assessment. Biometric changes induced by the selective ligature of 40-50% of the uteroplacental vessels result, as expected, in lower birth and heart weights, as well as decreased crown-rump length and abdominal girth. Additionally, an increase in heart to body weight is denoted in IUGR, which could be

interpreted as a hypertrophic compensatory mechanism and is consistent with previous studies from experimental models of severe IUGR [44,126,42].

Our **first study** demonstrates a remodelling of the heart at the whole organ level due to IUGR. We used a novel imaging technique whose main strengths are that provides a high resolution and does not require complicated processing. This enables to study the micro-architecture of the fetal heart, which is challenging otherwise. Additionally, we have shown that the integrated assessment of organ morphology, vasculature and fibre structure provides a way to quantify subtle (sub-clinical) remodelling induced in-utero. We have observed, as expected, that IUGR fetal rabbit hearts are smaller and with thinner ventricular walls compared to controls, as it has been previously observed in other models of intrauterine hypoxia [5]. Interestingly, results show a change in fiber orientation in IUGR pointing towards an alteration of its transmural course. This is consistent with a previous study which described that fiber orientation is sensitive to changes in mechanical loading [56], which are believed to occur in IUGR. Since cardiac function depends on cardiac movements that are determined by the complex three-dimensional organization of the fibers within the cardiac walls, it could be hypothesized that the change in fiber orientation might be responsible for the cardiac dysfunction in IUGR. However, results are still preliminary and more data is needed to be able to make the associaton between structure and function. While whole IUGR heart is smaller, the coronary arteries are clearly dilated, most probably due to the haemodynamic challenge induced by hypoxia and hyponutricia in IUGR, as it has been previously described [45].
It is worthy to mention that the technique used in this study allows fast imaging of whole hearts to quantitatively describe and compare morphological remodelling of all substructures within the different components of the heart. Obtained datasets provide a unique source of information where tissue properties can be quantified and compared within the 3D structure for purposes of describing changes induced by disease, even if the remodelling present is subtle and not detectible by current imaging modalities.

In **study 2** we aimed to study cardiomyocyte intracellular organization in the experimental model and we show that IUGR is associated with a less organized intracellular arrangement of the cardiomyocyte organelles. The specific disarrangement of the ICEUs is strongly related to the differences in the gene expression of key pathways for energy production. Together, study 2 suggests an impairment of the energetic metabolism under IUGR.

The stereological estimation of the volume densities of the different cellular components evidences that IUGR fetal hearts show a less organized intracellular arrangement, characterized by an increased relative volume occupied by cytoplasm and a decreased relative volume occupied by mitochondria. These changes under IUGR could be either due to alterations on cardiac development, hypoxia or to loading changes caused by pressure or volume overload [5,30]. It has been shown that experimentally induced pressure overload results in a depression of mitochondrial respiratory capacity together with a reduction of total mitochondrial volume density [127]. Our observations of a decrease on mitochondrial relative volume in IUGR are in line with the observations from Schwarzer et al. [127]. Additionally, in the same study [127], they relate a decrease in mitochondrial density with a decrease in mitochondrial size, since the citrate synthase activity is decreased in pressure overload but the mitochondrial number is not. We do not observe changes on the number or in the area of individual mitochondria. Since the stereological study shows a decreased relative volume occupied by mitochondria, we hypothesize that smaller mitochondrial size could be the reason for the decreased mitochondrial density (similar to what was described in pressure overloaded hearts [127]), despite the lack of significance, which might be attributed to sample size restrictions. The decrease in mitochondrial density but with no changes in myofibrillar content has also been observed in fetal sheep subjected to high altitude hypoxia, which is in agreement with an alteration caused by the lack of oxygen during intrauterine life [128].

Concerning the relative volume occupied by cytoplasm, we observe that the total relative density of cytoplasm is increased in IUGR, however, when classifying it into free cytoplasm or cytoplasm within ICEUs, the former is not significantly increased while the later is significantly increased in IUGR hearts. We show that both the area of cytoplasm and the mean distance between mitochondria and myofilaments within ICEUs are increased in IUGR myocardium. In fetal heart, energy transfer is believed to rely on the direct ATP and ADP channeling between organelles since the CK-bound (creatine kinase) system is not mature [66]. Its efficiency mostly depends on the close interaction between mitochondria and myofilaments [67]. In this regard, it has been reported that intracellular disorganization restricts ATP and ADP diffusion, decreasing the efficiency of energy transfer (5). Since ICEUs play a central role in maintaining cardiac energetic homeostasis, alterations on their structure could alter the energy production, utilization and transfer, and as a consequence, cardiac function could be compromised [73]. Based on previous studies, this study suggest that ICEUs abnormal arrangement could contribute to the development of less efficient

hearts in IUGR, maybe due to a decrease on the energy transfer efficiency from mitochondria to the main cardiac ATPases. Such compromise of cardiac function due to alterations on ICEUs has been previously evidenced in heart failure [67]. The abnormal ICEUs arrangement in IUGR could also be interpreted as a maturation delay, as it has been described that during cardiac maturation there are major changes on the cardiomyocyte intracellular organization in which mitochondria get closer to myofilaments to form the ICEUs [65].

Therefore, from one side findings from this study have a close similarity to those previously described in experimentally induced pressure overload cardiac dysfunction [127,129]. On the other side, it has been described that cytoarchitectural perturbations can lead to energetic alterations, and conversely perturbations of cellular energetic metabolism can lead to ultrastructural remodeling [69]. In our study, it remains uncertain whether the structural changes could contribute to be a cause or a consequence of the cardiac dysfunction previously documented in IUGR.

Subsequently, we wanted to evaluate whether these structural changes are related to changes on gene expression. There were not individual genes with significant differential expression. The analysis identified key gene pathways related to cardiac energy production which were altered under IUGR. These included: oxygen homeostasis (GO: 0032364), oxidative phosphorylation (GO: 0006119), mitochondrial respiratory chain complex I (GO: 0005747) and NADH dehydrogenase activity (GO: 0003954). On one hand, alterations on the oxygen homeostasis and oxidative phosphorylation suggest that IUGR hearts are suffering from hypoxia. Previous studies have shown a 20-35% decrease in the oxidative phosphorylation in skeletal muscle from IUGR rats, leading to a decrease in ATP production and thus an impairment of muscle function [130]. Additionally, exposure to chronic hypoxia has been related to a decrease in cardiac oxidative capacity, which leads to a decline in ATP synthesis and in oxygen consumption [77]. Hypoxia during early life has also been associated to persistent changes in genes linked to the regulation of cardiac metabolic processes that remain present long after the termination of the neonatal hypoxic insult [131]. This may eventually be linked to the cardiovascular programming due to IUGR and the long term persistence of the changes. On the other hand, alterations on the expression of mitochondrial respiratory chain complex I and specifically on the NADH dehydrogenase activity are again in line with the study of Schwarzer *et al.* in pressure overload, in which they observe decreased function of the mitochondrial respiratory chain complex I. Our

observations are also consistent with other studies in human IUGR in which a deficiency of the mitochondrial respiratory chain complex I has been observed [132].
In conclusion this study shows that hearts from IUGR fetuses present a less organized intracellular arrangement of the cardiomyocyte organelles. These structural changes are accompanied with differences in the expression of groups of genes related to energy production and oxygen homeostasis. Overall, this study suggests that energetic metabolism is impaired in IUGR.

The **third study**, based on human fetal samples, provides evidence that IUGR is associated with cardiac dysfunction and morphometric changes in the form of shorter sarcomere length. IUGR fetuses showed signs of severe hemodynamic deterioration and cardiac dysfunction by echocardiography and the presence of B-type natriuretic peptide in cord blood. This finding was expected as all cases were early onset severe IUGR fetuses and it is consistent with previous studies demonstrating cardiac dysfunction in IUGR which correlates linearly with the degree of fetal deterioration [133,134,135,27]. Increased B-type natriuretic peptide production may result from increased volume overload and/or by direct effect of hypoxia [27,134,135]. Additionally, IUGR fetuses showed a non-significant trend to increased values of troponin-I which is also in line with previous studies demonstrating signs of myocardial cell damage in IUGR [27]. An increase in heart to body weight was also denoted in IUGR which could be explained as a compensatory mechanism and is consistent with previous data from experimental models of severe IUGR [126,44,42] and with our experimental model of IUGR.

The striking finding of this study was the observation of shorter sarcomere length in IUGR fetuses compared with control fetuses. The sarcomere is a key element for heart contractility, thus abnormalities of the sarcomere might have an impact on global cardiac function. Sarcomere length and [Ca^{2+}] are involved in myofilament force generation by different mechanisms. While [Ca^{2+}] has an effect on cross-bridge kinetics, sarcomere length has an effect on actin-myosin cross-bridge recruitment [136]. In this regard, sarcomere length is associated with the degree of thick-thin filament overlap, which affects the probability of actin-myosin cross-bridge formation and thus the capacity to generate force [137].

The main aim of our **fourth study** was to evaluate the postnatal persistence of the structural changes affecting the sarcomere described in the human population. Since the

availability of post-mortem cardiac samples of children or adults that were born with IUGR is extremely remote, we translated this study to our experimental model of IUGR. Firstly, we evaluated sarcomere morpometry in rabbit fetuses at 30 days of gestation using the same SHG microscopy technique and image processing methodology that we used for human samples. Before that, fetal cardiac function was evaluated, and confirmed that IUGR hearts are more globular, and present signs of systolic longitudinal dysfunction, which is similar to changes observed in human fetuses and children [26,27,36] and in the human population evaluated in this study. SHG microscopy results showed that sarcomere length was shorter in IUGR, consisitent with the results from the third study; and additionally it was accompanied by a decrease in A-band length and thick-thin filament interaction length. Subsequently the same approach was applied to young adult rabbits and results were the same. The shorter sarcomere length and thick-thin filament interaction length might indicate a decrease in the number of binding events for cross-bridges between actin and myosin. Since cardiac muscle energy consumption is dependent on the number of recruited cross-bridges [138] a shorter sarcomere uses less energy contracting over a smaller distance which allows the heart to be operative under energy restriction conditions [138,139]. As a trade off, shorter sarcomeres lose force and stability in unfavourable working conditions [79,139] . Therefore, shorter sarcomeres in IUGR might reflect an adaptive mechanism to cope with chronic oxygen and nutrient restriction. This would allow increased efficiency through lower energy consumption but result in reduced contractile function. Therefore changes observed in sarcomere length are consistent with reduced longitudinal systolic function and stroke volume observed in IUGR fetuses and children [27,36]. Shorter sarcomeres have been found in animal models of a variety of cardiac diseases, diastolic cardiomyopathy [87], and dilated cardiomyopathy and heart failure [88]. Additionally, in a recent paper using human biopsies, passive force-length analysis suggested a shorter sarcomere length in pressure-overloaded myocardium compared to volume overload and control donors [113]. The observed changes in sarcomere length are consistent with previous research where it was shown that chronic prenatal hypoxia led to a shift in the expression of titin isoform N2BA (the larger, more compliant isoform) towards isoform N2B (the smaller, stiffer isoform) [5]. This protein extends from the center of the sarcomere to the *Z* line, thus acting as a developmental template for sarcomere assembly [140]. Titin is thought to be a major determinant of the sarcomere length [141,87].

The consistency of the existence of the same structural change in IUGR humans, IUGR rabbit fetuses and relevantly, the postnatal persistence in IUGR young adult rabbits,

strengthens the hypothesis that changes in sarcomere length could help to explain subclinical cardiac dysfunction associated with IUGR [36]. The permanent changes in sarcomere structure could be as well a response to the known sustained increase in fetal blood pressure that occurs in IUGR. Supporting this notion, recent findings suggest that isolated neonatal cardiomyocytes undergo structural modifications within their myofibrils in response to changes in environmental stiffness, resulting in differences in resting sarcomere length [142].

Gene expression set analysis demonstrated functional differences in a basic structure for the sarcomeric cytoskeleton, the M-band, which plays an important organizational role during myofibrillogenesis by performing the regular packing of the nascent thick (myosin) filaments [79]. This finding is in line with previous observations suggesting that specific structural alterations at the level of the M-band might be part of a general adaptation of the sarcomeric cytoskeleton to unfavorable working conditions in early stages of dilated cardiomyopathy, correlating with an impaired ventricular function [143]. Moreover, they suggest an underlying basis for the abnormal sarcomere cytoarchitecture observed in IUGR. Genes included in the M-band functional class involve a variety of associated molecules to this structure with key roles in sarcomere assembly and function, including titin, obscurin and myomesin. These findings deserve further investigation to clarify the involvement of critical proteins for sarcomere structure and function, such as titin, myosin and myosin binding protein C, which have been previously described to be abnormal in IUGR [5,44] and in inherited and acquired cardiomyopathies [144,145].

In conclusion, abnormal cardiac function observed in IUGR fetuses is associated with permanent morphometric changes at sarcomere level. These changes could represent part of the fetal adaptive response to the adverse environment of IUGR. Further characterization of the sarcomere components and the molecules involved in their regulation is warranted to better understand their involvement in cardiac dysfunction in IUGR.

IUGR is believed to induce a combination of hypoxia, pressure and volume overload. All of them are considered insults for the heart. Signs of fetal hypoxia are demonstrated by an increased pulsatility in aortic isthmus flow as a reflection of the shift of blood towards the brain circulation in response to hypoxia, which is produced by a combination of brain vasodilation and systemic hypertension [146]. An increase in ductus venosus pulsatility index, due to the brain sparing effect in order to provide blood to vital organs under hypoxic conditions, increases the venous return causing a volume overload condition to the heart.

Increased placental resistance may lead to a pressure overload condition of the heart. Therefore the heart from the IUGR fetus has to deal with these three insults, adapt according to them in order to maintain cardiac function and continue with the cardiac maturation. These adaptations might favour the fetus under the adverse intrauterine environment; however, the long-term consequences of these adaptations could have a significant impact on cardiovascular health later in life. During development and adult life, the heart has to deal with other type of insults (hypertension, coronary artery disease, ischemia, etc), when it occurs, the IUGR hearts which remodeled during intrauterine life and are different compared to normal hearts, might not be able to cope with these insults, thus increasing the risk of cardiovascular disease.

The structural changes described in this thesis support the hypothesis that hypoxia, pressure and volume overload have a role in IUGR cardiac remodelling and additionally affect the organ, the cell and the subcelluar level. Furthermore, these changes are accompanied by signs of cardiac dysfunction. Changes described are intimately related. Sarcomeres are shorter, however the relative amount of myofilaments is not altered in IUGR cardiomyocytes, which could bring up the idea that IUGR cardiomyocytes synthetize more sarcomeres per myofiber, but shorter. There is a higher amoung of cytoplasm and lesser amount of mitochondria, however, it still not clear if the size of control and IUGR cardiomyocytes is the same. Although IUGR hearts seem to be hypertrophic, we still have not elucidated if hearts are actually hypertrophic because cardiomyocytes are hypertrophic, because there is a higher amount of extracellular matrix or because the total number of cardiomyocytes is higher. This issue will be evaluated in future studies and will give a strong clue towards understanding cardiac programming in IUGR, because after birth, hearts have a reduced capacity to proliferate an repairing after injury.

Limitations

Several study limitations and technical considerations should be mentioned. The bioinformatics gene set analysis used in studies two and four, is useful for studying diseases in which subtle differences are expected to occur, like in IUGR. Therefore, rather than expression changes on individual genes, alterations are expected to occur at the level of biological pathways and functionally related groups of genes. IUGR is thought to be a multifactorial disease in which several pathways and multiple members of a pathway might

be involved, resulting in only subclinical changes. However, we acknowledge that is difficult to address the actual biological relevance of the gene expression findings. Future functional studies are required to relate the gene expression changes to functional alterations at the cellular level. However, this goal lies beyond the scope of the present studies and will be investigated in future research.

Regarding the study evaluating human fetuses (study 3), the limited sample size has probably prevented to demonstrate statistically significant changes in the A-A band length and troponin-I concentrations. Moreover, we acknowledge that differences on perinatal outcome (mainly spontaneous versus elective termination of pregnancy), blood sampling and body size could have interfered in the results. However, results were adjusted by fetal size and the study populations showed a similar gestational age and percentage of cardiac arrest with potassium chloride. It could be thought that sarcomere length differences in both studies could be attributed to differences in cardiac arrest on systole or diastole. We acknowledge that such differences have been described [50], however in our human study a similar proportion of subjects received potassium chloride to arrest the heart in diastole, and cases that were not arrested in diastole might have an ultrastructure closer to diastole than systole, since a delay in fixation due to fixative penetration into the tissue allows sarcomeres to begin to relax [50]. Regarding the animal model, sampling was performed under the same conditions for all subjects. On the other hand, concerning the SHG microscopy technique, it is worthy to mention that this technique has been validated to accurately visualize the SHG signal produced by cardiac myosin thick filaments in unstained sarcomeres from different species with an accuracy of 20 nm [84,95,111]. SHG offers comparable results to those provided by electron microscopy with the additional advantage of imaging larger tissue areas [111]. Sarcomere length values in this study were consistent with measurements using electron and light microscopy in fixed rabbit cardiomyocytes, and showed increasing values with cardiac maturation [62].

Concluding remarks

The relevance of this thesis relies on the description of signs of cardiac remodeling due to IUGR at all levels, from the whole cardiac architecture, through cardiomyocyte architecture, to the ultrastructure of the sarcomere. Moreover, the structural changes are associated with cardiac dysfunction and gene expression alterations. The characterization

of this remodeling might help to better understand the pathophysiological mechanisms underlying cardiac dysfunction in IUGR. This Thesis opens novel research lines aiming to clarify the molecular mechanisms underlying cardiac adaptation and remodeling in IUGR. A better understanding of these mechanisms is critical for identifying biomarkers and developing potential therapeutic strategies for improving cardiovascular health in these children. Given the high prevalence of IUGR (up to 7-10% of all pregnancies), the clinical relevance and potential effect of any preventive strategy may have a strong impact in public health.

In addition, novel imaging techniques such as X-ray phase contrast and second harmonic generation have been used in this Thesis, which could also have a potential application in understanding other cardiac diseases and open up new possibilities for a systems approach towards cardiac function.

Finally, this Thesis has also permited to adapt and validate some of these techniques for studying the fetal heart which is particularly challenging due to its size and limited access *in utero*. Developing tools for prenatal assessment is critical for future studies aiming to understand normal organ development and generation of disease from the earliest stages of life.

Altogether, this Thesis represents a step forward towards the deep understanding of cardiac remodeling and dysfunction in IUGR, identifying several mechanistical targets for future studies. The development, integration and validation of several high-resolution imaging techniques for the fetal heart may also contribute and extent this knowledge to other fetal conditions that could program the cardiovascular system from the earliest stages of life.

8. CONCLUSIONS

8. CONCLUSIONS

1. The detailed cardiac anatomy is different in IUGR hearts, with changes in fiber orientation and coronary vessels dilatation.

2. The arrangement of intracellular organelles of the cardiomyocyte is altered in IUGR fetuses, mainly affecting mitochondria and their interaction with myofilaments.

3. Sarcomere length is shorter in IUGR fetuses, which could result in decreased contractility.

4. Shorter sarcomere length persists in postnatal life, suggesting that IUGR-induced changes on sarcomere morphometry during fetal life could contribute to the increased risk of cardiovascular disease in adulthood.

5. The described signs of cardiac remodelling are associated with subclinical cardiac dysfunction in IUGR fetuses and changes in the expression of groups of genes involved in oxygen homeostasis, energy production and the sarcomere M-band.

9. REFERENCES

9. REFERENCES

1 Barker DJ, Osmond C, Golding J, Kuh D, Wadsworth ME. Growth in utero, blood pressure in childhood and adult life, and mortality from cardiovascular disease. *BMJ*, 298 (1989), 564-567.

2 Phillps D. Insulin resistance as a programmed response to fetal undernutrition. *Diabetologia*, 39 (1996), 1119-1122.

3 Gluckman PD, Hanson MA, Cooper C, Thornburg KL. Effect of in utero and early-life conditions on adult health and disease. *N Engl J Med*, 359 (2008), 61-73.

4 Palinski W, Napoli C. Impaired fetal growth, cardiovascular disease, and the need to move on. *Circulation*, 117 (2008), 341-343.

5 Tintu A, Rouwet E, Verlohren S, Brinkmann J, Ahmad S, Crispi F, van Bilsen M, Carmeliet P, Staff AC, Tjwa M, Cetin I, Gratacos E, Hernandez-Andrade E, Hofstra L, Jacobs M, Lamers WH, Morano I, Safak E, Ahmed A, le Noble F. Hypoxia induces dilated cardiomyopathy in the chick embryo: mechanism, intervention, and long-term consequences. *PLoS One*, 4 (2009), e5155.

6 Alberry M, Soothill P. Management of fetal growth restriction. *Arch Dis Child Fetal Neonatal Ed*, 92 (2007), F62-67.

7 Barker DJ. The long-term outcome of retarded fetal growth. *Schweiz Med Wochenschr*, 129 (1999), 189-196.

8 Gardosi J. New definition of small for gestational age based on fetal growth potential. *Horm Res*, 65 (2006), 15-18.

9 Figueras F, Gratacós E. Update on the Diagnosis and Classification of Fetal Growth Restriction and Proposal of a Stage-Based Management Protocol. *Fetal Diagn Ther* (2014), In press.

10 Committee on Practice Bulletins Gynecology, American College of Obstetricians and Gynecologists. Intrauterine growth restriction. Clinical management guidelines for obstetrician-gynecologists. American College of Obstetricians and Gynecologists. *Int J Gynaecol Obstet*, 72 (2001), 85-96.

11 Society for Maternal-Fetal Medicine Publications Committee, Berkley E, Chauhan SP, Abuhamad A. Doppler assessment of the fetus with intrauterine growth restriction. *Am J Obstet Gynecol*, 206 (2012), 300-308.

12 Maulik D. Fetal growth compromise: definitions, standards, and classification. *Clin Obstet Gynecol*, 49 (2006), 214-218.

13 Ott WJ. Sonographic diagnosis of fetal growth restriction. *Clin Obstet Gynecol*, 49 (2006), 295-307.

14 Oros D, Figueras F, Cruz-Martinez R, Meler E, Munmany M, Gratacos E. Longitudinal changes in uterine, umbilical and fetal cerebral Doppler indices in late-onset small-for-gestational age fetuses. *Ultrasound*

Obstet Gynecol, 37 (2011), 191-195.

15 Turan OM, Turan S, Gungor S, Berg C, Moyano D, Gembruch U, Nicolaides KH, Harman CR, Baschat AA. Progression of Doppler abnormalities in intrauterine growth restriction. *Ultrasound Obstet Gynecol*, 2 (2008), 160-167.

16 Hecher K, Bilardo CM, Stigter RH, Ville Y, Hackelöer BJ, Kok HJ, Senat MV, Visser GH. Monitoring of fetuses with intrauterine growth restriction: a longitudinal study. *Ultrasound Obstet Gynecol*, 18 (2001), 564-570.

17 Demicheva E, Crispi F. Long-Term Follow-Up of Intrauterine Growth Restriction: Cardiovascular Disorders. *Fetal Diagn Ther*, In press (2013).

18 AA Baschat. Fetal growth restriction - from observation to intervention. *J Perinat Med*, 38 (2010), 239-246.

19 AA, Baschat. Neurodevelopment following fetal growth restriction and its relationship with antepartum parameters of placental dysfunction. *Ultrasound Obstet Gynecol*, 37 (2011), 501-514.

20 Bijnens B, Cikes M, Butakoff C, Sitges M, Crispi F. Myocardial motion and deformation: What does it tell us and how does it relate to function? *Fetal Diagn Ther*, 32 (2012), 5-16.

21 Crispi F, Gratacós E. Fetal cardiac function: technical considerations and potential research and clinical applications. *Fetal Diagn Ther*, 32 (2012), 47-64.

22 Guyton AC, Hall JE. *Textbook of Medical Physiology ed 11*. Elsevier Saunder, Philadelphia, 2006.

23 Kiserud T, Acharya G. The fetal circulation. *Prenat Diagn*, 24 (2004), 1049-1059.

24 D Sedmera. Function and form in the developing cardiovascular system. *Cardiovasc Res*, 91 (2011), 252-259.

25 Opie LH, Commerford PJ, Gersh BJ, Pfeffer MA. Controversies in ventricular remodelling. *Lancet*, 367 (2006), 356-367.

26 Comas M, Crispi F, Cruz-Martinez R, Martinez JM, Figueras F, Gratacós E. Usefulness of myocardial tissue Doppler vs conventional echocardiography in the evaluation of cardiac dysfunction in early-onset intrauterine growth restriction. *Am J Obstet Gynecol*, 203 (2010), 45.e1-7.

27 Crispi F, Hernandez-Andrade E, Pelsers MM, Plasencia W, Benavides-Serralde JA, Eixarch E, Le Noble F, Ahmed A, Glatz JF, Nicolaides KH, Gratacos E. Cardiac dysfunction and cell damage across clinical stages of severity in growth-restricted fetuses. *Am J Obstet Gynecol*, 199 (2008), 254.e1-8.

28 Comas M, Crispi F, Cruz-Martinez R, Figueras F, Gratacos E. Tissue Doppler echocardiographic markers of cardiac dysfunction in small-for-gestational age fetuses. *Am J Obstet Gynecol*, 205 (2011), 57.es-6.

29 Cruz-Martinez R, Figueras F, Benavides-Serralde A, Crispi F, Hernandez-Andrade E, Gratacos E. Sequence of changes in myocardial performance index in relation to aortic isthmus and ductus venosus Doppler in fetuses with early-onset intrauterine growth restriction. *Ultrasound Obstet Gynecol*, 38 (2011), 179-184.

30 Verburg BO, Jaddoe VW, Wladimiroff JW, Hofman A, Witteman JC, Steegers EA. Fetal hemodynamic adaptive changes related to intrauterine growth: the Generation R Study. *Circulation*, 117 (2008), 649-659.

31 Soothill PW, Nicolaides KH, Campbell S. Prenatal asphyxia, hyperlacticaemia, hypoglycaemia, and erythroblastosis in growth retarded fetuses. *BMJ*, 294 (1987), 1051-1053.

32 Skilton MK, Evans N, Griffiths KA, Harmer JA, Celermajer D. Aortic wall thickness in newborns with intrauterine growth restriction. *Lancet*, 23 (2005), 1484-1486.

33 Turan S, Turan OM, Salim M, Berg C, Gembruch U, Harman CR, Baschat AA. Cardiovascular transition to extrauterine life in growth-restricted neonates: relationship with prenatal Doppler findings. *Fetal Diagn Ther*, 33 (2013), 103-109.

34 Kanaka-Gantenbein C. Fetal origins of adult diabetes. *Ann N Y Acad Sci* , 1205 (2010), 99-105.

35 Chaoui R. Coronary arteries in fetal life: physiology, malformations and the "heart-sparing effect". *Acta Paediatr Suppl*, 93 (2004), 6-12.

36 Crispi F, Bijnens B, Figueras F, Bartrons J, Eixarch E, Le Noble F, Ahmed A, Gratacós E. Fetal growth restriction results in remodeled and less efficient hearts in children. *Circulation*, 121 (2010), 2427-2436.

37 Hecher K, Snijders R, Campbell S, Nicolaides K. Fetal venous, intracardiac, and arterial blood flow measurements in intrauterine growth retardation: relationship with fetal blood gases. *Am J Obstet Gynecol* , 173 (1995), 10-15.

38 Ream M, Ray AM, Chandra R, Chikaraishi DM. Early fetal hypoxia leads to growth restriction and myocardial thinning. *Am J Physiol Regul Integr Comp Physiol*, 295 (2008), R583-595.

39 Rueda-Clausen CF, Morton JS, Davidge ST. Effects of hypoxia-induced intrauterine growth restriction on cardiopulmonary structure and function during adulthood. *Cardiovasc Res*, 81 (2009), 713-722.

40 Tong W, Xue Q, Li Y, Zhang L. Maternal hypoxia alters matrix metalloproteinase expression patterns and causes cardiac remodeling in fetal and neonatal rats. *Am J Physiol Heart Circ Physiol* , 301 (2011), H2113-2121.

41 Bae S, Xiao Y, Li G, Casiano CA, Zhang L. Effect of maternal chronic hypoxic exposure during gestation on apoptosis in fetal rat heart. *Am J Physiol Heart Circ Physiol* , 285 (200), H983-990.

42 Lim K, Zimanyi MA, Black MJ. Effect of maternal protein restriction during pregnancy and lactation on the number of cardiomyocytes in the postproliferative weanling rat heart. *Anat Rec (Hoboken)* , 293 (2010), 431-437.

43 Rueda-Clausen CF, Morton JS, Lopaschuk GD, Davidge ST. Long-term effects of intrauterine growth restriction on cardiac metabolism and susceptibility to ischaemia/reperfusion. *Cardiovasc Res*, 90 (2011), 285-294.

44 Xu Y, Williams SJ, O'Brien D, Davidge ST. Hypoxia or nutrient restriction during pregnancy in rats leads to progressive cardiac remodeling and impairs postischemic recovery in adult male offspring. *FASEB J* , 20 (2006), 1251-1253.

45 Thornburg KL, Reller MD. Coronary flow regulation in the fetal sheep. *Am J Physiol*, 277 (1999), R1249-1260.

46 Baschat AA, Gembruch U. Evaluation of the fetal coronary circulation. *Ultrasound Obstet Gynecol*, 20 (2002), 405-412.

47 Thompson LP. Effects of chronic hypoxia on fetal coronary responses. *High Alt Med Biol*, 4 (2003), 215-224.

48 Anderson RH, Ho SY, Redmann K, Sanchez-Quintana D, Lunkenheimer PP. The anatomical arrangement of the myocardial cells making up the ventricular mass. *Eur J Cardiothorac Surg*, 28 (2005), 517-525.

49 Anderson RH, Smerup M, Sanchez-Quintana D, Loukas M, Lunkenheimer PP. The three-dimensional arrangement of the myocytes in the ventricular walls. *Clin Anat*, 22 (2009), 64-76.

50 Sonnenblick EH, Ross J Jr, Covell JW, Spotnitz HM, Spiro D. The ultrastructure of the heart in systole and diastole. Changes in sarcomere length. *Circ Res*, 21 (1967), 423.431.

51 Henderson DJ, Anderson RH. The development and structure of the ventricles in the human heart.. *Pediatr Cardiol*, 588-596 (2009), 30.

52 Streeter DD Jr, Spotnitz HM, Patel DP, Ross J Jr, Sonnenblick EH. Fiber orientation in the canine left ventricle during diastole and systole. *Circ Res*, 24 (1969), 339-347.

53 Zhang L, Allen J, Hu L, Caruthers SD, Wickline SA, Chen J. Cardiomyocyte architectural plasticity in fetal, neonatal, and adult pig hearts delineated with diffusion tensor MRI.. *Am J Physiol Heart Circ Physiol*, 304 (2013), H246-H252.

54 Jouk PS, Usson Y, Michalowicz G, Grossi L. Three-dimensional cartography of the pattern of the myofibres in the second trimester fetal human heart. *Anat Embryol (Berl)*, 202 (2000), 103-118.

55 Jouk PS, Mourad A, Milisic V, Michalowicz G, Rault A, Caillerie D, Usson Y. Analysis of the fiber architecture of the heart by quantitative polarized light microscopy. Accuracy, limitations and contribution to the study of the fiber architecture of the ventricles during fetal and neonatal life. *Eur J Cardiothorac Surg*, 31 (2007), 915-921.

56 Tobita K, Garrison JB, Liu LJ, Tinney JP, Keller BB. Three-dimensional myofiber architecture of the embryonic left ventricle during normal development and altered mechanical loads. *Anat Rec A Discov*

Mol Cell Evol Biol, 283 (2005), 193-201.

57 Mekkaoui C, Huang S, Chen HH, Dai G, Reese TG, Kostis WJ, Thiagalingam A, Maurovich-Horvat P, Ruskin JN, Hoffmann U, Jackowski MP, Sosnovik DE. Fiber architecture in remdeled myocardium revealed with a quantitative diffusion CMR tractography framework and histological validation. *J Cardiovasc Magn Reson*, 14 (2012), 70.

58 Mekkaoui C, Porayette P, Jackowski MP, Kostis WJ, Dai G, Sanders S, Sosnovik DE. Diffusion MRI tractography of the developing human fetal heart. *PLoS One* , 8 (2013), e72795.

59 Betz O, Wegst U, Weide D, Heethoff M, Helfen L, Lee WK, Coletens P. Imaging applications of synchrotron X-ray phase-contrast microtomography in biological morphology and biomaterials science. I. General aspects of the technique and its advantages in the analysis of millimetre-sized arthropod structure. *J Microsc*, 227 (2007), 51-71.

60 Weitkamp T, David C, Bunk O, Bruder J, Cloetens P, Pfeiffer F. X-ray phase radiography and tomography of soft tissue using grating interferometry. *Eur J Radiol*, 68 (2008), S13-S17.

61 Kaasik A, Veksler V, Boehm E, Novotova M, Minajeva A, Ventura-Clapier R. Energetic crosstalk between organelles: architectural integration of energy production and utilization. *Circ Res*, 89 (2001), 153-159.

62 Nassar R, Reedy MC, Anderson PA. Developmental changes in the ultrastructure and sarcomere shortening of the isolated rabbit ventricular myocyte. *Circ Rres*, 61 (1987), 465-483.

63 Knaapen MW, Vrolijk BC, Wenink AC. Ultrastructural changes of the myocardium in the embryonic rat heart. *Anat Rec*, 248 (1997), 233-241.

64 Page E, Buecker JL. Development of dyadic junctional complexes between sarcoplasmic reticulum and plasmalemma in rabbit left ventricular myocardial cells. Morphometric analysis. *Circ Res*, 48 (1981), 519-522.

65 Piquereau J, Novotova M, Fortin D, Garnier A, Ventura-Clapier R, Veksler V, Joubert F. Postnatal development of mouse heart: formation of energetic microdomains. *J Physiol*, 588 (2010), 2443-2454.

66 Hoerter JA, Kuznetsov A, Ventura-Clapier R. Functional development of the creatine kinase system in perinatal rabbit heart. *Circ Res*, 69 (1991), 665-676.

67 Joubert F, Wilding JR, Fortin D, Domergue-Dupont V, Novotova M, Ventura-Clapier R, Veksler V. Local energetic regulation of sarcoplasmic and myosin ATPase is differently impaired in rats with heart failure. *J Physiol* , 586 (2008), 5181-5192.

68 Sabbah HN, Sharov V, Riddle JM, Kono T, Lesch M, Goldstein S. Mitochondrial abnormalities in myocardium of dogs with chronic heart failure. *J Mol Cell Cardiol*, 24 (1992), 1333-1347.

69 Ventura-Clapier R, Garnier A, Veksler V, Joubert F. Bioenergetics of the failing heart. *Biochim Biophys Acta* , 1813 (2011), 1360-1372.

70 Lopaschuk GD, Jaswal JS. Energy metabolic phenotype of the cardiomyocyte during development, differentiation, and postnatal maturation. *J Cardiovasc Pharmacol* , 56 (2010), 130-140.

71 Saks V, Kuznetsov AV, Gonzalez-Granillo M, Tepp K, Timohhina N, Karu-Varikmaa M, Kaambre T, Dos Santos P, Boucher F, Guzun R. Intracellular Energetic Units regulate metabolism in cardiac cells. *J Mol Cell Cardiol*, 52 (2012), 419-436.

72 Seppet EK, Eimre M, Anmann T, Seppet E, Peet N, Käämbre T, Paju K, Piirsoo A, Kuznetsov AV, Vendelin M, Gellerich FN, Zierz S, Saks VA. Intracellular energetic units in healthy and diseased hearts. *Exp Clin Cardiol* , 10 (2005), 173-183.

73 Seppet EK, Eimre M, Anmann T, Seppet E, Piirsoo A, Peet N, Paju K, Guzun R, Beraud N, Pelloux S, Tourneur Y, Kuznetsov AV, Käämbre T, Sikk P, Saks VA. Structure-function relationships in the regulation of energy transfer between mitochondria and ATPases in cardiac cells. *Exp Clin Cardiol*, 11 (2006), 189-194.

74 Stanley WC, Recchia FA, Lopaschuk GD. Myocardial substrate metabolism in the normal and failing heart. *Physiol Rev* , 85 (2005), 1093-1129.

75 Lemieux H, Semsroth S, Antretter H, Höfer D, Gnaiger E. Mitochondrial respiratory control and early defects of oxidative phosphorylation in the failing human heart. *Int J Biochem Cell Biol*, 43 (2011), 1729-1738.

76 Porter GA, Hom J, Hoffman D, Quintanilla R, de Mesy Bentley K, Sheu SS. Bioenergetics, mitochondria, and cardiac myocyte differentiation. *Prog Pediatr Cardiol* , 31 (2011), 75-81.

77 Al Ghouleh I, Khoo NK, Knaus UG, Griendling KK, Touyz RM, Thannickal VJ, Barchowsky A, Nauseef WM, Kelley EE, Bauer PM, Darley-Usmar V, Shiva S, Cifuentes-Pagano E, Freeman BA, Gladwin MT, Pagano PJ. Oxidases and peroxidases in cardiovascular and lung disease: new concepts in reactive oxygen species signaling. *Free Radic Biol Med*, 51 (2011), 1271-1288.

78 Scheubel RJ, Tostlebe M, Simm A, Rohrbach S, Prondzinsky R, Gellerich FN, Silber RE, Holtz J. Dysfunction of mitochondrial respiratory chain complex I in human failing myocardium is not due to disturbed mitochondrial gene expression. *J Am Coll Cardiol*, 40 (2002), 2174-2181.

79 Agarkova I, Perriard JC. The M-band: an elastic web that crosslinks thick filaments in the center of the sarcomere. *Trends Cell Biol*, 15 (2005), 477-485.

80 Bönnemann CG, Laing NG. Myopathies resulting from mutations in sarcomeric proteins. *Curr Opin Neurol*, 17 (2004), 529-537.

81 Cheng Y, Wan X, McElfresh TA, Chen X, Gresham KS, Rosenbaum DS, Chandler MP, Stelzer JE. Impaired contractile function due to decreased cardiac myosin binding protein C content in the sarcomere. *Am J Physiol Heart Circ Physiol*, 305 (2013), H52-65.

82 Patel JR, Pleitner JM, Moss RL, Greaser ML. Magnitude of length-dependent changes in contractile

properties varies with titin isoform in rat ventricles. *Am J Physiol Heart Circ Physiol*, 302 (2012), H697-708.

83 Fukuda N, Sasaki D, Ishiwata S, Kurihara S. Length dependence of tension generation in rat skinned cardiac muscle: role of titin in the Frank-Starling mechanism of the heart. *Circulation*, 104 (2001), 1639-1645.

84 Boulesteix T, Beaurepaire E, Sauviat MP, Schanne-Klein MC. Second-harmonic microscopy of unstained living cardiac myocytes: measurements of sarcomere length with 20-nm accuracy. *Opt Lett*, 29 (2004), 2031-2033.

85 Bub G, Camelliti P, Bollensdorff C, Stuckey DJ, Picton G, Burton RA, Clarke K, Kohl P. Measurement and analysis of sarcomere length in rat cardiomyocytes in situ and in vitro. *Am J Physiol Heart Circ Physiol*, 298 (2010), H1616-25.

86 Anderson PG, Bishop SP, Digerness SB. Transmural progression of morphologic changes during ischemic contracture and reperfusion in the normal and hypertrophied rat heart. *Am J Phatol*, 129, 152-167.

87 Radke MH, Peng J, Wu Y, McNabb M, Nelson OL, et al. Targeted deletion of titin N2B region leads to diastolic dysfunction and cardiac atrophy. *Proc Natl Acad Sci U S A* , 104 (2007), 3444-3449.

88 Chen JF, Murchison EP, Tang R, Callis TE, Tatsuguchi M, et al. Targeted deletion of Dicer in the heart leads to dilated cardiomyopathy and heart failure. *Proc Natl Acad Sci U S A*, 105 (2008), 2111-2116.

89 Haddad F, Bodell PW, Baldwin KM. Pressure-induced regulation of myosin expression in rodent heart. *J Appl Physiol*, 4 (1995), 1489-1495.

90 Warren CM, Jordan MC, Roos KP, Krzesinski PR, Greaser ML. Titin isoform expression in normal and hypertensive myocardium. *Cardiovasc Res* , 59 (2003), 86-94.

91 Falcão-Pires I, Palladini G, Gonçalves N, van der Velden J, Moreira-Gonçalves D, et al. Distinct mechanisms for diastolic dysfunction in diabetes mellitus and chronic pressure-overload. *Basic Res Cardiol* , 106 (2011), 801-814.

92 Campagnola PJ, Millard AC, Terasaki M, Hoppe PE, Malone CJ, Mohler WA. Three-Dimensional High-Resolution Second-Harmonic Generation Imaging of Endogenous Structural Proteins in Biological Tissues. *Biophys J*, 82 (2002), 493-508.

93 Plotnikov S, Juneja V, Isaacson A, Mohler W, Campagnola P. Optical Clearing for Improved Contrast in Second Harmonic Generation Imaging of Skeletal Muscle. *Biophys J*, 90 (2006), 328-339.

94 Plotnikov SV, Kenny AM, Walsh SJ, Zubrowski B, Joseph C, Scranton VL, Kuchel GA, Dauser D, Xu M, Pilbeam CC, Adams DJ, Dougherty RP, Campagnola PJ, Mohler WA. Measurement of muscle disease by quantitative second-harmonic generation imaging. *J Biomed Opt*, 13 (2008), 044018.

95 Plotnikov SV, Millard A, Campagnola PJ, Mohler WA. Characterization of the Myosin-Based Source for

Second-Harmonic Generation from Muscle Sarcomeres. *Biophys J* , 90 (2006), 693-703.

96 Rao RA, Mehta MR, Toussaint KC Jr. Fourier transform-second-harmonic generation imaging of biological tissues. *Opt Express*, 17 (2009), 14534-14542.

97 Sivaguru M, Durgam S, Ambekar R, Luedtke D, Fried G, Stewart A, Toussaint KC Jr. Quantitative analysis of collagen fiber organization in injured tendons using Fourier transform-second harmonic generation imaging. *Opt Express*, 18 (2010), 24983-24993.

98 Garcia-Canadilla P, Gonzalez-Tendero A, Iruretagoyena I, Crispi F, Torre I, Amat-Roldan I, Bijnens B, Gratacós E. Automated cardiac sarcomere analysis for Second Harmonic Generation images. *J Biomed Opt*, In press (2014).

99 Figueras F, Meler E, Iraola A, Eixarch E, Coll O, Figueras J, Francis A, Gratacos E, Gardosi J. Customized birthweight standards for a Spanish population. *Eur J Obstet Gynecol Reprod Biol*, 136 (2008), 20-24.

100 Baschat AA, Gembruch U. The cerebroplacental Doppler ratio revisited. *Ultrasound Obstet Gynecol*, 21 (2003), 124-127.

101 Eixarch E, Figueras F, Hernández-Andrade E, Crispi F, Nadal A, Torre I, Oliveira S, Gratacós E. An experimental model of fetal growth restriction based on selective ligature of uteroplacental vessels in the pregnant rabbit. *Fetal Diagn Ther* , 26 (2009), 203-211.

102 Eixarch E, Hernandez-Andrade E, Crispi F, Illa M, Torre I, Figueras F, Gratacos E. Impact on fetal mortality and cardiovascular Doppler of selective ligature of uteroplacental vessels compared with undernutrition in a rabbit model of intrauterine growth restriction. *Placenta*, 32 (2011), 304-309.

103 Paganin D, Gureyev TE, Mayo SC, Stevenson AW, Nesterets YI, Wilkins SW. X-ray omni microscopy. *J Microsc*, 214 (2004), 315-327.

104 Schindelin J, Arganda-Carreras I, Frise E, Kaynig V, Longair M, Pietzsch T, Preibisch S, Rueden C, Saalfeld S, Schmid B, Tinevez JY, White DJ, Hartenstein V, Eliceiri K, Tomancak P, Cardona A. Fiji: an open-source platform for biological-image analysis. *Nat Methods*, 9 (2012), 676-682.

105 de Chaumont F, Dallongeville S, Chenouard N, Hervé N, Pop S, Provoost T, Meas-Yedid V, Pankajakshan P, Lecomte T, Le Montagner Y, Lagache T, Dufour A, Olivo-Marin JC. Icy: an open bioimage informatics platform for extended reproducible research. *Nat Methods*, 9 (2012), 690-696.

106 Sommer C, Straehle C, Köthe U, Hamprecht FA. *8th IEEE International Symposium on Biomedical Imaging (ISBI 2011), in press*.

107 WS, Rasband. *ImageJ, U. S. National Institutes of Health*. http://imagej.nih.gov/ij/, Bethesda, Maryland, USA, 1997-2011.

108 Gundersen HJ, Bendtsen TF, Korbo L, Marcussen N, Møller A, Nielsen K, Nyengaard JR, Pakkenberg B, Sørensen FB, Vesterby A, et al. Some new, simple and efficient stereological methods and their use in

pathological research and diagnosis. *APMIS* , 96 (1988), 379-394.

109 Hiraumi Y, Iwai-Kanai E, Baba S, Yui Y, Kamitsuji Y, Mizushima Y, Matsubara H, Watanabe M, Watanabe K, Toyokuni S, Matsubara H, Nakahata T, Adachi S. Granulocyte colony-stimulating factor protects cardiac mitochondria in the early phase of cardiac injury. *Am J Physiol Heart Circ Physiol*, 29 (2009), H823-832.

110 Breu H, Gil J, David Kirkpatrick D, Werman M. Linear Time Euclidean Distance Transform Algorithms. *IEEE Trans Pattern Anal Mach Intell*, 5 (1995), 529-533.

111 Garcia-Canadilla P, Torre I, Gonzalez-Tendero A, et al. Automated morphometric characterization of cardiac fibers by second harmonic microscopy imaging. *Proc IEEE Int Symp Biomed Imaging* (2011), 1379-1982.

112 Conturo TE, Lori NF, Cull TS, Akbudak E, Snyder AZ, Shimony JS, McKinstry RC, Burton H, Raichle ME. Tracking neuronal fiber pathways in the living human brain. *Proc Natl Acad Sci U S A.*, 96 (1999), 10422-10427.

113 Chaturvedi RR, Herron T, Simmons R, Shore D, Kumar P, Sethia B, Chua F, Vassiliadis E, Kentish JC. Passive stiffness of myocardium from congenital heart disease and implications for diastole. *Circulation*, 121 (2010), 979-988.

114 Wallace SJ, Morrison JL, Botting KJ, Kee TW. Second-harmonic generation and two-photon-excited autofluorescence microscopy of cardiomyocytes: quantification of cell volume and myosin filaments. *J Biomed Opt*, 13 (2008), 064018.

115 Hecher K, Campbell S, Snijders R, Nicolaides K. Reference ranges for fetal venous and atrioventricular blood flow parameters. *Ultrasound Obstet Gynecol* , 4 (1994), 390-391.

116 Cruz-Martínez R, Figueras F, Bennasar M, García-Posadas R, Crispi F, Hernández-Andrade E, Gratacós E. Normal reference ranges from 11 to 41 weeks' gestation of fetal left modified myocardial performance index by conventional Doppler with the use of stringent criteria for delimitation of the time periods. *Fetal Diagn Ther*, 32 (2012), 79-86.

117 DeVore GR. Assessing fetal cardiac ventricular function. *Semin Fetal Neonatal Med*, 10 (2005), 515-541.

118 Tsutsumi T, Ishii M, Eto G, Hota M, Kato H. Serial evaluation for myocardial performance index in fetuses and neonates using a new Doppler index. *Pediatr Int*, 41 (1999), 722-727.

119 Tei C, Ling LH, Hodge DO, Bailey KR, Oh JK, Rodeheffer RJ, Tajik AJ, Seward JB. New index of combined systolic and diastolic myocardial performance: a simple and reproducible measure of cardiac function--a study in normals and dilated cardiomyopathy. *J Cardiol*, 26 (1995), 357-366.

120 Belenky A, Smith A, Zhang B, Lin S, Despres N, Wu AH, Bluestein BI. The effect of class-specific protease inhibitors on the stabilization of B-type natriuretic peptide in human plasma. *Clin Chim Acta*, 340 (2004), 163-172.

121 Smyth GK. Linear models and empirical bayes methods for assessing differential expression in microarray experiments. *Stat Appl Genet Mol Biol*, 3 (2004), Article 3.

122 Benjamini Y, Hochberg Y. Controlling the false discovery rate a practical and powerful approach to multiple testing. *J R Statist Soc B*, 57 (1995), 289-300.

123 Medina I, Carbonell J, Pulido L, Madeira SC, Goetz S, Conesa A, Tárraga J, Pascual-Montano A, Nogales-Cadenas R, Santoyo J, García F, Marbà M, Montaner D, Dopazo J. Babelomics: an integrative platform for the analysis of transcriptomics, proteomics and genomic data with advanced functional profiling. *Nucleic Acids Res*, 38 (2010), W210-W213.

124 Beaudoin S, Barbet P, Bargy F. Developmental stages in the rabbit embryo: guidelines to choose an appropriate experimental model. *Fetal Diagn Ther*, 18 (2003), 422-427.

125 Bassan H, Trejo LL, Kariv N, Bassan M, Berger E, Fattal A, Gozes I, Harel S. Experimental intrauterine growth retardation alters renal development. *Pediatr Nephrol* , 15 (2000), 192-195.

126 Wang KC, Zhang L, McMillen IC, Botting KJ, Duffield JA, Zhang S, Suter CM, Brooks DA, Morrison JL. Fetal growth restriction and the programming of heart growth and cardiac insulin-like growth factor 2 expression in the lamb. *J Physiol*, 589 (2011), 4709-4722.

127 Schwarzer M, Schrepper A, Amorim PA, Doenst T. Pressure overload differentially affects respiratory capacity in interfibrillar and subsarcolemmal mitochondria. *Am J Physiol Heart Circ Physiol*, 304 (2013), H529-H537.

128 Lewis AM, Mathieu-Costello O, McMillan PJ, Gilbert RD. Quantitative electron microscopic study of the hypoxic fetal sheep heart. *Anat Rec*, 256 (1999), 381-388.

129 Friehs I, Cowan DB, Choi YH, Black KM, Barnett R, Bhasin MK, Daly C, Dillon SJ, Libermann TA, McGowan FX, del Nido PJ, Levitsky S, McCully JD. Pressure-overload hypertrophy of the developing heart reveals activation of divergent gene and protein pathways in the left and right ventricular myocardium. *Am J Physiol Heart Circ Physiol*, 304 (2013), H697-708.

130 Selak MA, Storey BT, Peterside I, Simmons RA. Impaired oxidative phosphorylation in skeletal muscle of intrauterine growth-retarded rats. *Am J Physiol Endocrinol Metab*, 285 (2003), E130-137.

131 Del Duca D, Tadevosyan A, Karbassi F, Akhavein F, Vaniotis G, Rodaros D, Villeneuve LR, Allen BG, Nattel S, Rohlicek CV, Hébert TE. Hypoxia in early life is associated with lasting changes in left ventricular structure and function at maturity in the rat. *Int J Cardiol*, 156 (2012), 165-173.

132 Gibson K, Halliday JL, Kirby DM, Yaplito-Lee J, Thorburn DR, Boneh A. Mitochondrial oxidative phosphorylation disorders presenting in neonates: clinical manifestations and enzymatic and molecular diagnoses. *Pediatrics*, 122 (2008), 1003-1008.

133 Hecher K, Campbell S, Doyle P, Harrington K, Nicolaides K. Assessment of fetal compromise by Doppler ultrasound investigation of the fetal circulation: arterial, intracardiac, and venous blood flow velocity

studies. *Circulation*, 91 (1995), 129-138.

134 Makikallio K, Vuolteenaho O, Jouppila P, Rasanen J. Ultrasonographic and biochemical markers of human fetal cardiac dysfunction in placental insufficiency. *Circulation*, 105 (2002), 2058-2063.

135 Girsen A, Ala-Kopsala M, Makikallio K, Vuolteenaho O, Rasanen J. Cardiovascular hemodynamics and umbilical artery N-terminal peptide of proB-type natriuretic peptide in human fetuses with growth restriction. *Ultrasound Obstet Gynecol* , 29 (2007), 296-303.

136 Wannenburg T, Heijne GH, Geerdink JH, Van Den Dool HW, Janssen PM, de Tombe PP. Cross-bridge kinetics in rat myocardium: effect of sarcomere length and calcium activation. *Am J Physiol Heart Circ Physiol*, 279 (2000), H779-H790.

137 Gordon AM, Homsher E, Regnier M. Regulation of contraction in striated muscle. *Physiol Rev*, 80 (2000), 853-924.

138 Sela G, Yadid M, Landesberg A. Theory of cardiac sarcomere contraction and the adaptive control of cardiac function to changes in demands. *Ann N Y Acad Sci*, 1188 (2010), 222-230.

139 Agarkova I, Ehler E, Lange S, Schoenauer R, Perriard JC. M-band: a safeguard for sarcomere stability?. *J Muscle Res Cell Motil*, 24 (2003), 191-203.

140 Tskhovrebova L, Trinick J. Titin: properties and family relationships. *Nat Rev Mol Cell Biol* (2003), 679-689.

141 Labeit S, Kolmerer B, Linke WA. The giant protein titin. Emerging roles in physiology and pathophysiology. *Circ Res*, 80 (1997), 290-294.

142 Rodriguez AG, Han SJ, Regnier M, Sniadecki NJ. Substrate stiffness increases twitch power of neonatal cardiomyocytes in correlation with changes in myofibril structure and intracellular calcium. *Biophys J*, 101 (2011), 2455-2464.

143 Schoenauer R, Emmert MY, Felley A, Ehler E, Brokopp C, Weber B, Nemir M, Faggian GG, Pedrazzini T, Falk V, Hoerstrup SP, Agarkova I. EH-myomesin splice isoform is a novel marker for dilated cardiomyopathy. *Basic Res Cardiol*, 106 (2011), 233-247.

144 Kruger M, Linke WA. Titin-based mechanical signalling in normal and failing myocardium. *J Mol Cell Cardiol*, 46 (2009), 490-498.

145 Barefield D, Sadayappan S. Phosphorylation and function of cardiac myosin protein-C in health and disease. *J Mol Cell Cardiol*, 48 (2010), 866-875.

146 Fouron JC, Skoll A, Sonesson SE, Pfizenmaier M, Jaeggi E, Lessard M. Relationship between flow through the fetal aortic isthmus and cerebral oxygenation during acute placental circulatory insufficiency in ovine fetuses. *Am J Obstet Gynecol*, 181 (1999), 1102-1107.

10. ACKNOWLEDGMENTS

10. ACKNOWLEDGMENTS

Financial support

Anna Gonzalez-Tendero was supported by a predoctoral fellowship from the Institut d'Investigacions Biomèdiques August Pi i Sunyer (IDIBAPS).

Studies were supported by grants from Ministerio de Economia y Competitividad PN de I+D+I 2008-2011 (ref. SAF2009_08815, SAF2012-37196 and BIO2011-27069); Instituto de Salud Carlos III (ref. PI11/00051, PI11/01709, PI12/00801) cofinanciado por el Fondo Europeo de Desarrollo Regional de la Unión Europea "Una manera de hacer Europa"; Centro para el Desarrollo Técnico Industrial (Ref. cvREMOD 2009-2012) apoyado por el Ministerio de Economia y Competitividad y Fondo de inversión local para el empleo, Spain; The Cerebra Foundation for the Brain Injured Child (Carmarthen, Wales, UK); Obra Social "La Caixa" (Spain); Fundació Mutua Madrileña (Spain); Fundació Agrupació Mutua (Spain); AGAUR 2009 SGR grant nº 1099 and Red Temática de Investigación Cooperativa en cancer (ref. RD06/0020/1019). We acknowledge the *European Synchrotron Radiation Facility* for provision of synchrotron facilities.

I would like to express my gratitude to all the people who have made the completion of this Thesis possible, to those who have helped me from the beginnig to the end and to those who have had a significant relevance at any point during this period.

To my directors, Eduard Gratacós, Bart Bijnens and Fàtima Crispi. It is because of the opportunity they granted me by their acceptance in this wonderful group, and to take on this ambitious project, that I am here today.

To Eduard, for being the best example of a persistent, talented, exigent and excellent researcher. To Bart for making the completion of this Thesis possible when it was needed, for being challenging which has made me become demanding with myself, always willing to improve. To Fàtima for taking the responsibility of this Thesis, for always encouraging me to continue with this research and for being the best example to follow, I am very grateful to her for everything she taught me during this project and for trusting me.

To all coauthors of the papers whose work has been essential in order to achieve this Thesis and from whom I could learnt.

Aquesta Tesis ha estat un camí llarg en el que han intervingut moltes persones. Tot i que totes les paraules d'agraïment seràn poques, m'agradaria fer una menció especial a aquelles persones que crec que han tingut un paper rellevant i han aconseguit aportar-me moltíssim; així com a aquelles que han tingut la paciència d'ensenyar-me.

A la Míriam i l'Eli, per endinsar-me en el món dels models animals, per ensenyar-me amb la màxima exigència i contagiar-me del seu entusiasme i optimisme que tant les caracteritza i que tant m'agrada.

A totes les persones dels CCiTUB amb qui he pogut aprendre tant i qui transmetent-me la seva professionalitat i passió per la ciència, així com la seva confiança, han donat un color especial a

aquest projecte. A la Maria Calvo, la Carmen, Gemma, Yolanda i Nieves, per contagiar-me la seva passió per la microscopia. A la Isabel i la gent que l'envolta, per la seva ajuda, confiança i per saber crear aquest ambient tan acollidor.

A en Leif Hove-Madsen del ICCC-CSIC de Sant Pau, per la seva professionalitat i per tot el que m'ha ensenyat d'electrofisiologia cel.lular.

A totes les persones del grup de medicina fetal i perinatal, qui al llarg dels anys i condicions cambiants, han esdevingut amics i família. Sense tots ells aquest projecte no hagués estat possible. Crec que les persones som el que som perquè estem formats per petites aportacions de totes les persones que van passant per la nostra vida; amb tots vosaltres he crescut, m'he format i tant aquesta tesis com jo mateixa portem un trosset de cadascún de vosaltres.

A la Patricia, per ser la millor coautora, amb qui he pogut aprendre el punt de vista "telecos" i treballar de la millor manera possible. Li agraeixo haver pogut compartir amb ella els moments difícils, professionals i personals; entendre'm, coneixe'm i sempre estar disposada a ajudar. Al Dafnis i l' Emma, perquè potser sense saber-ho m'han ajudat a somriure en moments complicats. A totes les persones de gestió, en especial a la Maite, que m'ha vist créixer i a la Balma, per aguantar la meva insistència i demanar-li sempre les coses "urgents" i comandes extranyes.

I amb molta nostàlgia recordo i m'agradaria agraïr a algunes de les persones que han passat per aquest grup, amb qui vem compartir estones extraordinàries. A l'Ariadna, per el toc que donava a aquest grup amb la seva alegria i espontaneïtat. A la Marina, amb qui hem compartit amistat i professió; per escoltar-me, motivar-me, fer-me riure…infinitat de coses bones que m'has aportat.

A les dues persones que han donat color i alegria a aquesta Tesis; Marina i Montse. Totes les paraules del món es queden curtes per agraïr-vos el vostre suport.

A la Clara i el Sergi, pel seu suport i el seu interés en la meva feina.

A la Cristina, per dedicar el seu temps en dissenyar aquesta magnífica portada.

Als meus pares, per el seu constant suport incondicional i aguantar-me els meus moments de nervis. Per ser el clar exemple a seguir, per la seva capacitat de treure forces d'on creies que no n'hi havia i ensenyar-me que malgrat la boira cal caminar. Als meus germans i en Sergio, per posar sempre el seu toc d'humor i per el seu interès en la meva feina. Per què en moments complicats t'adones de la importància de la família i que són les persones que et donaràn suport de forma incondicional.

A tu, que has estat present en moments claus, per el teu suport, per escoltar-me i estimar-me.